A Comprehensive Study of Proto-Planetary Disks around Herbig Ae stars using Long-Baseline Infrared Interferometry

by

Ajay-Kumar M. Tannirkulam

A dissertation submitted in partial fulfillment
of the requirements for the degree of
Doctor of Philosophy
(Astronomy and Astrophysics)
in The University of Michigan
2008

Doctoral Committee:

Associate Professor John D. Monnier, Chair
Professor Fred C. Adams
Professor Sushil K. Atreya
Professor Nuria P. Calvet
Associate Professor Edwin A. Bergin

"Where the mind is without fear and the head is held high

Where knowledge is free

Where the world has not been broken up into fragments by narrow domestic walls

Where words come out from the depth of truth

Where tireless striving stretches its arms towards perfection

Where the clear stream of reason has not lost its way into the dreary desert sand of dead habit

Where the mind is led forward by thee into ever-widening thought and action

Into that heaven of freedom, my Father, let my country awake."

Rabindranath Tagore (1861-1941)

To Amma, Appa and my sister, Bhargavi.

Acknowledgments

The fruition of this thesis has depended on the support and assistance of many people. First, and foremost, a big "thank you" to my thesis advisor Prof. John Monnier for being a great mentor. It has been a privilege and a pleasure being his graduate student. He has always motivated me to perform to the best of my abilities and his enthusiasm and work ethics have been very inspirational. I am very grateful to him for providing me the guidance and the resources to work on very interesting astrophysical problems. I have been fortunate to have had valuable discussions with Dr. Tim Harries (University of Exeter) on young-stellar-object science. The majority of the disk-structure calculations in my thesis were performed with the TORUS Monte-Carlo radiation-transfer code developed by Dr. Harries's group. He has always been readily available for consultation and technical advice. I owe much of my interferometric observing skills to Dr. Rafael Millan-Gabet (Michelson Science Center) and am thankful for his friendly advice and encouragement. I very much appreciate the time and effort of my thesis committee: Prof. Fred Adams, Prof. Sushil Atreya, Prof. Nuria Calvet and Prof. Edwin Bergin. Their advice and constructive criticism has been very helpful. I am lucky to have been able to interact frequently with Prof. Calvet and Prof. Bergin and am thankful for their valuable suggestions and support. Prof. Timothy Mckay, my Master's project advisor in-

troduced me to hands-on astronomy research and made me realize the importance of time management. The entire Astronomy faculty at University of Michigan has been very friendly and supportive and I am grateful to them for making my graduate education very enjoyable.

Next, I would like to acknowledge the assistance of Jeremy Hallum, Dr. Michael Busha, Marlin Whitaker, Dr. Phillip Hughes, Dr. Augustus Evrard, Rebecca Stanek and Roy Bonser for helping me execute code on the Wiglaf and Opus Beowulf clusters. I am especially thankful to Dr. Hughes for clarifying many of my elementary questions on parallel code compilation. I want to thank Tom Brink, Ming Zhao, Zhaohuan Zhu, John Tobin, Dr. Jesus Hernandez, Dr. David Berger, Dr. Ettore Pedretti (University of St. Andrews), Dr. Rishi Sharma (Los Alamos National Labs), Dr. Theo ten Brummelaar (CHARA, GSU), Prof. Lynne Hillenbrand (California Institute of Technology), Prof. Michael Meyer (University of Arizona), Prof. Charles Cowley and Prof. Lee Hartmann for technical discussions that have helped me crystallize my thoughts at various occasions. The staff at MDM Observatories and CHARA (Georgia State University) helped make my observing runs successful and very enjoyable. Carin Scott, Stephanie Ford and Sarah Lloyd have helped me a great deal with administrative chores and have been extremely patient with me on the numerous occasions where I did not turn in papers on time.

The graduate students and the research scholars at the Astronomy Department have made 6 years of my stay in Ann Arbor a lot of fun. The congenial atmosphere and the cooperative spirit that they provide makes the Department a great place to be in. Tom Brink has been a very good office mate and friend. We have had

deep, insightful discussions on a wide variety of topics ranging from cricket, arranged marriages in India, the scientific validity of agnosticism, the superiority of Waltz vs Salsa and veganism. These discussions have sometimes been big suckers of time which often drew in unsuspecting prey in the form of Ming Zhao, Jess Werk, Sarah Ragan, Rebecca Stanek and Laura Ingleby. I wish to thank Shannon Schmoll for her excellent ginger cake which made me realize that vegan desserts need not always have to be bad. Tom Brink, Sarah Ragan, Rebecca Stanek, Jess Werk and Jefferey Fogel have been excellent organizers for a number of social events which often helped me kick off my weekends on a fun note. Thanks to all my friends at Michigan. Fortunately, I have too many to list everyone, but I am especially thankful to my apartment mates, Ajay Raghavan, Shidhartha Das, Siddharth D'Silva, Harsh Singhal, Vishal Shah and Panos for tolerating my bathroom singing and making my stay enjoyable. Lastly, but definitely not the least, the encouragement of parents, sister Bhargavi and my extended family played an important role in the realization of my dissertation.

This thesis was supported in part by NASA Grant 050283. The support is greatly appreciated. Chapters 2, 3, 4 and 5 in the thesis are partly based on publications in the Astrophysical Journal (Tannirkulam et al. [2007, 2008b]) and the Astrophysical Journal Letters (Monnier et al. [2008a]; Tannirkulam et al. [2008]).

Contents

List of Figures

Figure

List of Tables

Table

List of Appendices

Appendix

List of Abbreviations

BCL	Beam Combination Laboratory
BSF	Beam Synthesis Facility
CHARA	Center for High Angular Resolution Astronomy
CSM	circumstellar material
IR	infrared
HAe	Herbig Ae
HAe/Be	Herbig Ae/Be
IOTA	Infrared Optical Telescope Array
GSU	Georgia State University
MIR	mid infrared
NIR	near infrared
OPLE	Optical Path Length Equalization
POP	Pipes of Pan
PTI	Palomar Testbed Interferometer
SED	Spectral Energy Distribution
UD	Uniform Disk
VLTI	Very Large Telescope Interferometer
YSO	Young Stellar Object

Abstract

A Comprehensive Study of Proto-Planetary Disks around Herbig Ae stars using Long-Baseline Infrared Interferometry

by

Ajay-Kumar M. Tannirkulam

Chair: John D. Monnier

Planetary systems are born in circumstellar disks around young stellar objects (YSOs) and the disk is thought to play a major role in the evolution of planetary systems. A good understanding of disk structure and its time evolution is therefore essential in comprehending planet formation, planet migration and the diversity of planetary systems. In this thesis, I use high angular resolution observations and state-of-the-art radiative transfer modeling to probe circumstellar disk structure and validate current disk models.

First, I discuss models and observations of the gas-dust transition region in YSOs. The dust component in circumstellar disks gets truncated at a finite radius from the central star, inside of which it is too hot for dust to survive. The truncated disk forms an "evaporation front" whose shape depends sensitively on dust properties. The possibility of using the front as a probe of the dust physics operating in circumstellar disks is explored. The Center for High Angular Resolution Astronomy (CHARA)

near-infrared (near-IR) array is used to resolve out the evaporation front in the Herbig Ae stars MWC275 and AB Aur, and the presence of an additional near-IR opacity source within the "conventional" dust destruction radius is reported. Second, I describe comprehensive disk models that simultaneously explain the spectral energy distribution (from UV to milli-meter) and long-baseline interferometry (from near-IR to mm) of Herbig Ae stars. The models are constrained with a wide range of data drawn from the literature as well as new interferometric observations in the K-band with the CHARA array and in the mid-IR with the novel Keck Segment Tilting Experiment. I show that the mid-IR size of MWC275 relative to AB Aur is small, suggesting that dust grains in the outer disk of MWC275 are significantly more evolved/settled than the grains in the AB Aur disk. Using the Segment Tilting data, I also demonstrate that Herbig Ae/Be systems having a higher mid-IR surface brightness tend to have bluer mid-IR colors. I interpret this trend with simple geometric models for circumstellar disks.

I conclude with a discussion on exciting prospects for measuring the gas-disk morphology on scales of fractions of an AU with the CHARA array, introducing a new powerful tool to understand the "star-disk connection".

Chapter 1

Introduction

In this thesis, I focus on the structure of disks surrounding intermediate mass ($1.5_{\odot}$ - 4 $M_{\odot}$) young stellar objects (YSOs). These disks are formed as a natural consequence of angular momentum conservation during the star formation process. Circumstellar-disk material composed of dust and gas provides the physical setting in which planetary systems are born and evolve. Circumstellar disks have therefore become core subjects of study in modern astronomy.

One class of intermediate mass YSOs, the Herbig Ae/Be stars, are key to detailed understanding of proto-planetary disk strucure. Due to the higher luminosity and effective temperature of the central star, the region of the disk emitting at a given wavelength is much larger in Herbig Ae/Be (HAe/Be) stars than in solar type T Tauri stars. Therefore, when at similar distances from the earth, HAe/Be stars are more amenable to spatially resolved studies. Fortunately, quite a few HAe/Be stars exist within 150pc from us making them ideal test subjects for YSO disk studies accessing current high resolution instrumentation. The star and disk properties from T Tauri to HAe stars, form a continuum (see for e.g. Mottram et al. [2007]) and the results that I obtain on HAe stars will act as a bridge towards theories of T Tauri disks and lay a strong foundation for future studies of T Tauri systems with the next generation

of higher sensitivity, higher spatial resolution instruments.

1.1 Star Formation

Stars are formed from the collapse (gravitational/external compression) of molecular clouds. Molecular cloud material (mostly hydrogen and helium) having typical number densities of 10^5-10^6 cm^{-3}, gets compressed by over 17 orders of magnitude en-route to forming stars. The size scale of the cloud also decreases several orders of magnitude (from parsecs to hundreds of AU). Thus any rotation present in the cloud initially gets enormously magnified due to angular momentum conservation. The bulk of the in-falling material falls onto a disk from which material is then accreted onto the central growing stellar embryo. Fig 1.1 shows a schematic for the star formation process for low ($0.1M_\odot$ - $1.5M_\odot$) and intermediate mass stars ($1.5M_\odot$ - $8M_\odot$).

Based on the work of Adams et al. [1987] and Lada [1987], the process can be divided into 4 stages -

- **Class 0:** In the class 0 stage, the proto-stellar core is completely embedded in the in-falling envelope (Andre et al. [2000]). The potential energy of the system gets converted into thermal energy and the spectral energy distribution (SED) peaks in the mid and far infrared wavelengths. Fig 1.2 is a Hubble image of the Eagle Nebula which harbors many protostars in the Class 0 phase.
- **Class I:** In the Class I stage, the disk becomes prominent and the protostar is optically detectable for the first time. The star is heavily obscured by surrounding dust. The bulk of the energy is released through the stellar luminosity

and from viscous dissipation in the active accretion disk.

- **Class II:** Mass accretion rates drop down significantly and the disk becomes relatively quiescent. The central star is optically visible and the infrared excess is dominated by the reprocessing of stellar light by circumstellar material. Planetary systems are born and actively evolve in this stage. Figs 1.4 and 1.5 show scattered light images of famous Class II sources AB Aur and MWC275. These objects are the central subjects of this thesis.
- **Class III:** In the Class III stage, much of the circumstellar material has been accreted/dissipated. Class III objects sometimes exhibit a weak mid-IR excess due to the presence of an optically thin remnant disk (debris disk). AU Microscopii (see Fig 1.6) is a famous Class III debris disk object.

  In the next section, we describe observational properties of intermediate mass YSOs, objects of detailed study in later chapters.

1.2 Herbig Ae/Be stars

Herbig Ae/Be (HAe/Be) stars are pre-main-sequence stars in the mass range of $1.5M_{\odot}$ - $8M_{\odot}$. They were first classified by Herbig [1960] in an attempt to observationally identify more massive analogues of T Tauri stars. We follow Waters & Waelkens [1998] in listing a working definition of HAe/Be stars: *Herbig Ae/Be stars have spectral types F6 to B, luminosity class III to V and display emission lines. Their SED shows an infrared excess over stellar photospheric values due to the presence of hot/cool circumstellar dust.* Some of the general properties of HAe/Be stars as reviewed in Waters & Waelkens [1998] are -

- **SED** The infrared SED is characterized by the emission due to large amounts of circumstellar material (CSM). For HAe/Be stars in the Class II phase, the bulk of IR emission arises from warm dust heated by stellar photons. Some HAeBe stars also exhibit excess UV continuum emission from accretion of gas. In subsequent chapters, we will use SED and interferometry as powerful probes of CSM geometry.
- **Photometric Variability** The optical continuum of HAe/Be stars show variability on several time scales. Some of the more extreme variable sources (≥ 1 mag in the visual band) are termed UX Orionis objects. These variations are believed to arise from the changing geometry of the CSM.
- **Line Spectra** Frequently observed emission lines in HAe/Be stars are from hydrogen, oxygen, silicon, calcium, sulphur and magnesium. The lines show time variability and complex line profiles. The photospheric absorption features are fairly straightforward and the line strengths are consistent with F, A and B main sequence stars.
- **Polarization** The optical continuum of HAe/Be stars shows intrinsic and variable polarization due to the presence of aligned dust grains or grains in a non-spherical geometry. The polarization in some sources is high (several percent) and can also exhibit strong variability coinciding with photometric minima. These observations have been interpreted in terms of dust blocking the unpolarized light from the central source.

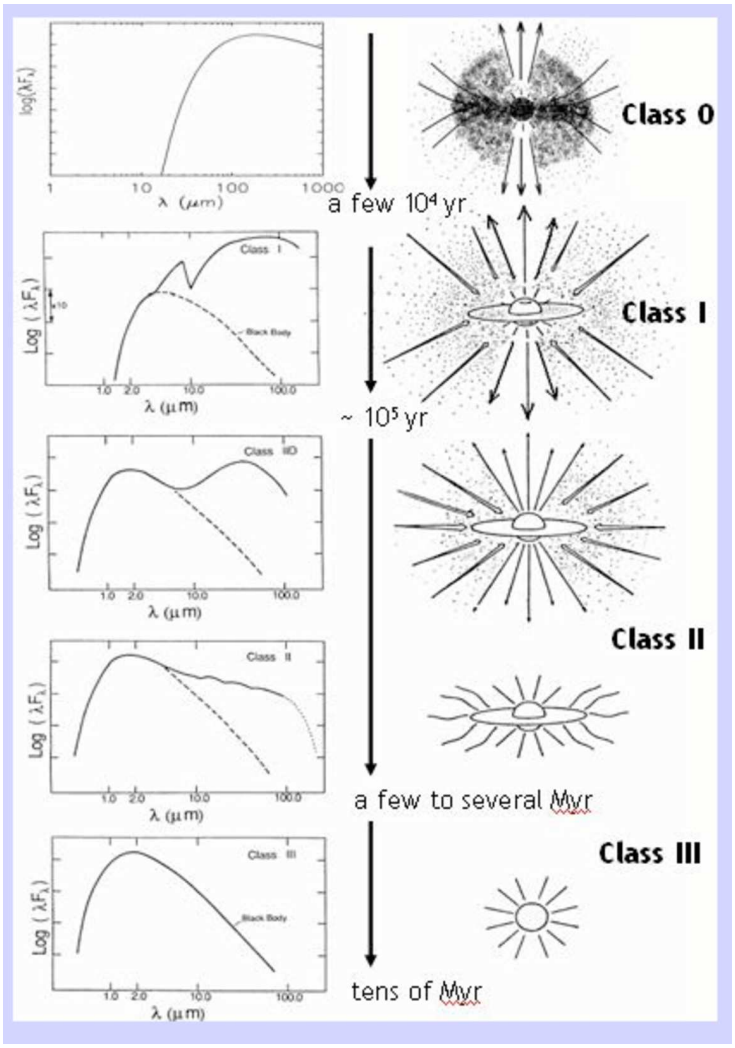

Figure 1.1 Star formation paradigm for low and intermediate mass stars. The left-half panel shows the spectral energy distribution at various stages of star formation and the right-half panel shows the corresponding source geometry (Wilking [1989]; Furlan [2006]).

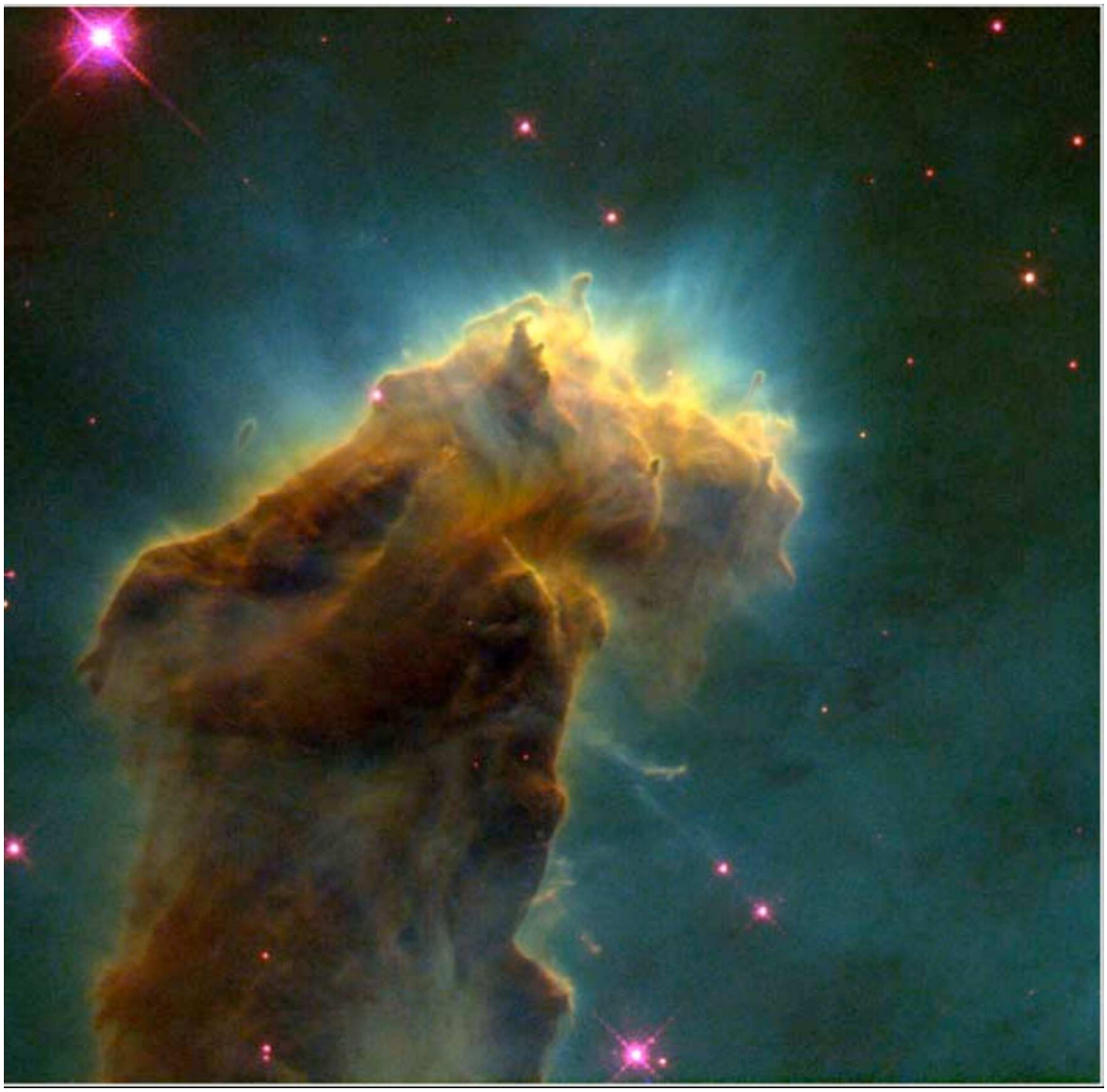

Figure 1.2 Hubble image of the M16 (Eagle Nebula) courtesy NASA/ESA/STScI.

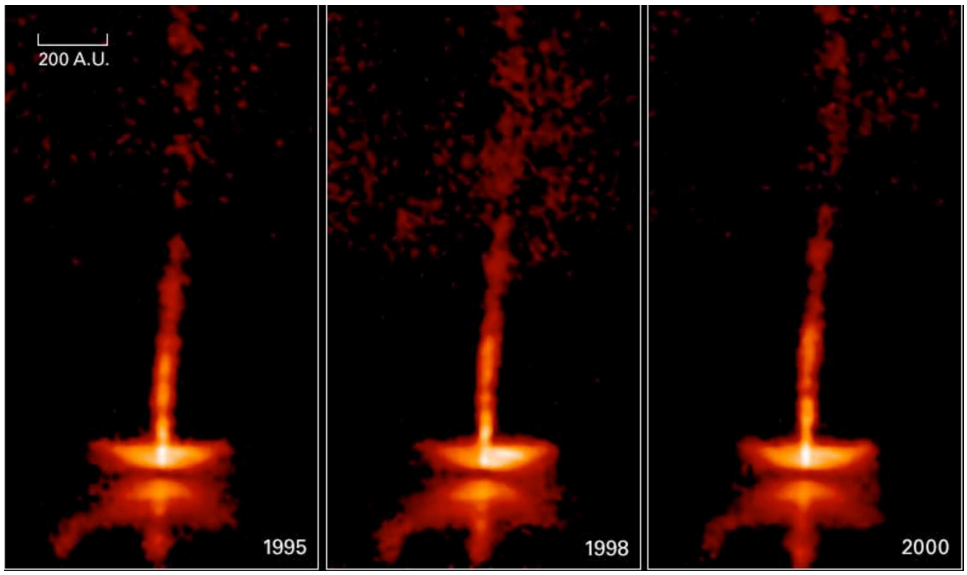

Figure 1.3 Hubble images of the edge on Herbig Haro object HH30. The images show variations in the jet structure over a 5 year period (credits NASA/ESA/STScI, Burrows et al. [1996]).

Figure 1.4 AB Aurigae in scattered light (Grady et al. [1999]). The disk shows spiral arms.

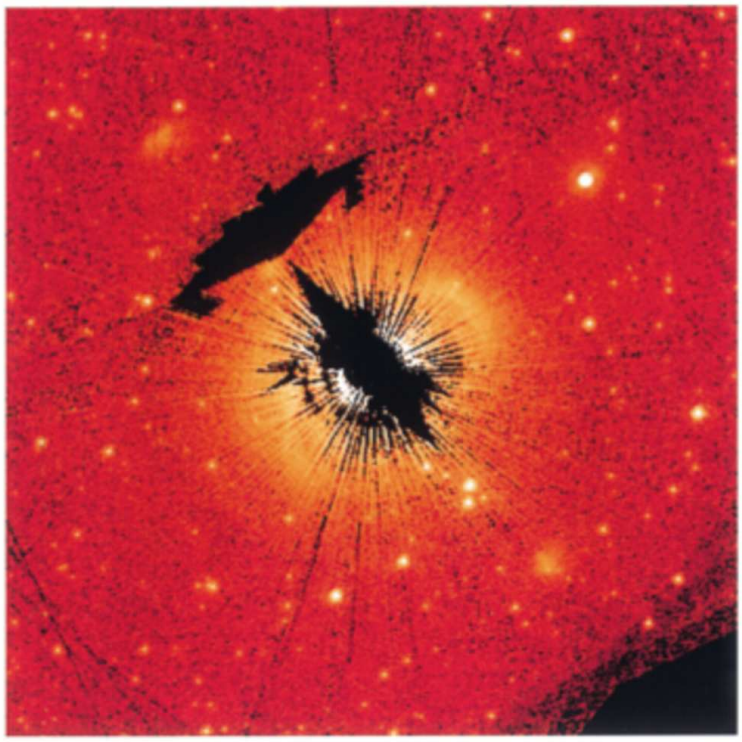

Figure 1.5 MWC275 in scattered light (Grady et al. [2000]). The disk has a number of rich structural features.

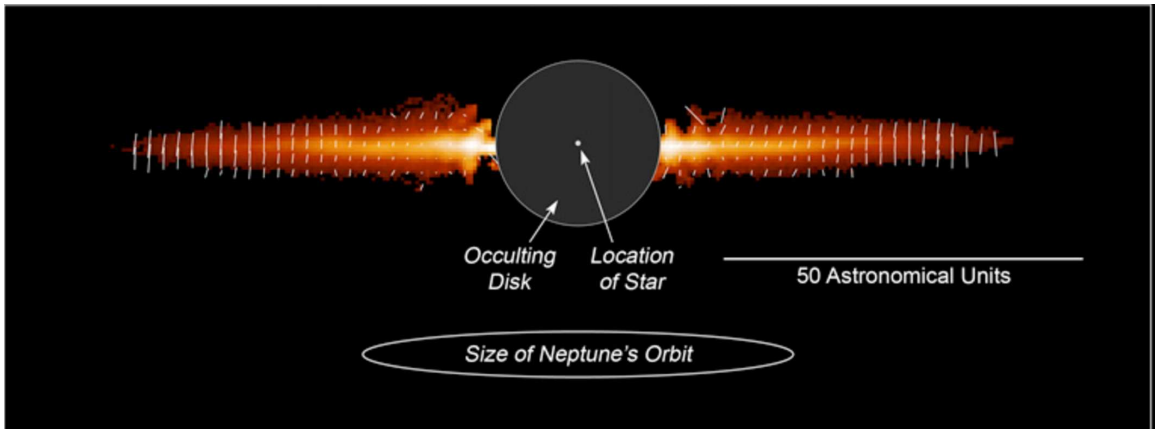

Figure 1.6 Reflected light from the debris disk around AU Mic (Krist et al. [2005]).

1.3 Circumstellar Disks in Herbig Ae Stars

Dust plays the dominant role in setting the thermal structure of CSM because of its much higher opacities compared to gas. Keeping this in mind, we now proceed to describe disk models for Herbig Ae stars.

In a pioneering study, Hillenbrand et al. [1992, hereafter HSVK92] tried to observationally constrain accretion rates for a number of Herbig Ae/Be stars. The near-infrared(NIR) excess above photospheric levels in these systems (see Fig 1.7) were interpreted as arising from geometrically flat, optically thick accretion disks ("the standard disk") - a model already adopted for the T Tauri case (Fig 1.8). Hartmann et al. [1993] argued that the accretion rates reported in HSVK92 were too high and would cause significant optical veiling in these systems which was not observed. Furthermore, Millan-Gabet et al. [1999, 2001] showed that standard accretion models predicted NIR sizes that were too small to explain the NIR sizes of Herbig Ae stars (Fig 1.9). Early interferometry results (Millan-Gabet et al. [1999, 2001]; Tuthill et al. [2001]; Monnier & Millan-Gabet [2002]) suggested that the dust disk gets truncated at a finite radius (determined primarily by the luminosity of the central star and dust sublimation temperature) within which the temperature is too high for dust to survive, creating an optically thin cavity surrounding the star. The truncated disk forms a 'rim' (Natta et al. [2001]; Dullemond et al. [2001]) that subtends a significant solid-angle around the star and intercepts stellar photons, re-radiating predominantly in the NIR. The disk-like nature of the 'rim' was confirmed by Eisner et al. [2003] and Eisner et al. [2004].

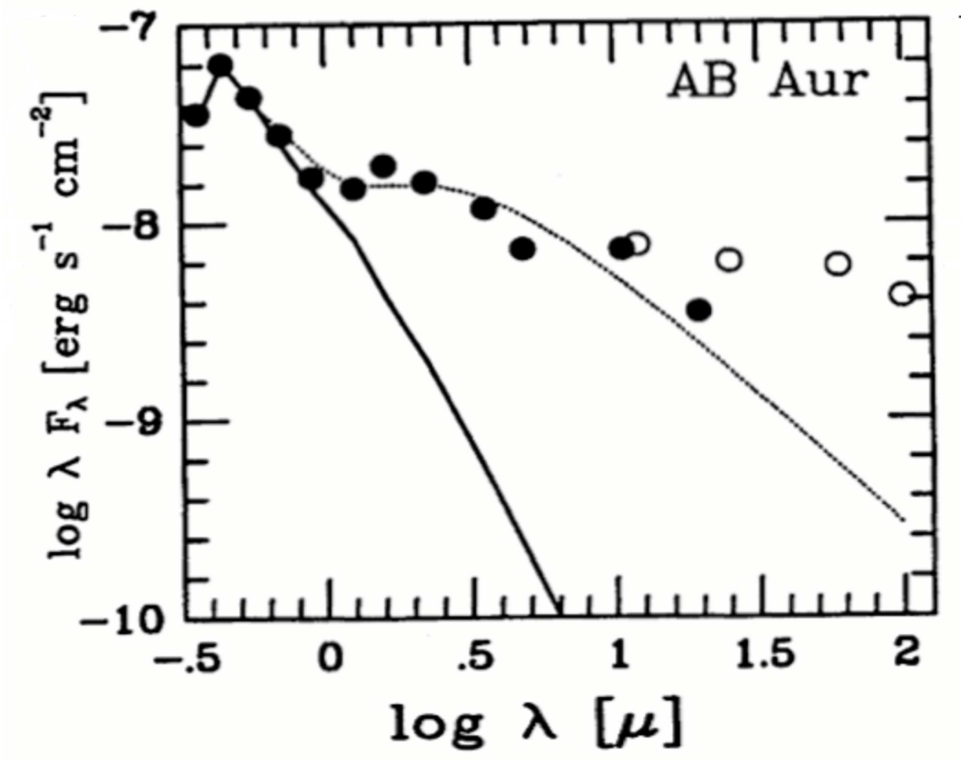

Figure 1.7 The SED of AB Aur (Hillenbrand et al. [1992]). Solid circles are ground based observations and open circles represent IRAS points. The solid line shows stellar photospheric emission. The dotted line is the "best fit" disk model.

1.3.1 Dullemond Model

Motivated by the need to have a physical mechanism that explains the NIR bump in Herbig Ae stars, Natta et al. [2001] and Dullemond et al. [2001] proposed a passive disk model which has become the currently favored theoretical model. In this model, the structure of the circumstellar disk is set by a balance between stellar gravity and the pressure gradient created from the heating of disk material by stellar photons. The model divides the disk into 3 regions (see Fig 1.10) -

- **Inner Rim** Sufficiently close to the star (distance depends on stellar luminosity and dust properties), dust in the circumstellar disk reaches sublimation temperatures and evaporates inside of which the disk is optically thin. The

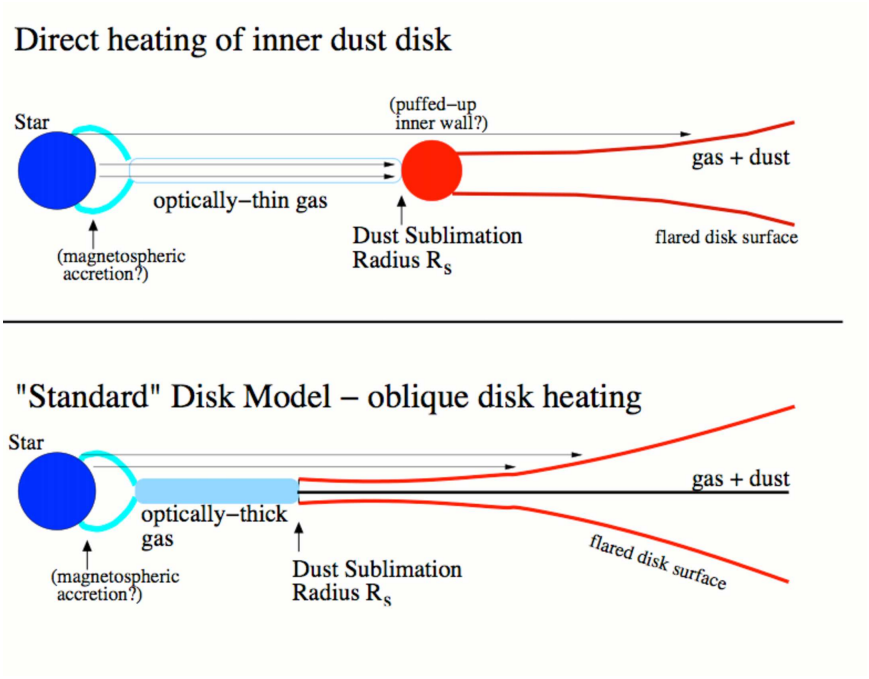

Figure 1.8 Schematic for passive (top) and active (bottom) disk models. (Figure from Monnier et al. [2005])

truncated dust disk is frontally illuminated by the star and forms a 'rim'. The rim puffs up, traps a significant fraction of stellar photons and re-radiates predominantly in the NIR. For an A0 star and a dust sublimation temperature of $\sim$ 1500K, the radius of the inner rim is $\sim$ 0.35 AU.

The major success of this model has been the correct prediction of the NIR size-luminosity diagram for YSOs (Monnier & Millan-Gabet 2002, Millan-Gabet et al. 2007). According to the model, NIR size $\propto L^{0.5}$. Fig 1.11 shows a comparison between theoretical predication and observations.

- **Shadow Region** The inner rim casts a geometric shadow on the region behind it, preventing it from receiving direct star light. The disk in the shadow is heated by scattered photons from the rim edge and through radial heat diffusion. The size of the shadow can be several AU depending on the rim

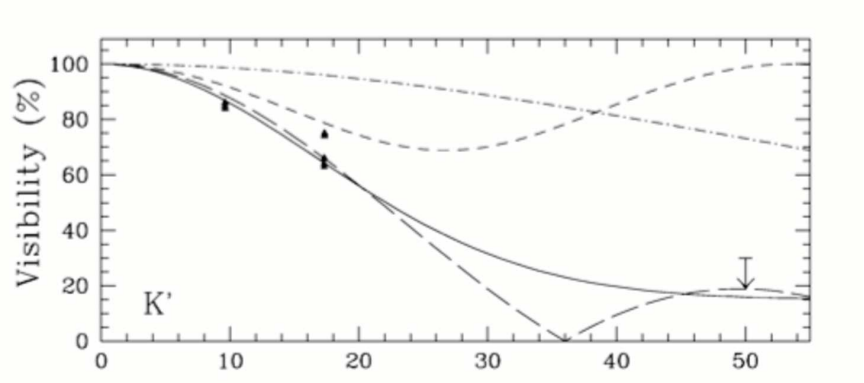

Figure 1.9 K-Band visibilty data on AB Aur (Millan-Gabet et al. [1999]). The dashed-dotted line shows the predicted visibility for a "classical" accretion disk model. The long-dashed line is the visibility for a dust "rim" model. The dashed line represents a binary model and the solid line is a Gaussian disk.

geometry, the mass of dust in the outer disk and dust grain properties in the outer disk. The shadow corresponds to the terrestrial planet forming region in circumstellar disks.

- **Flared Disk** If sufficient dust is present in the outer disk, the disk eventually emerges from the shadow and "flares". The flared disk can be a few hundred AU in size and emits radiation in the MIR and longer wavelengths.

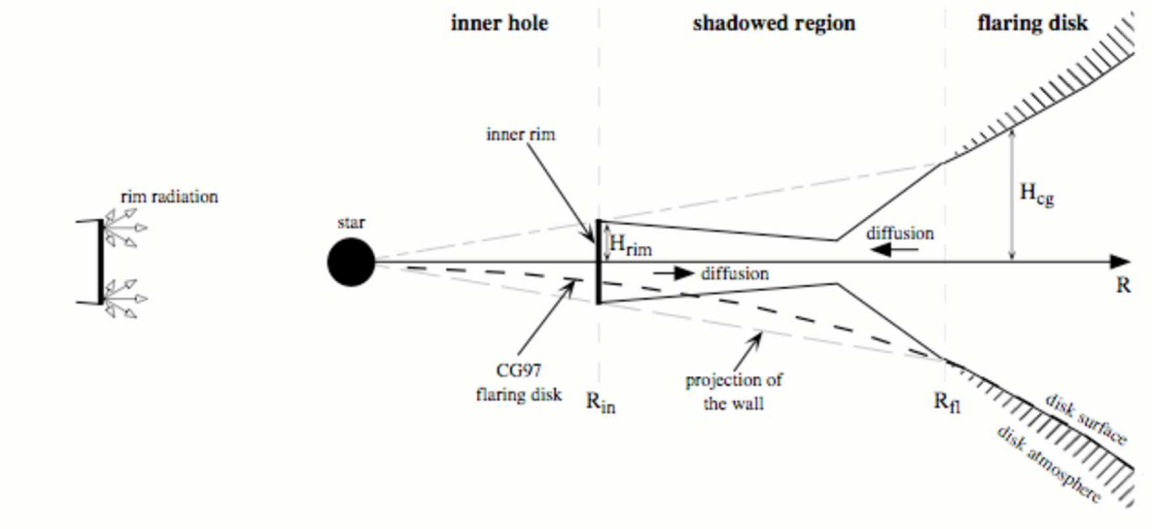

Figure 1.10 The Dullemond (Dullemond et al. [2001]) passive disk model.

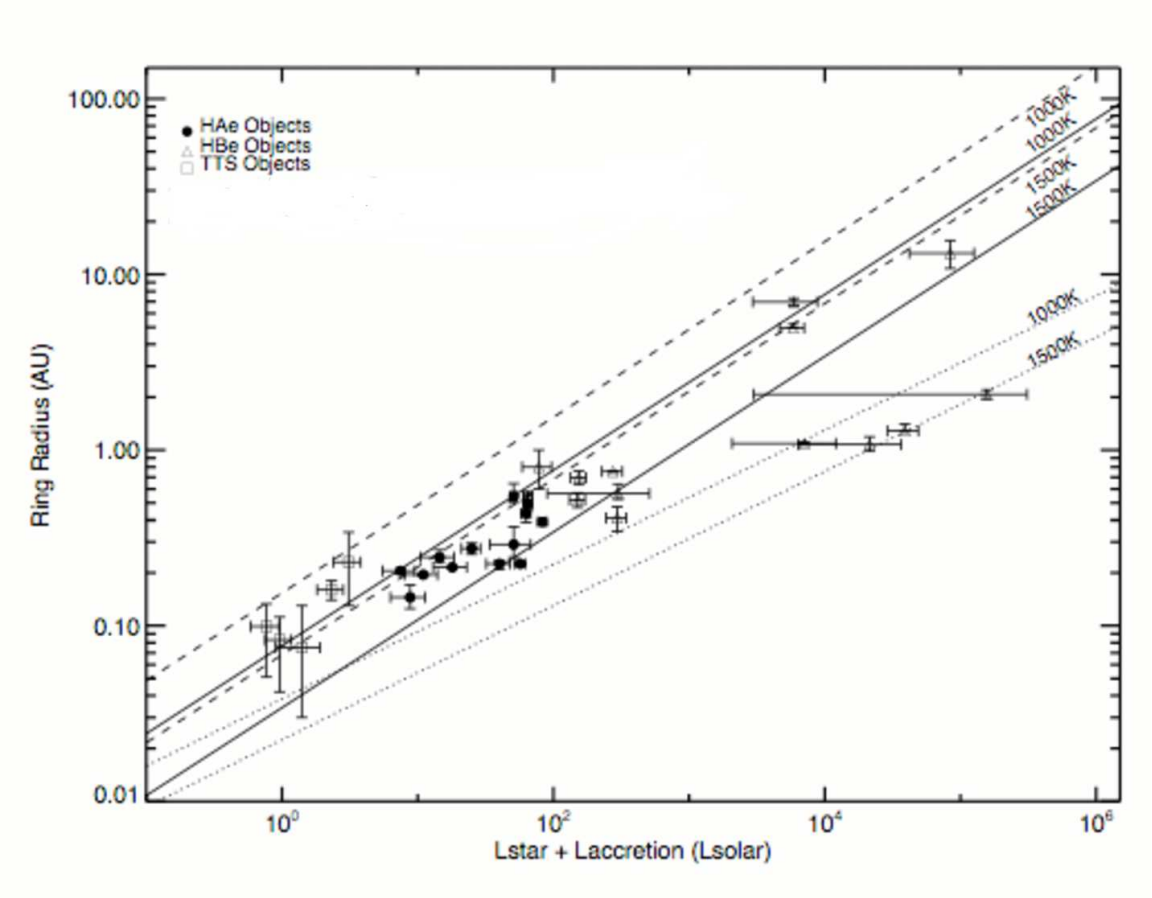

Figure 1.11 The NIR size luminosity diagram (Millan-Gabet et al. [2007]). The solid (no backwarming) and dashed lines (with backwarming) are the sublimation radii for dust directly heated by the central luminosity. The dotted lines are sublimation radii for the oblique heating implied by classical accretion disk models.

Meeus et al. [2001] analyzed the ISO MIR spectra of a sample of Herbig Ae stars and found they could be grouped into two distinct categories - Groups I & II. The MIR continuum in Group I sources could be fit with a power-law + a black-body fit, whereas the Group II sources could be fit with a power law alone (Fig 1.12). In producing disk models in radiative and vertical hydrostatic equilibrium, Dullemond & Dominik [2004] realized that depending on the structure of the inner rim and dust properties in the outer disk, the outer disk surface can assume two geometries (i)

Flared disk, where the disk emerges from the shadow of the inner rim (Fig 1.13) (ii) Self-shadowed disk, where the disk fails to emerge out of the rim shadow (Fig 1.14). The flared disk SED matches the SED of Group I sources and the self-shadowed disk SED matches the SED of Group II sources. This physical connection has gotten support from recent modeling work on VV Ser by Pontoppidan et al. [2007]. The size and shape of the dark wedge in VV Ser PAH emission (Fig 1.15) was used to infer the existence of a shadowed disk in VV Ser.

In summary, the DDN01 model has been partly successful in explaining the SED of Herbig Ae stars (from UV to millimeter wavelenghts) and their NIR interferometric sizes. The model has sufficient structure and complexity to provide physical interpretation to the Meeus Groups I and II classification of YSOs. UX Orionis phenomena (Dullemond et al. [2003b]) have also been interpreted in terms of the DDN01 model.

1.4 The power of Interferometry in exploring HAe/Be disk structure

Circumstellar disks around YSOs emit from the NIR to mm wavelengths (Fig 1.7). To first order, the emission traces the disk temperature structure, with NIR emission arising in the hot inner region at fractions of an AU from the star and mm emission arising from the cold outer disk at length scales of several hundred AU. At a distance of 100 parsecs (typical of the nearest star forming regions) the emission scales correspond to angular resolutions between $\sim$2 milli-arcseconds (for NIR emission) and $\sim$2 arcseconds (for mm emission). Long-baseline interferometry is the ideal tool for

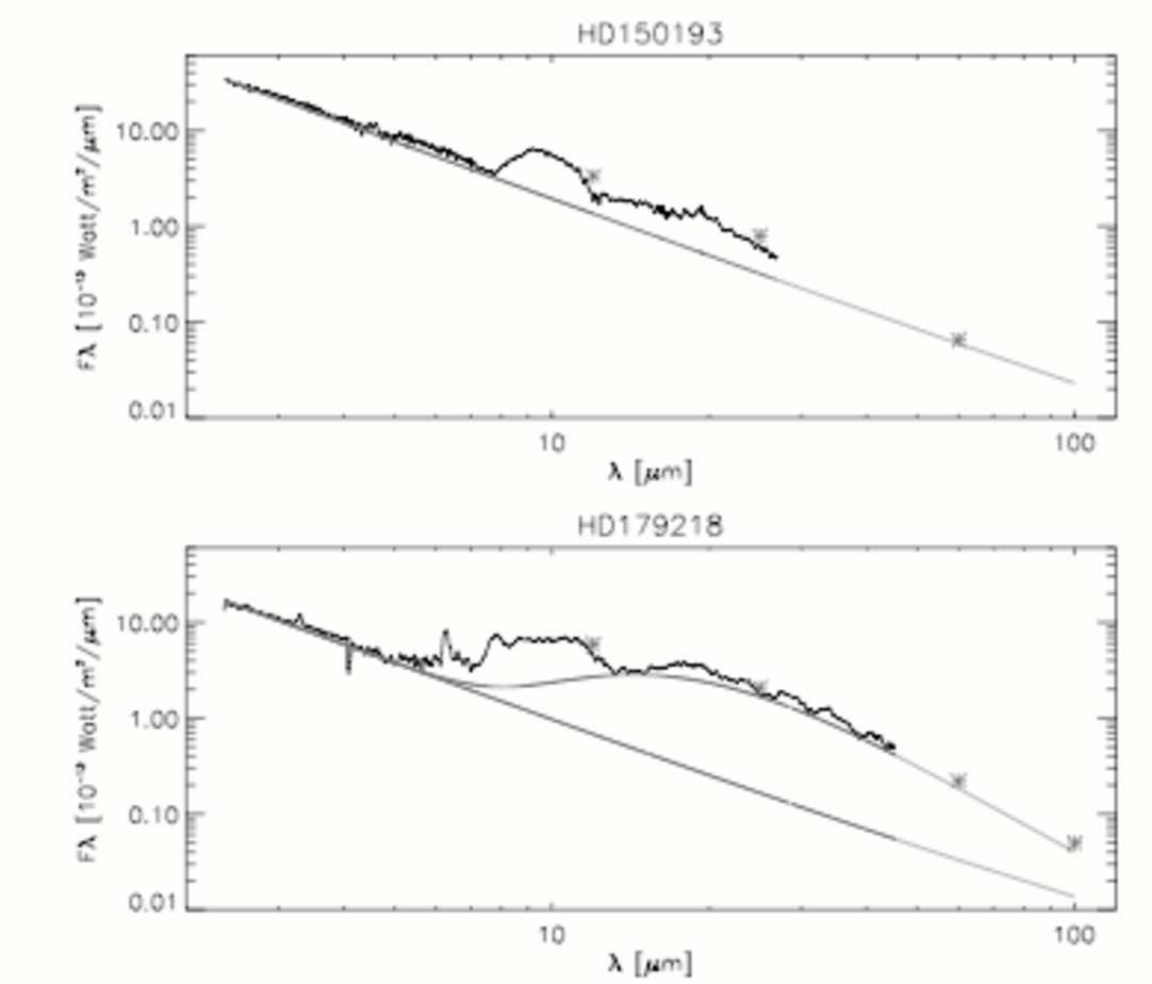

Figure 1.12 SED for Meeus Group II and Group I sources (Meeus et al. [2001]). The mid-infrared SED of Group II sources can be fit with a power law, and that of Group I sources with a power law + black-body.

probing proto-plantery disk structure at such high angular resolution.

Over the last decade infrared and millimeter interferometry have drastically improved our understanding of the physical structure (temperature and density) of circumstellar material (CSM) around HAe/Be stars. Mannings & Sargent [1997] resolved the CSM around a number of YSOs in the mm, detecting elongated structures, and finding observational evidence for the CSM to be in a disk-like structure. CO emission-line profiles (Mannings & Sargent [1997]; Corder et al. [2005]; Isella et al.

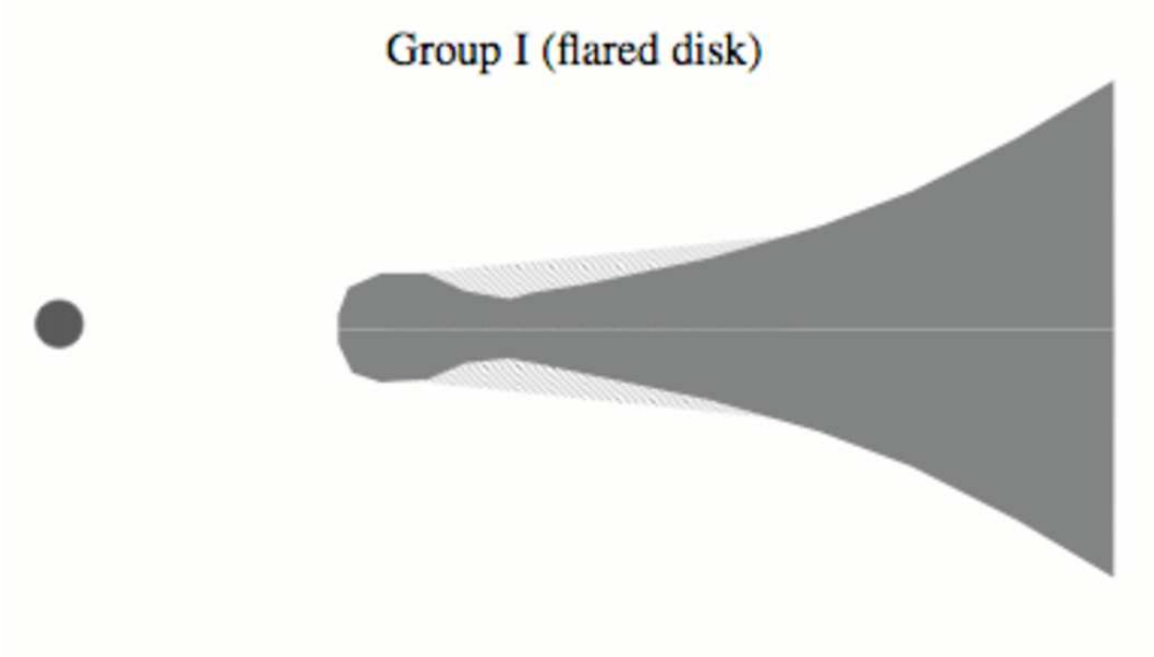

Figure 1.13 Flared Disk (Dullemond et al. [2003b]). The Group I mid-infrared SED has been interpreted in terms of the flared disk model.

[2007]) display signatures of Keplerian rotation around the central star, further evidence for CSM disk morphology. Arcs and spiral arms (e.g. Corder et al. [2005]; Lin et al. [2006]) have been observed in a number of disks providing evidence for strong dynamical effects in YSO systems. Millimeter-wave interferometry also provided the first measurements on the extent of the CSM constraining it to be several hundred AU.

MIR emission probes the planet formation region in circumstellar disks (Chiang & Goldreich [1997]; Dullemond et al. [2001]) with the emission arising from warm dust (T >150K). The MIR sizes of YSO disks were first obtained with VLTI/MIDI for a sample of seven HAe/Be stars by Leinert et al. [2004]. The sizes were found to correlate with the source IRAS colors, and this correlation was interpreted in terms of Group I and Group II sources, with flared disks being larger and redder than

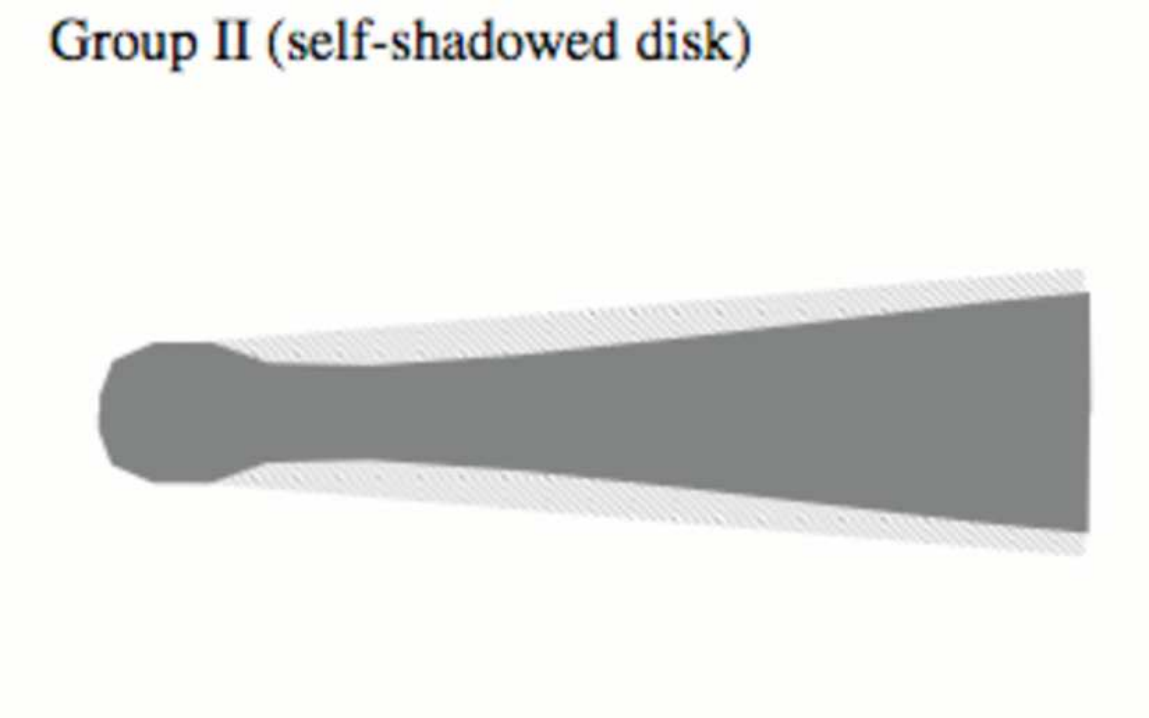

Figure 1.14 Self-shadowed Disk (Dullemond et al. [2003b]). The Group II mid-infrared SED has been interpreted in terms in terms of the shadowed disk model.

shadowed disks (see Figs 1.13 and 1.14). van Boekel et al. [2004] used spectrally resolved MIR interferometry to show radial gradients in dust crystallinity, particle size and chemical composition in circumstellar disks (Fig 1.16). The MIDI observations revealed that that the inner 1-2 AU is much more crystalline than the outer 2-20AU, which in turn is significantly more crystalline than the inter-stellar medium (see Millan-Gabet et al. [2007] for details).

Thermal NIR emission probes hot regions (typically inner AU) of the disk with temperatures greater than 700K. Early NIR interferometry results (Millan-Gabet et al. [1999, 2001]; Tuthill et al. [2001]; Monnier & Millan-Gabet [2002]) changed our picture of the gas dust transition region (Figs 1.8 and 1.9) and highlighted the importance of passive stellar heating in establishing disk structure. Furthermore,

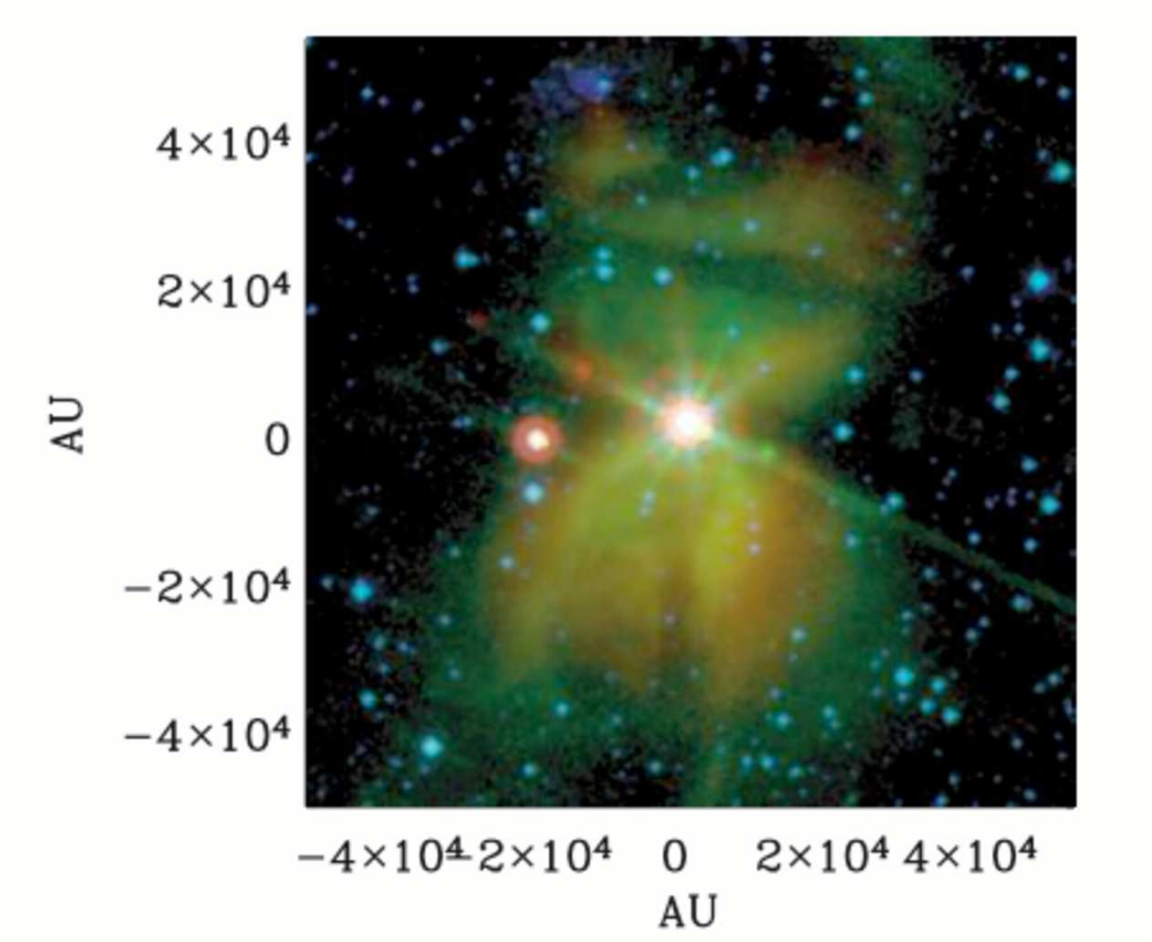

Figure 1.15 VVSer imaged in PAH emission (Pontoppidan et al. [2007]). The shape and size of the dark wedge has been used to infer the existence of a disk shadow in VV Ser.

Monnier et al. [2006] showed that the first generation vertical rim model (Fig 1.10) lacked the necessary physics to explain closure phase observations of YSOs with the IOTA interferometer. More recently, Tatulli et al. [2007] and Kraus et al. [2008b] (using VLTI/Amber) demonstrated that Brγ emission lines attributed to the magnetospheric in-fall of gas onto the central star (Muzerolle et al. [1998]), can sometimes arise in the disk or in a wind (Fig 1.17). This result is motivation for further developing spatially resolved probes of stellar accretion.

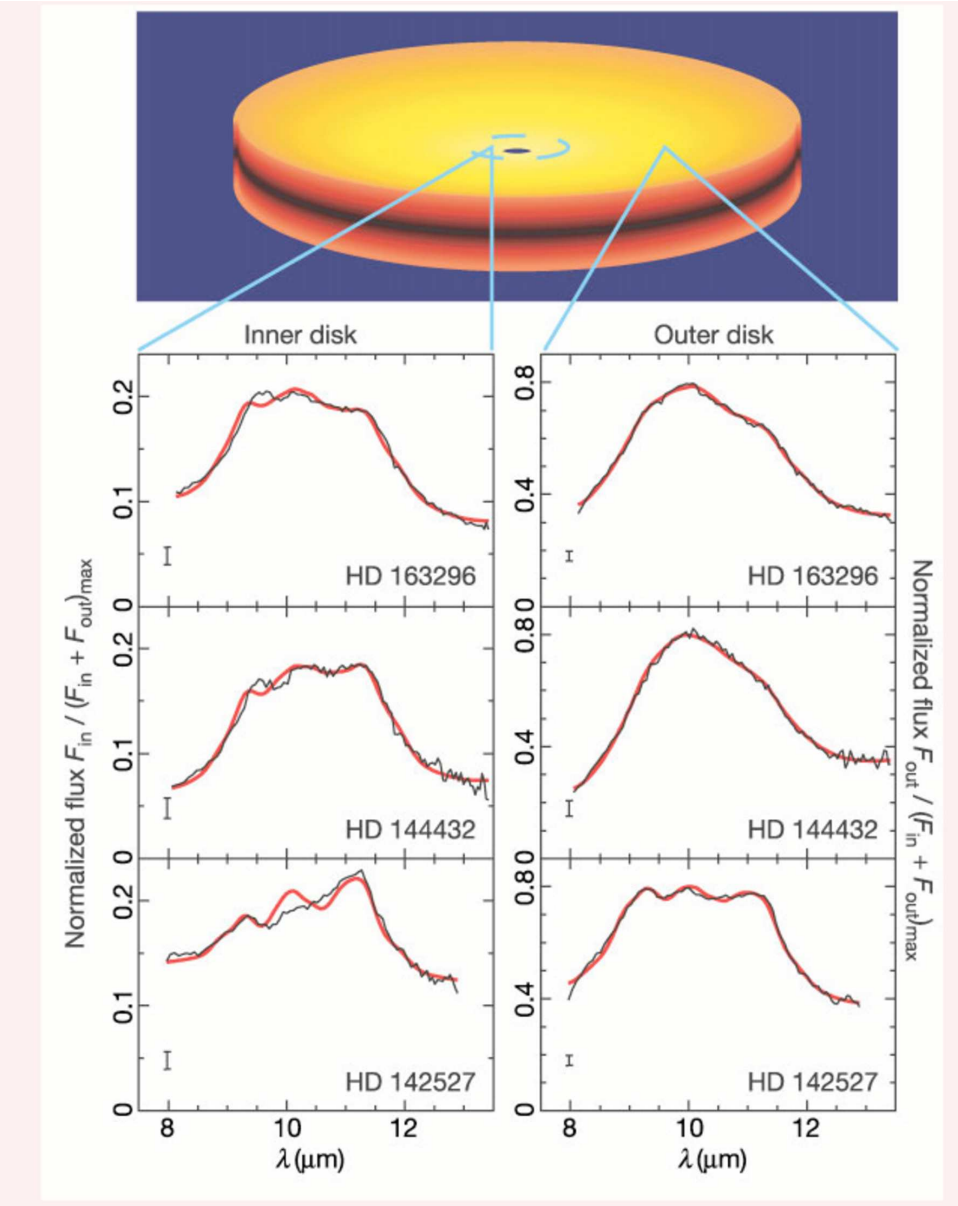

Figure 1.16 Spatially-resolved MIR spectra of HAe stars (van Boekel et al. [2004]). The left-half panel shows the spectrum for the inner disk (1-2AU) and the right-half panel shows the spectrum for the outer (2-20AU) disk. The broadening of the feature in the inner-disk spectra indicates grain growth and the resonance at 11.3μm indicates the presence of crystalline silicates.

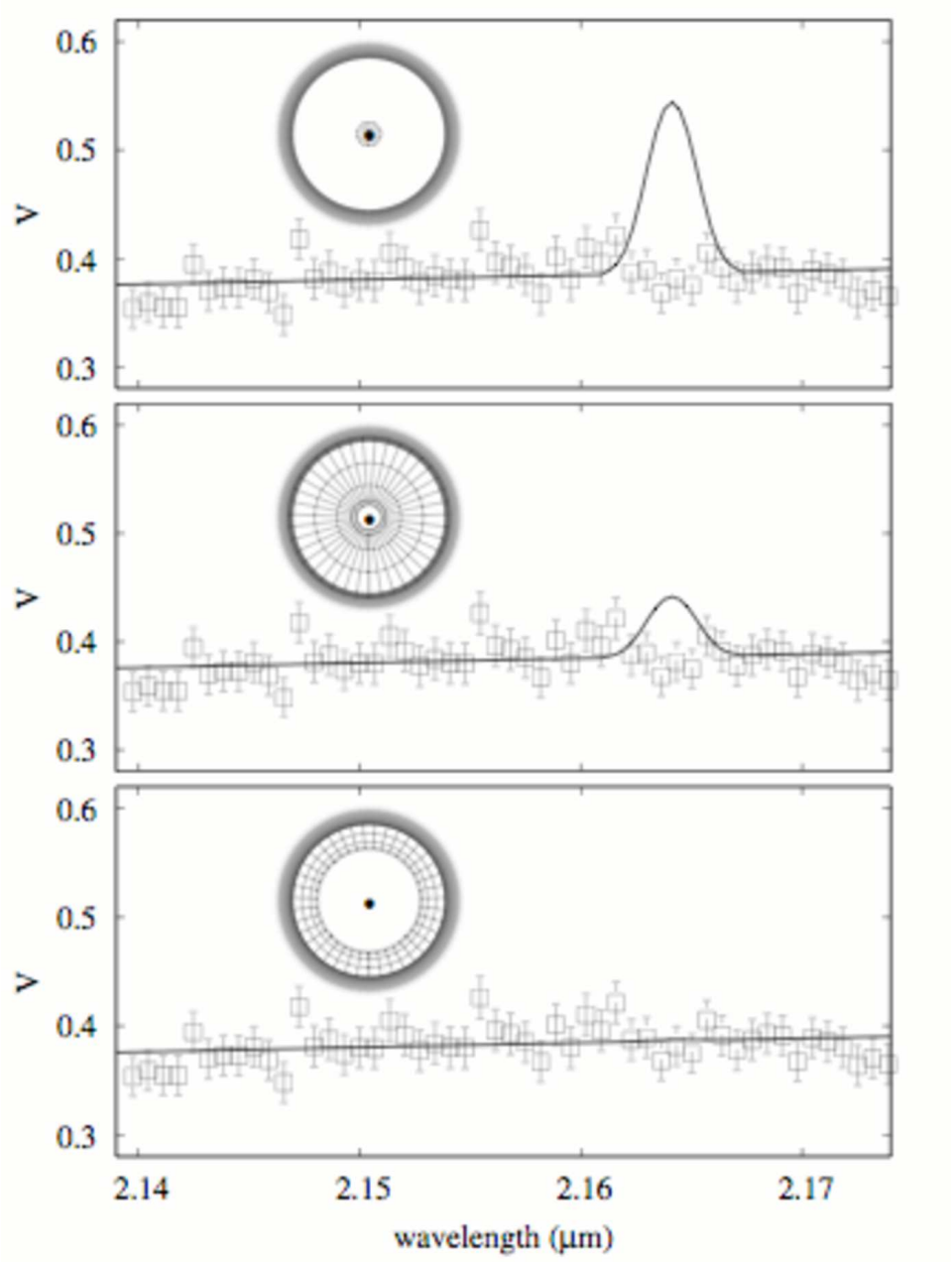

Figure 1.17 Brγ emission in Herbig Ae star HD104237 (Tatulli et al. [2007]). The empty squares are observed visibility points and solid curves are predictions for simple geometric models. The continuum emission arises from the central star and the dust rim shown as a grey scale ring. The Brγ emission regions are shown as a grid surface. In the upper panel, Brγ emission arises in a magnetospheric accretion column close to the star inside the co-rotation radius. The Brγ emission arises between the co-rotation radius and the dust rim in the middle panel. In the bottom panel, the emission arises close to the dust rim.

1.5 Overview of the Thesis

My thesis focuses on obtaining a detailed understanding of the structure of the inner tens of AU in circumstellar disks around HAe stars using a combination of NIR interferometry from CHARA, mid-infrared (MIR) interferometry from the Keck Segment Tilting Experiment, and state-of-the-art radiative transfer models. Figure 1.18 is an illustration of the models used in interpreting the data.

In Chapter 2, we describe self-consistent Monte Carlo radiative transfer models of the gas-dust transition (the evaporation front) in circumstellar disks. Observational and theoretical developments over the last couple of years have shown the the evaporation front is significantly more complicated than the vertical wall (Figs 1.10 and 1.18) assumed in Dullemond et al. [2001]. The front shape depends sensitively on dust properties and can be used as a probe of dust physics operating in circumstellar disks.

Chapter 3 gives a brief description of the CHARA instrument and presents a comparison between theoretical inner rim models and CHARA NIR interferometry on MWC275 and AB Aur. We report the presence of additional NIR opacity inside the "conventional" dust destruction radius (see Fig 1.18, bottom panel).

Chapter 4 deals with the thermal MIR region of circumstellar disks. The effects of inner-rim structure on the MIR disk in YSOs are investigated. We describe the Keck Segment Tilting Experiment and attempt at generating models that explain trends between stellar properties, disk flaring parameters, and the observed disk properties in the MIR. In this chapter, we also study the structure of the circumbinary disk around V892Tau.

Chapter 5 is the essence of this thesis and presents models (Fig 1.18) that simultaneously explain the long-baseline interferometry (from NIR to mm) and the SED (from UV to mm) for Herbig Ae stars MWC275 and AB Aur. We show that despite similar stellar properties, and nearly identical NIR disk structure, MWC275 and AB Aur have remarkably dissimilar MIR morphology. We suggest that the difference in MIR morphology arises due to the presence/absence of dynamical processes (like planetesimal collisions) in the outer disk.

Chapter 6 is the final chapter and here we summarize our results, discuss open questions and outline exciting future prospects for understanding the open issues.

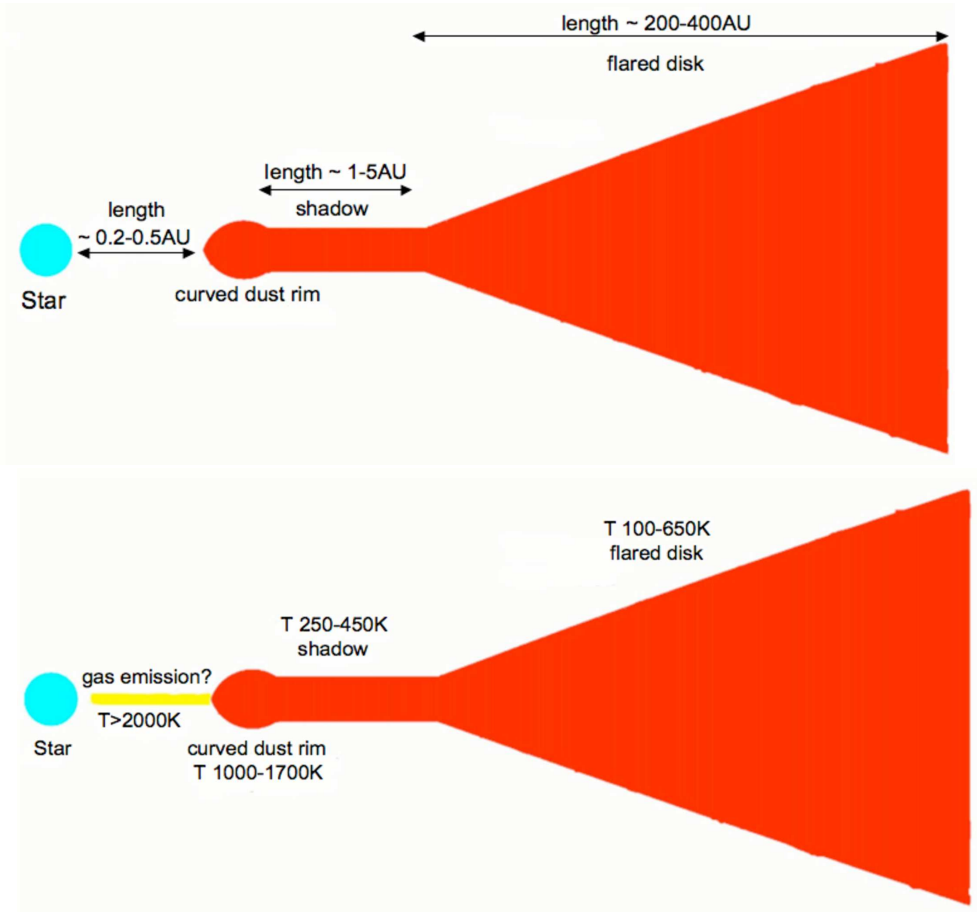

Figure 1.18 Schematic of disk models. a)Top panel. Flared disk with a curved inner rim. The typical size for each of the regions in the disk is indicated. b) Bottom panel. An additional "smooth" emission component (presumably gas) has been added inside the dust destruction radius to explain MWC275 and AB Aur NIR photometry and interferometry. The typical temperatures in the photosphere of each of the disk regions is indicated.
Note: The models are not to scale.

Chapter 2

Self-consistent Models for the Gas-Dust Transition Region

Abstract: Dust-grain growth and settling are the first steps towards planet formation. An understanding of dust physics is therefore integral to a complete theory of the planet formation process. In this chapter, we explore the possibility of using the dust evaporation front in YSO disks ('the inner rim') as a probe of the dust physics operating in circumstellar disks. The geometry of the rim depends sensitively on the composition and spatial distribution of dust. Using radiative transfer and hydrostatic equilibrium calculations we demonstrate that dust growth and settling can curve the evaporation front dramatically (from a cylindrical radius of about 0.5 AU in the disk mid-plane to 1.2 AU in the disk upper layers for an A0 star). We compute synthetic images and interferometric visibilities for our representative rim models.

2.1 Introduction

Advances in long-baseline near-infrared (NIR) interferometry have made it possible to study the inner regions of circumstellar disks at sub-AU scales. Early results (Millan-Gabet et al. [1999, 2001]; Tuthill et al. [2001]; Monnier & Millan-Gabet [2002]) have shown that the dust disk gets truncated at a finite radius (determined by the luminosity of the central star and dust sublimation temperature) within which

the temperature is too high for dust to survive. The truncated disk forms a 'rim' (Natta et al. [2001]; Dullemond et al. [2001, hereafter DDN01]) that subtends a significant solid-angle around the star and intercepts stellar photons, re-radiating predominantly in the NIR. This rim naturally explains the NIR excess observed in Herbig Ae systems.

Despite its success in accounting for the near-IR excess, the vertical rim model introduced in DDN01 has had a few weaknesses from the very outset. The flux received from a vertical rim is highly viewing-angle dependent (see Fig 2.1), since the projected line-of-sight area of the rim changes rapidly with inclination angle. This implies that the near-IR spectral energy distributions (SEDs) of Herbig Ae/Be stars should be a strong function of inclination angle, but observations show that most Herbig Ae stars have similar near-IR excesses, independent of their inferred inclination angles (Natta et al. [2001]; Dominik et al. [2003]). Furthermore, the surface brightness distribution of a vertical rim will become highly asymmetric at inclination angles different from face-on (Fig 2.1). This asymmetry should be detectable by interferometers in the form of a closure-phase signal (Monnier [2000, and references therein]), but recent studies (Monnier et al. [2006]) do not detect significant closure-phase signals indicating that the geometry of the inner rim is not a vertical wall.

It appears that a mechanism that curves the inner rim is needed. Isella & Natta [2005] (hereafter IN05) studied the impact of density-dependent dust sublimation temperatures on the structure of the rim. Close to the mid-plane, where the densities are high, the dust sublimation temperatures are also high (Pollack et al. [1994]),

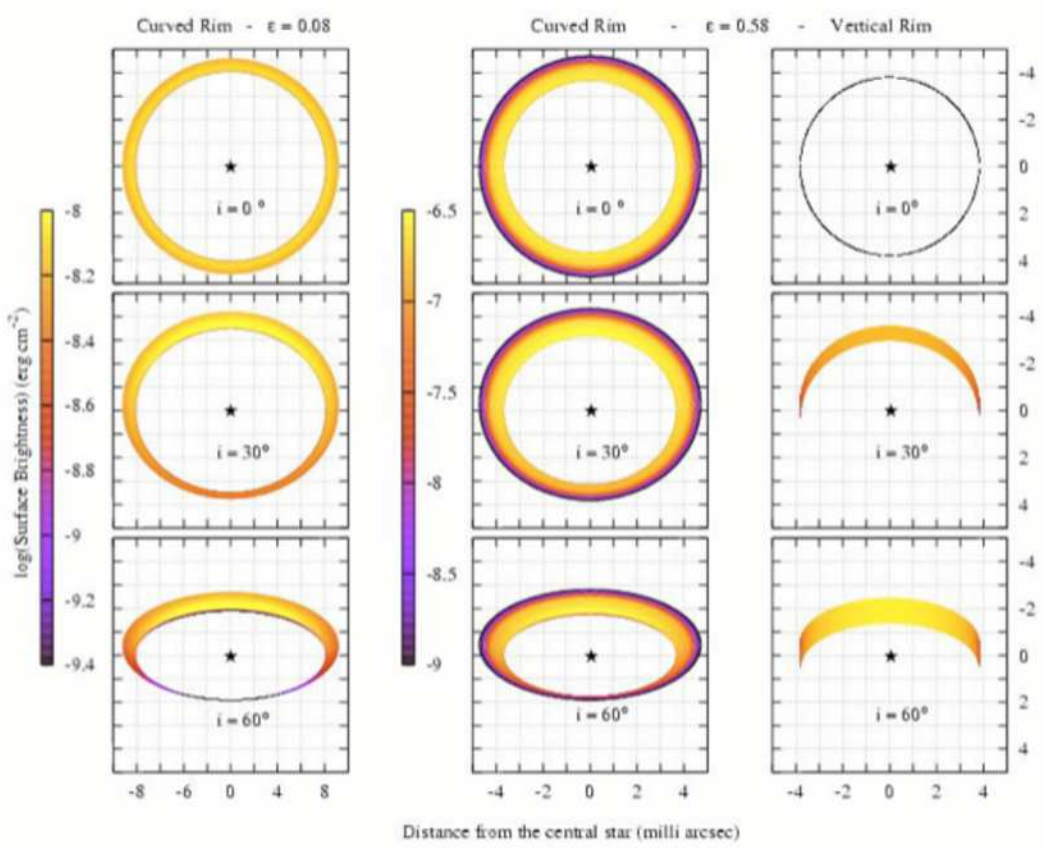

Figure 2.1 Synthetic images for rim models showing effects of inclination. The left and the center panel are curved rim models from Isella & Natta [2005]. The right panel shows the vertical rim model from Dullemond et al. [2001]. (Diagram from Isella & Natta [2005])

while as the densities begin to fall rapidly in the vertical direction the sublimation temperatures drop. The IN05 calculations show that this causes the inner rim to curve away (Fig 2.1) from the surface of the star. Isella et al. [2006] found that a curved-rim model provides a substantially better fit to the visibilities and near-IR SEDs of a few Herbig Ae systems.

In this chapter we look at another mechanism that could curve the rim on larger scales than the ones produced by a density-dependent dust sublimation model—namely, dust growth and settling. In the absence of strong turbulence, dust grains

will settle towards the disk mid-plane with large grains settling lower and having a smaller scale height than small grains. Dust grains will also grow rapidly in the mid-plane due to the much higher densities (Dubrulle et al. [1995]; Dullemond & Dominik [2004]; Tanaka et al. [2005]). The opacity in the mid-plane is thus dominated by large grains whereas small grains dominate the opacity higher in the disk photosphere. This transition in the nature of the opacity source along with dust sublimation curves the inner rim as described in Section 4. Near-IR interferometers with baselines several hundred meters long (e.g. CHARA, VLTI) can distinguish between the model presented in this chapter and the IN05 model based on their visibility curves (see §2.4.3), shedding light on dust physics operating at sub-AU scales.

We have computed the structure of the dust evaporation front in a self-consistent manner for the first time in a 2-D geometry (photon scattering has not been included; for effects of scattering on disk structure and SED see Dullemond & Natta [2003]) using the radiative transfer code TORUS (Harries [2000]). In the following section we describe the radiative transfer code, while in section 3 we perform a consistency check by comparing the results for a TORUS generated density-dependent dust sublimation model with IN05 results. In Section 4 we present results for the dust segregation model, followed by a summary of the results and conclusions in Section 5.

2.2 The Monte Carlo Radiative Transfer Code - TORUS

2.2.1 Description of grid and disk structure calculations

The calculations in this chapter were performed using the TORUS Monte-Carlo radiative-transfer code (Harries [2000]; Harries et al. [2004]; Kurosawa et al. [2004]). Radiative

equilibrium is computed using Lucy's (Lucy [1999]) algorithm on a two-dimensional, cylindrical-cartesian adaptive-mesh grid. Storing the opacity and temperature information on an adaptive mesh has particular advantages for the problem considered here, since the accurate determination of temperatures and subsequent SEDs requires an adequate resolution of the effective disk photosphere, whose position is changing spatially both as the dust is sublimated and as the vertical structure of the disk changes as it is iterated towards hydrostatic equilibrium. Using adaptive-mesh refinement (AMR) we are able to subdivide cells near the disk photosphere as the calculation proceeds, ensuring the resolution is maintained at each step.

The initial density structure for the disk calculations is based on the canonical description of the α-disk developed by Shakura & Sunyaev [1973], viz

$$\rho(r,z) = \rho_0 \left(\frac{r}{r_0}\right)^{-\alpha} \exp\left[-\frac{1}{2}\frac{z^2}{h(r)^2}\right] \tag{2.1}$$

where r is the radial distance in the mid-plane, r_0 is some characteristic radius, z is the distance perpendicular to the mid-plane, and $h(r)$ is the scale height, given by

$$h(r) = h_0 \left(\frac{r}{r_0}\right)^{\beta} \tag{2.2}$$

with parameters of $\alpha = 2.625$ and $\beta = 1.125$, giving a radial density dependence of the surface density of $\Sigma(r) \propto r^{-1.5}$. The AMR mesh is divided such that the cells are logarithmically spaced in the radial direction and that there are at least 7 cells in the vertical direction per disk scale height $h(r)$. A sweep of the grid is then made to split cells further around the $\tau_{5500} = 1$ (τ_{5500} is the optical depth calculated at 5500 Å) surface using the following algorithm: for each pair of adjacent AMR cells the individual optical depths across the cells are calculated (τ_1 and τ_2

say, with τ_1 referring to the more optically thick of the two). The more optically thick cell is subdivided providing that $\tau_2 < \tau_{\rm min}$ and $\tau_1 > \tau_{\rm max}$, where $\tau_{\rm min}$ and $\tau_{\rm max}$ are parameters (typically 0.1 and 0.5 respectively). Should any cell in the grid be subdivided, the sweep is repeated until no new cells are added to the mesh.

Once the temperature (we assume that the disk is in local thermodynamic equilibrium and gas and dust are thermally coupled, Kamp & Dullemond [2004]) and dust sublimation (see next section) structures have converged using the Lucy algorithm, the vertical disk structure is modified via the equation of hydrostatic equilibrium following a similar algorithm to that detailed by Walker et al. [2004]. Briefly, and assuming that the disk mass is negligible compared to the central star, the equation of hydrostatic equilibrium is

$$\frac{{\rm d}P}{{\rm d}z} = -\rho g_z \tag{2.3}$$

where P is the pressure, ρ is the density and g_z is the vertical component of the stellar gravity. Adopting an ideal gas equation of state $P = \rho kT/\mu m_{\rm H}$ (with $\mu = 2.3$ for a standard molecular hydrogen-helium mixture) we get

$$\frac{{\rm d}\rho}{{\rm d}z}\frac{1}{\rho} = -\frac{1}{T}\left(\frac{g_z \mu m_{\rm H}}{k} + \frac{{\rm d}T}{{\rm d}z}\right). \tag{2.4}$$

The above equation can be solved for $\rho(z)$ numerically on the AMR mesh since the vertical temperature structure is known from the radiative-equilibrium calculation. The vertical density structure is then renormalized to conserve the radial surface density profile detailed above. A self-consistent calculation for dust sublimation (see 2.2.2) and disk temperature followed by a hydrostatic equilibrium calculation is repeated until the disk density structure has converged. Convergence is typically

achieved in four iterations. Images and SEDs are subsequently calculated using a separate Monte Carlo algorithm based on the dust emissivities and opacities (Harries [2000]).

2.2.2 Implementation of Dust Sublimation.

In the models discussed here the shape of the inner rim is controlled by dust sublimation. Typical mid-plane densities in the dust sublimation region are of the order of $10^{-8} - 10^{-10}$ g cm^{-3} in Herbig disks. In the mid-plane, an optical depth of unity for visible light photons (measured radially inward into the disk from the rim edge) corresponds to a length scale of $\sim 10^{-5} - 10^{-7}$ AU. Therefore if we started sublimation runs with a grid that had the full dust opacity present, convergence towards an equilibrium rim shape would be extremely slow. This is very similar to the problem encountered in photoionization codes, where neutral hydrogen opacity to ionizing photons is so large that starting from a neutral grid would take an impractical amount of CPU time for the Strömgren sphere to propagate outwards (Wood et al. [2004]).

The solution that we adopt is also analogous to the one used in photoionization codes (Wood et al. [2004]). The dust content is first reduced to a very low value in the computational grid for the circumstellar disk, to make each of the grid cells optically thin. Stellar photons then propagate through the disk and the temperature of grid cells is determined. Dust is added to cells that are cooler than the sublimation temperature in small steps of τ. The step size is a τ of 10^{-3} (computed at 5500Å) for the first five dust growth steps. The step size is then increased logarithmically, first to 10^{-2}, then to 10^{-1} and so on until the appropriate gas to dust ratio is reached in each

grid cell. The grid cell temperatures are recomputed after every dust growth step and the process is repeated until the shape of the dust sublimation region converges.

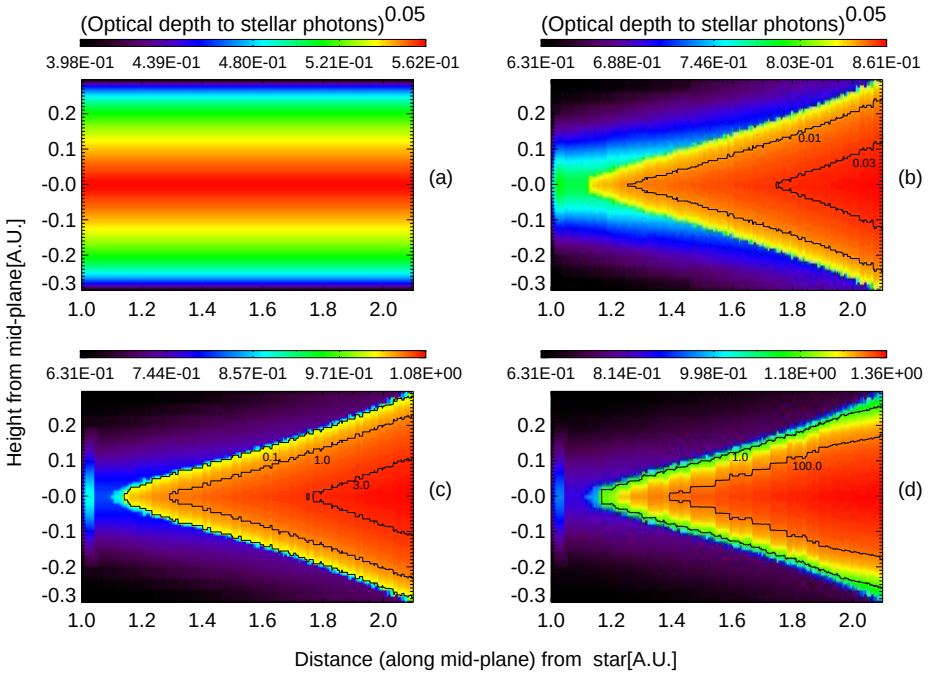

Figure 2.2 Rim-structure Computation. a) Cross section of an inner rim from which dust has been stripped. Photons are propagated through this rim to determine the 'optically thin' grid-cell temperatures. The color scheme shows integrated τ, measured along lines perpendicular to the disk mid-plane. b) Inner rim after the first dust growth step. Dust is grown in cells that are cooler than the sublimation temperature. The contours connect points with equal integrated tau. c) and d) depict stages further along in the dust growth scheme. The geometry of the rim is "sublimation converged" in (d) (see 2.2.2). A hydrostatic equilibrium calculation (see 2.2.1) is then performed. The dust growth and hydrostatic equilibrium calculations are repeated until convergence is reached for the structure. The rim shapes depicted above are not the final converged solution. See Figure 2.3 for the final rim shapes.

Figure 2.2 illustrates the dust-growth process in our computational scheme. The color scheme shows integrated optical depth, measured along lines perpendicular to the disk mid-plane. Panel-(a) is a grid for which the optical depth across each cell is 10^{-8}. Panel-(b) is a cross section of the grid after the first dust growth step where τ across each cell is now 10^{-3}. The cells have a τ of 10^{-1} across them in panel-(c).

The optical depth across each of the cells that lie away from the rim surface is 10 in panel-(d), whereas cells at the outer surface of the rim have been smoothed to resolve the $\tau = 1$ surface. The geometry of the rim can considered to be 'sublimation converged' in panel-(d). Any further addition of dust does not significantly change the distance of the $\tau = 1$ rim surface from the star. An appropriate amount of dust is put into each of the cells to reach a predetermined gas to dust ratio in the final dust growth steps. A hydrostatic equilibrium calculation as described in §2.2.1 is then performed. The dust growth and hydrostatic equilibrium calculations are repeated until convergence for the entire disk structure is reached (typically 4 iterations). In the next section we describe checks that ensure that this process gives accurate results.

2.3 Code testing against IN05 results

IN05 calculated inner rim models with astronomical silicate dust (Weingartner & Draine [2001]), where the shape of the rim is set by the fact that the evaporation temperature of dust depends on gas density (Pollack et al. [1994]). In this model, silicate grains sublimate at a higher temperature compared to other grains and hence fix the rim location. For silicate dust, the evaporation temperature $T_{\rm evp}$ can be parameterized as

$$T_{\rm evp} = G \left[\frac{\rho_{\rm gas}(r,z)}{1{\rm g\ cm^{-3}}} \right]^{\gamma} \tag{2.5}$$

where $G = 2000$K, $\gamma = 1.95\times10^{-2}$ and $\rho_{\rm gas}$ is the density of gas in $\rm g\,cm^{-3}$ (see IN05 eq. [16]). IN05 showed that this dependence of $T_{\rm evp}$ on gas density curves the inner rim.

Table 2.1. Basic properties of central star and the circumstellar disk.

Star		Circumstellar Disk	
Mass	2.5 $M_\odot$	Surface Density	$\Sigma(r) = 2000(r/\mathrm{AU})^{-1.5}$ g cm^{-2}
$T_{\rm eff}$	10,000 K	Disk outer-Radius	200 AU
Luminosity	47 $L_\odot$	Mass	3.8×10^{-2} $M_\odot$
Distance	150 pc		

In order to test the numerical scheme described in §2.2.2 we compared TORUS results for the rim with the IN05 results (kindly provided by A. Isella). Table 2.1 describes the properties of the star and the circumstellar disk used in the comparisons. Figure 2.3 shows the shape of the rim for large (1.2μm) and small (0.1μm) grains. The rim here is defined as the $\tau = 1$ surface (for $\lambda = 5500$Å), calculated along radial lines from the central star towards the disk. Figure 2.4 compares the fraction of stellar luminosity re-emitted by the rim in infrared wavelengths (integrated over 1.25–7μm) as computed by IN05 and TORUS.

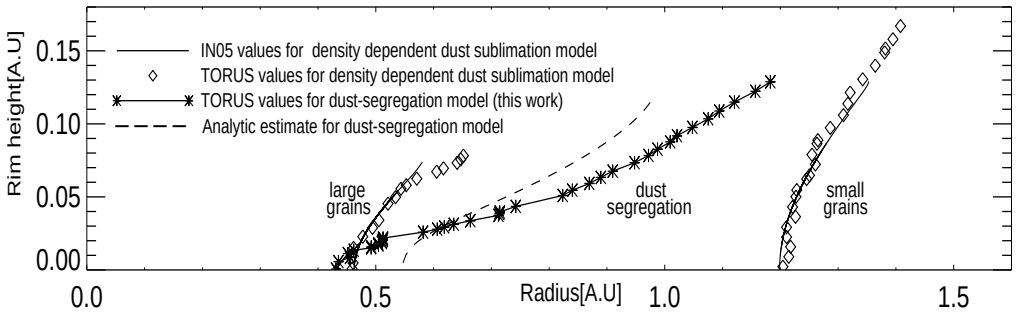

Figure 2.3 Converged Rim Structure. The 'rim' is defined as the $\tau = 1$ surface (for λ= 5500Å), computed along radial lines from the central star. The figure shows the height of the inner rim above the disk mid-plane. The IN05 rim has been scaled at the $\sim 8\%$ level to match up with the TORUS rim. The dashed lines are an analytical estimate of the evaporation front for the dust segregation model (see §2.4.2). The analytic rim agrees with the TORUS dust segregation rim at the 30% level. The match at the outer edge is poor because the analytic calculation does not take into account the transition between the rim and the 'shadow' beyond it.

Figures 2.3 and 2.4 show that that the TORUS results are consistent with the IN05 calculations at better than 15% level, giving us confidence in our Monte Carlo (MC) computations. We note that benchmark comparisons for MC codes, studying radiative transfer in optically thick disks (Pascucci et al. [2004]), show a similar level of agreement among the various MC codes.

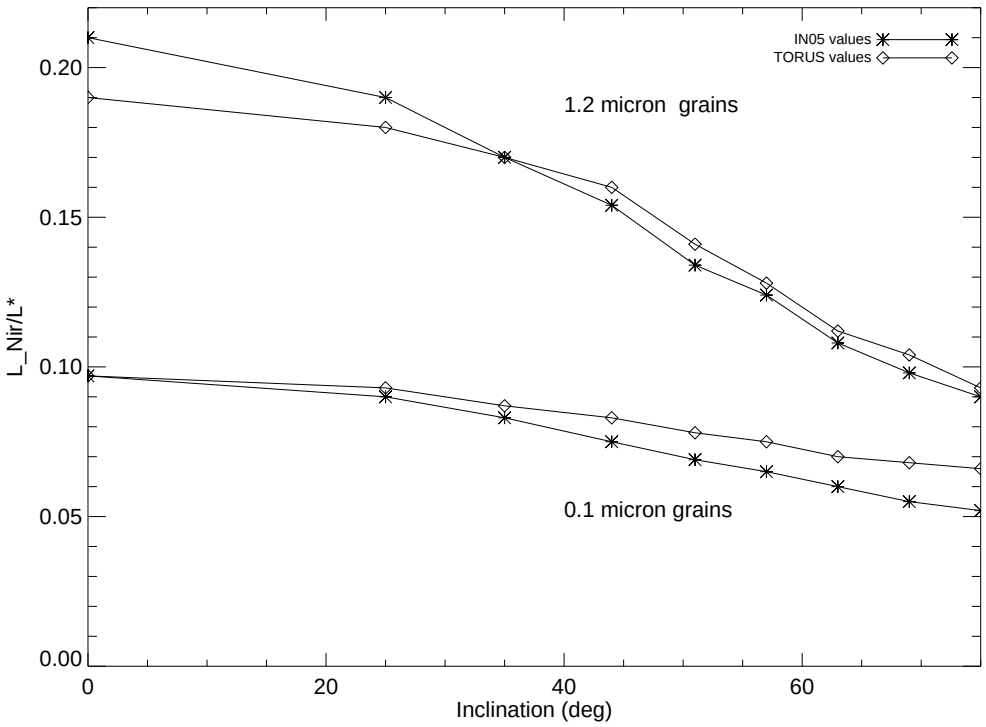

Figure 2.4 Integrated (between 1.25–7μm) NIR emission from the inner rim. The emission is plotted as a function of inclination angle for small and large grains. The emission has been normalized to the stellar luminosity.

2.4 Rim curvature due to grain growth/settling

2.4.1 Model Description

The rim in the IN05 model is curved because of a density-dependent dust-evaporation temperature. In this section we describe an alternative model in which the dust

sublimation temperature is kept fixed at 1400 K and rim curvature arises entirely because of dust growth and settling.

Small grains are much less efficient at cooling than large grains. If only single-sized grains are present, then at a given distance from the star, small grains will have a higher temperature than large grains. Under the assumption of a good temperature coupling between gas and dust (at densities characteristic of the rim region, this is a good approximation even in the disk photosphere - Kamp & Dullemond [2004]), a mixture of small and large grains will be hotter than the case where only large grains are present. Combined with dust sublimation, this means that the location and shape of the inner rim will change depending on the relative fraction of small and large grains.

Observational (e.g. Rettig et al. [2006]) and theoretical work (Weidenschilling & Cuzzi [1993]; Dullemond & Dominik [2004]; Tanaka et al. [2005]), and model fits to data (D'Alessio et al. [2001, 2006]; Chiang et al. [2001]) have shown that dust properties in circumstellar disks evolve with time. Small grains tend to coagulate into larger grains and settle towards the disk mid-plane, with the evolution of dust grain sizes occurring most rapidly in the disk mid-plane where the densities are high. In the absence of strong turbulence (the nature and strength of turbulence in circumstellar disks is not well understood), large grains will have a smaller scale-height than small grains. Thus grain growth and settling provide a natural means for changing the fraction of large and small grains as a function of height ('dust segregation') from the disk mid-plane. This will curve the rim as described in the previous paragraph.

As an illustration, we look at a model (henceforth 'dust segregation model') with silicate dust (Weingartner & Draine [2001]). In order to simulate dust settling we fix the large (1.2μm) grain scale height to be 60% of the gas scale height. We do not settle the small grains (0.1μm) and their scale height is fixed to be the same as the gas scale height. As grains grow, the net mass of small grains decreases, while the net mass of large grains increases: we fix the mass of large grains to be ~ 9 times the mass of small grains. All the the dust mass resides in the 1.2 & 0.1 μm grain components and total mass of dust in the disk is chosen to be 1/100th of the total gas mass. The rim gets curved over a wide range of parameter choices. The curvature can be made stronger by increasing the relative fraction of small grains.

The above description leads to the following expressions for dust density:

$$\rho_{1.2} = 1.5 \times 10^{-2} \rho_{o\_\mathrm{gas}} \exp\left[-\frac{1}{2}\frac{z^2}{(0.6h)^2}\right] \tag{2.6}$$

$$\rho_{0.1} = 10^{-3} \rho_{o\_\mathrm{gas}} \exp\left[-\frac{1}{2}\frac{z^2}{h^2}\right] \tag{2.7}$$

where $\rho_{1.2}$ is the density of 1.2μm grains, $\rho_{0.1}$ is the density of 0.1μm grains, ρ_{o_gas} is the gas density in the mid-plane, z is distance perpendicular to the disk mid-plane and h is the gas scale height. The star and disk parameters are chosen as in Table 2.1 (the parameters are the same as in the IN05 models of section 3).

2.4.2 Geometry of the Dust Segregation Rim

Rim Shape

Figure 2.3 shows the shape of the inner rim for the dust segregation model. The curvature of the rim depends on the relative density fractions of large and small

grains and the width depends on the sizes of the two dust components. A major finding here is that the dust segregation model can curve the rim on much larger scales than a density-dependent dust sublimation temperature (IN05) model. The $\tau = 1$ surface is nearly vertical at the inner edge of the dust segregation model because of the fixed, density-independent dust sublimation temperature.

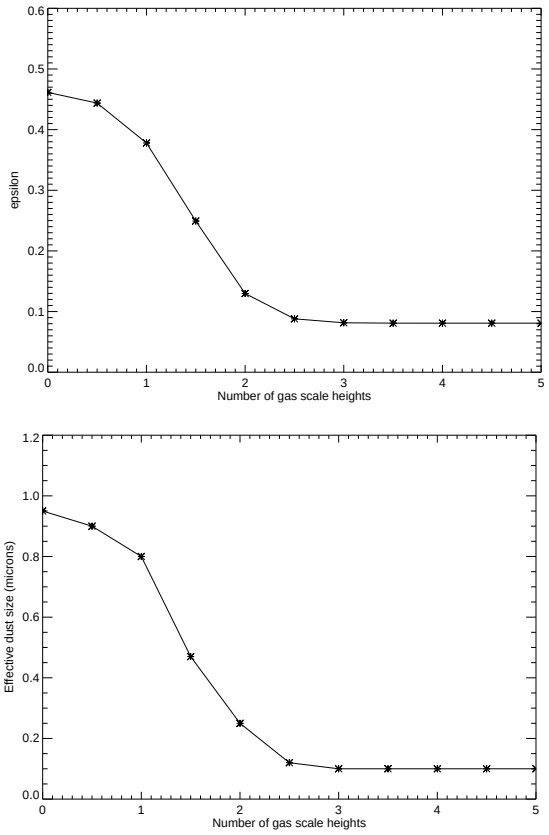

Figure 2.5 Dust Planck-mean Opacities. a) The ratio of Planck mean opacities for dust at the sublimation temperature and at the stellar photospheric temperature for the dust segregation model. b) Effective dust size plotted against the number of gas scale heights (see 2.4.1).

Analytic Estimate for Rim Shape

The most important dust parameter that determines the rim shape is $\epsilon(z)$, defined as the ratio of Planck mean opacities at the dust sublimation temperature and the stellar

effective temperature (IN05). Using equations (6) and (7) and values of Planck mean opacities for 0.1μm and 1.2μm grains, ϵ (see Appendix for a more general expression) for the dust segregation model is given by

$$\epsilon\left(z\right) = \left[\frac{0.42 + 0.015\exp\left(\frac{0.89z^2}{h^2}\right)}{0.76 + 0.181\exp\left(\frac{0.89z^2}{h^2}\right)}\right] \tag{2.8}$$

Figure 2.5a shows ϵ as a function of mid-plane height. Corresponding to this ϵ, an effective dust size which has the same ϵ as the dust mixture, is plotted in Figure 2.5b.

A crude estimate for the rim shape in the dust segregation model can be obtained analytically. The dust destruction radius $R_{\rm evp}$ (see Calvet et al. [1991]; Isella et al. [2006]) is

$$R_{\rm evp}\left[\rm AU\right] = 0.034\left[\rm AU\right]\left(\frac{1500K}{T_{\rm evp}}\right)^2\left[\left(\frac{L_*}{L_\odot}\right)\left(B + \frac{1}{\epsilon(z)}\right)\right]^{1/2}, \tag{2.9}$$

T_{evp} is the dust evaporation temperature, L_* is luminosity of the star in solar units, and B is a dimensionless diffuse heating term. B characterizes the optical thickness of the rim to its own thermal emission.

The gas scale height h at R_{evp} is estimated to be (see eqs. (7) and (8) from Chiang & Goldreich [1997])

$$h\left[\rm AU\right] = R_{\rm evp}\left[\rm AU\right]\left[\left(\frac{T_{\rm gas}}{4\times10^7K}\right)\left(\frac{M_\odot}{M_*}\right)\left(\frac{R_{\rm evp}}{4.64\times10^{-3}\ \rm AU}\right)\right]^{1/2} \tag{2.10}$$

where $T_{\rm gas}$ is the temperature of the bulk of the gas (assumed to be isothermal) and M_* is mass of the star in solar masses.

Combining equations (8), (9), and (10), substituting for stellar parameters from Table 2.1 and setting $T_{\rm evp} = 1400\,\rm K$, the height of the evaporation front (see appendix

for a general result) as a function of distance from the star along the disk mid-plane becomes

$$z\,[\mathrm{AU}] = 1.06 R_{\mathrm{evp}}\,[\mathrm{AU}] \left[\ln\left(\frac{5.87\mathrm{AU}^{-2}R_{\mathrm{evp}}^2 - 0.42B - 0.76}{0.181 + 0.015B - 0.21\mathrm{AU}^{-2}R_{\mathrm{evp}}^2}\right)\right]^{1/2} \times \left[\left(\frac{T_{\mathrm{gas}}}{1\times10^8 K}\right)\left(\frac{R_{\mathrm{evp}}}{4.64\times10^{-3}\ \mathrm{AU}}\right)\right]^{1/2} \quad (2.11)$$

Figure 2.3 shows an analytic estimate for the rim shape (we assume a gas temperature of 1000 K and have set $B = 2$, Calvet et al. [1991]). The analytic rim agrees with the TORUS dust segregation rim at the 30% level. The match at the inner edge of the rim can be improved by tuning the diffuse heating parameter B, but the match at the outer edge remains poor because the analytic estimate is not self-consistent and does not take into account the transition between the rim and the 'shadow' (see §2.4.3) region beyond it.

2.4.3 Observables

SED

Figure 2.6 shows the infrared emission from the inner rim and the outer flared-disk component. There is significant emission over the stellar blackbody (denoted by the continuous line) from 1.5μm onwards. The strength of the rim emission is approximately determined by the temperatures along the rim at optical depths of 2/3 (calculated at the wavelength of emission). Figure 3 in the IN05 paper shows that at a given optical depth, the small grain rim has a lower temperature than the large grain rim. Because of this temperature difference, near-IR emission in the small grain model gains strength at longer wavelengths compared to the large-grain and dust-segregation models.

Images and Visibilities

In order to illustrate the differences between the IN05 and dust segregation models we have computed synthetic images and visibilities for the different models. At 2.2μm, all the emission comes from the rim and the central star. The panels in Figure 2.7 show 2.2μm rim surface brightness for two inclination angles. As discussed previously, and is evident in Figure 2.7, the dust segregation rim is thicker than the IN05 rims. The dust segregation models also distinguish themselves observationally from the IN05 rims by their visibility curves. Figure 2.8 shows plots of 2.2μm visibilities calculated along the disk major and minor axes. The visibilities at long baselines are more oscillatory in the IN05 models. The IN05 rims are also more skewed at large inclination angles which would give them a stronger closure phase signal (Monnier et al. [2006]).

2.5 Discussion

In this chapter we introduced a new mechanism based on dust growth and settling to curve the inner rim. As a consequence of growth and settling, opacity in the rim mid-plane will be dominated by large grains whereas small grains dominate the opacity higher up in the disk photosphere (grain settling in the inner rim with large grains dominating the mid-plane opacity may be needed to explain near-IR SED and interferometry data on VVSer, Pontoppidan et al. [2007]). Large grains can exist much closer to the star than small grains since they cool more efficiently. A variation in grain size with disk scale height in the inner rim causes the rim to curve as shown in Figure 2.3. This curvature is on a much larger scale than the curvature produced

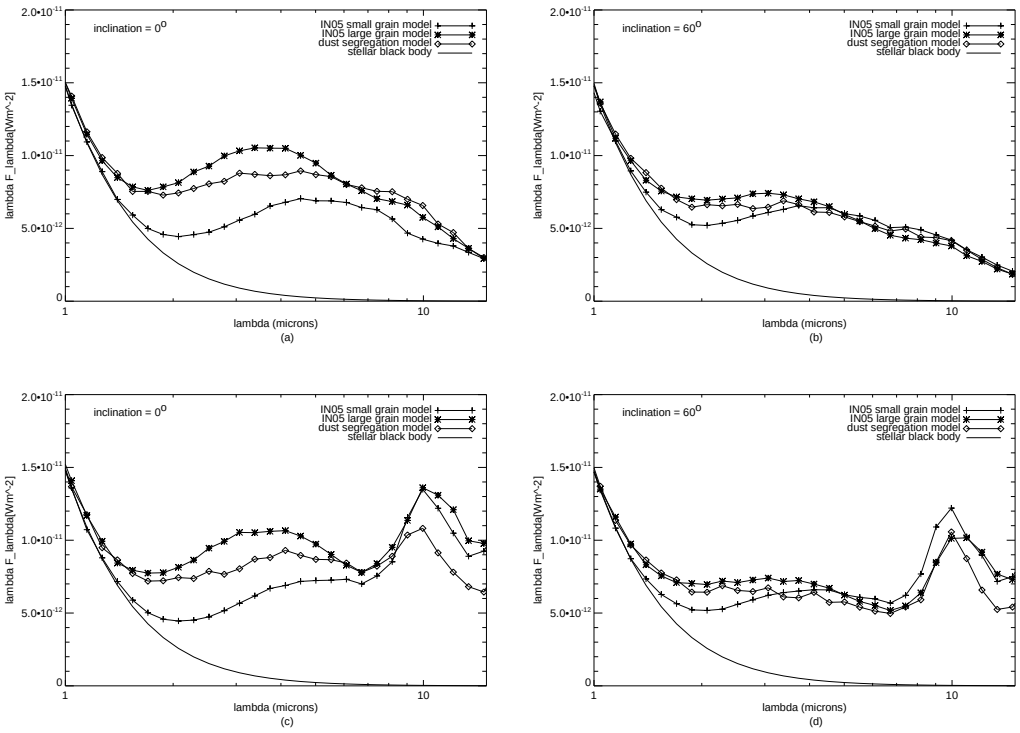

Figure 2.6 Rim infrared SED. a & b show near and mid-IR SEDs of the star + rim system for the IN05 and dust segregation models. c & d show SEDs of the star + rim + the disk. The star is placed at 150pc with stellar parameters described in Table 2.1. (a, c) system is face-on, (b, d) system is inclined 60^{o} from face-on.

in the IN05 models. Figure 2.8 shows that the two models can be distinguished based on their visibility curves.

In the dust segregation model that we studied in §2.4.1, the effects of dust growth and sedimentation on rim structure were calculated assuming that the dust sublimation temperature is independent of density. But in reality, both dust evolution and the density dependence of dust evaporation temperatures (INO5 model) probably simultaneously play a role in determining rim structure. We have shown that in the absence of strong turbulence the rim shape is predominantly determined by grain growth and settling. Adding a density dependence to dust sublimation temperatures will lower the rim height (see Fig 2.3) and extend it further into the disk by just a

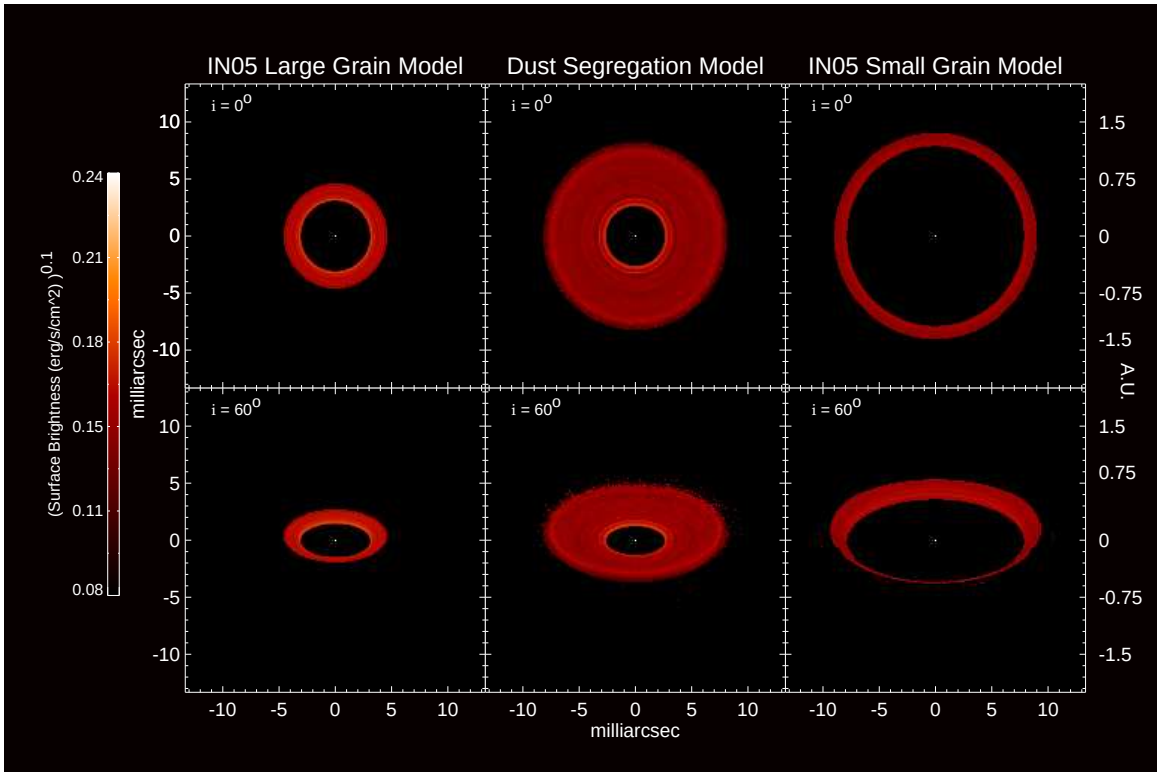

Figure 2.7 Synthetic 2.2μm images for the different rim models discussed. The panels on the left and right are IN05 rims computed for 1.2μm (large grain) and 0.1μm (small grain) silicate dust. The center panels are images for the dust segregation model. The star is placed at 150pc with the stellar parameters described in Table 2.1. The star is unresolved at the image scale and is just one bright pixel at the center of the images.

few tenths of an AU: a small perturbation compared to the effect of dust segregation on rim shape.

Calculations in this chapter do not take into account effects of gas on dust rim geometry. Gas can affect the structure and location of the rim through accretion heating and by providing a source of opacity to stellar photons within the dust destruction radius. Akeson et al. [2005b] have shown that gas accretion heating might contribute significantly to the near-IR excess observed in some T Tauri stars and play an important role in fixing the location of the dust destruction radius in these systems. Eisner et al. [2006] argue that emission from gas within the inner rim is

needed to explain spectrally dispersed near-IR interferometry data on Herbig Ae/Be systems. The effects of gas on dust rim structure and observed near-IR excesses in YSOs is not well understood. Some theoretical efforts (see for e.g. Muzerolle et al. [2004]) have been made in this direction, but further progress would require detailed modeling of the relevant gas physics.

The dust rim in YSOs is a unique test-bed for theories of grain evolution. A number of observational and modeling results (D'Alessio et al. [2001, 2006]; Chiang et al. [2001]; Rettig et al. [2006]) have found evidence for dust growth and settling in the outer regions (tens of AU scale) of YSO disks. In this work we show that long baseline NIR interferometry provides an opportunity for similar studies on the inner rim at sub-AU scale. Furthermore, if the gas within the inner rim were to emit significantly in the near-IR (gas emission is not well constrained and results from CHARA on AB Aur suggest that this is important), then the baselines of CHARA($\sim$ 300m) are capable of partially resolving the hot gas emission, at-least for a few Herbig systems. Combined with accretion line diagnostics (Muzerolle et al. [2004]), near-IR interferometry could help pin down the structure of the inner gas disk. In Chapter 3, we will compare SED and interferometry data with our model predictions for the inner rim.

2.6 Chapter Summary and Conclusions

We have described a Monte Carlo approach to calculating the structure of the inner rim in protoplanetary disks. The obvious advantage of this method over an analytic approach is that it allows for a self-consistent determination of the entire disk

structure. Any effects of spatially varying dust properties on disk structure (and the resulting effects on SEDs and visibilities) can also be easily studied.

We have shown that dust growth and sedimentation may play a dominant role in determining the structure of the inner rim. The difference in cooling properties between grains of different sizes, combined with sublimation and a vertical gradient in dust sizes in the disk, leads to inner rims that are extremely curved (over scales > 0.7 AU in cylindrical radius for an A0 star, see Figure 2.3). Synthetic images (Figures 2.7 & 4.1) and visibilities (Figures 2.8 & 4.2) for the rim models have been computed, highlighting differences between various theoretical models.

The inner rim dominates near-IR emission from circumstellar disks. Studies in the near-IR thus isolate the rim from the rest of the disk and are therefore a powerful tool for characterizing rim properties. In the last decade or so, near-IR interferometers (Millan-Gabet et al. [1999, 2001]; Eisner et al. [2003, 2004]; Akeson et al. [2005b,a]) have been used to determine the sizes of inner rims in a number of Herbig Ae/Be and T Tauri stars. This has helped in establishing a tight correlation between the radii of the rims and the luminosities of the central stars (Monnier & Millan-Gabet [2002]; Monnier et al. [2005]). The current generation of near-IR interferometers (CHARA, VLTI) are capable of taking the next natural step—determining the geometry of the inner rims. As shown in this chapter and IN05, the geometry of the inner rim is tied to multiple dust properties such as grain evolution, grain sedimentation (which depends on the strength of turbulence), and dust sublimation temperatures (IN05). Once the inner rim shape is constrained, mid-IR interferometry (as seen in Figure 4.1, both the rim and the flared disk region emit in the mid IR) can be used to assess

the geometry of the outer, flared-disk component.

To test the validity of inner-rim models and constrain dust properties in YSO evaporation fronts, we compare theoretical models with sub-milli-arcsecond resolution NIR interferometry observations in Chapter 3.

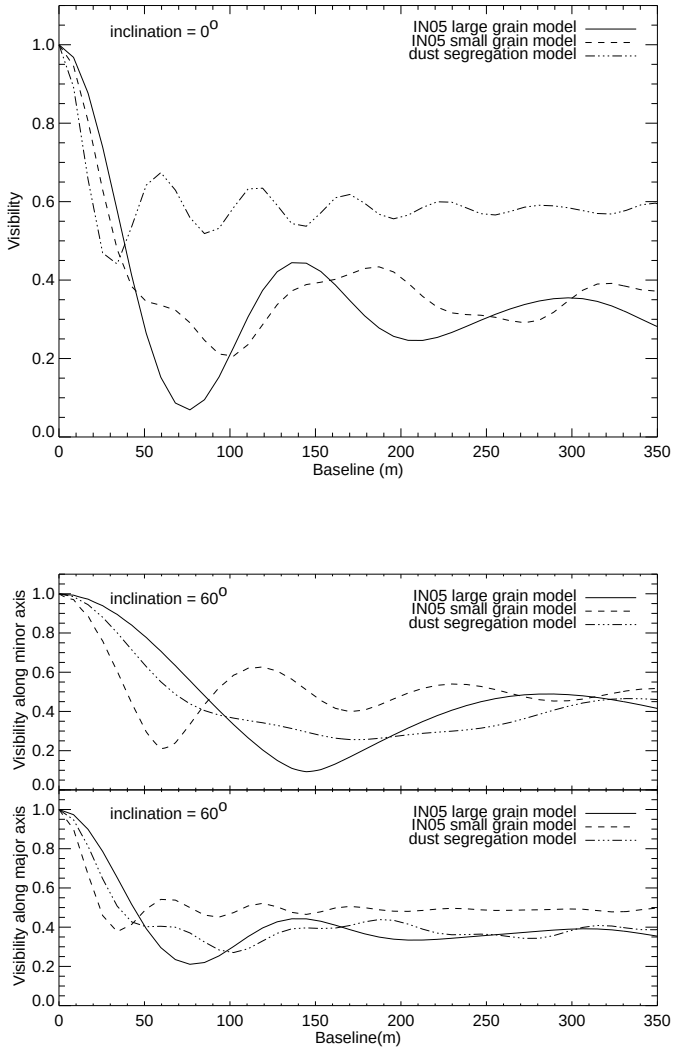

Figure 2.8 2.2μm visibilities for the IN05 and dust segregation models. The panel on top shows the visibilities for a face-on disk and the bottom panel shows visibilities computed along the major and minor axis for an inclined disk.

Chapter 3

Confronting Long-Baseline Near-Infrared Interferometry

Abstract: Using the longest optical-interferometeric baselines currently available, we have detected strong near-infrared (NIR) emission from inside the dust-destruction radius of Herbig Ae stars MWC275 and AB Aur. Our sub-milli-arcsecond resolution observations unambiguously place the emission between the dust-destruction radius and the magnetospheric co-rotation radius. We argue that this new component corresponds to hot gas inside the dust-sublimation radius, confirming recent claims based on spectrally-resolved interferometry and dust evaporation front modeling.

3.1 Introduction

In the previous chapter, we presented state-of-the-art models for the dust evaporation front in circumstellar disks. The models show that the front structure is extremely sensitive to dust properties. The sublimation front can thus be used to study dust physics operating in the inner regions of circumstellar disks, provided that we have a means to spatially resolve the geometry of this region. Spatially resolved studies are also crucial to validating current models.

To be able to completely resolve the inner-rims of even the nearest Herbig Ae systems (distances of $\sim$ 150pc), one needs milli-arcsecond resolution. The only two

instruments currently capable of this resolution in the NIR wavelengths (where the sublimation front produces bulk of its emission) are the CHARA interferometer array on Mt. Wilson (California,USA) and the VLTI interferometer in Paranal (Chile). To test rim models and constrain dust physics in the gas-dust transition region, we began a YSO observing program with the CHARA array (Prof. Monnier's optical interferometer group is member of the CHARA collaboration). In the next few sections, I describe the CHARA interferometer, our observations on two Herbig Ae stars MWC275 and AB Aur, the data reduction procedure and model comparisons with the data.

3.2 The CHARA Array

The CHARA array was constructed and is currently operated by Georgia State University's Center for High Angular Resolution Astronomy (CHARA). The Array works in the optical and NIR and is located on the on the grounds of the historic Mt. Wilson Observatory. A complete description of the instrument is provided in ten Brummelaar et al. [2005].

The array consists of six 1-meter telescopes arranged in a Y configuration (Fig 3.1). This arrangement provides $C_2^6 = 15$ non-redundant baselines between 34m and 331m. Fig 3.2 (ten Brummelaar et al. [2005]) shows the on-sky Fourier coverage provided by the telescope pairs. Light from each of the telescopes is transported through dedicated vacuum tubes to a central beam synthesis facility (BSF). The vacuum tubes help maintain the quality of the star-light wavefront, preventing further degradation of beam quality due to atmospheric turbulence.

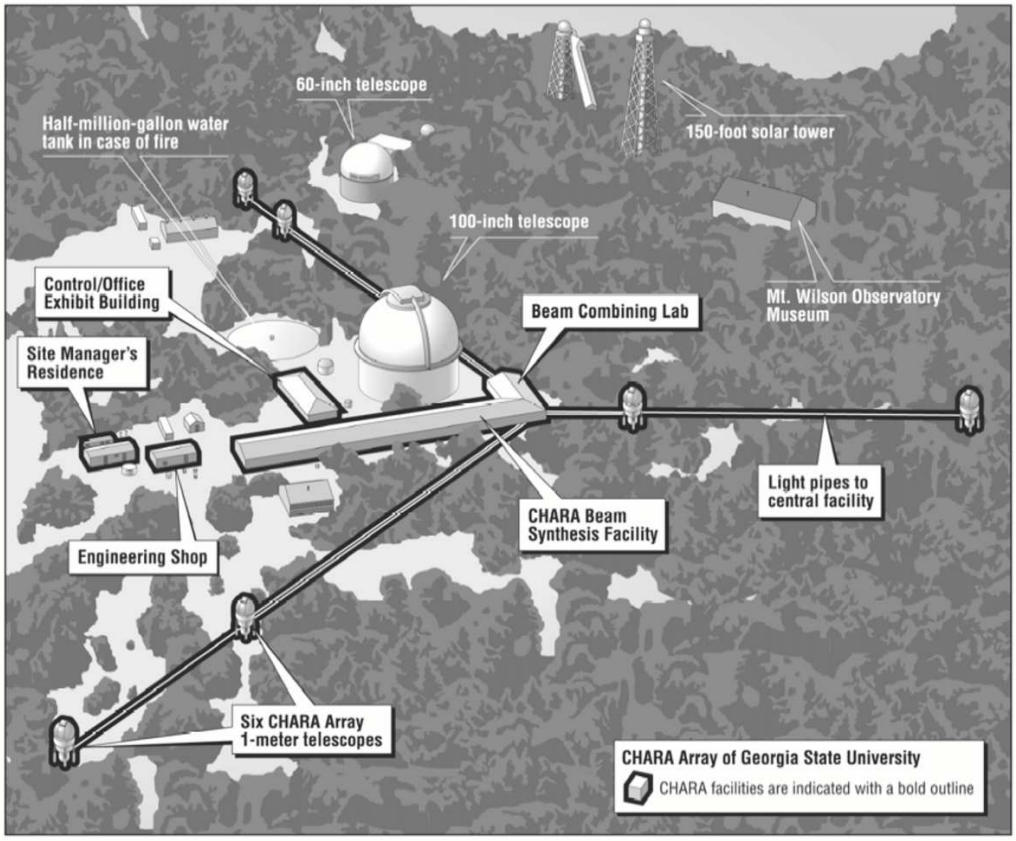

Figure 3.1 The CHARA Array layout. North is towards lower right.
(Diagram by GSU Office of University relations)

The BSF is an L shaped building housing the Optical Path Length Equalization Facility (OPLE) and the Beam Combination Laboratory (BCL). Zero optical path length difference between the telescope beams is achieved in 2 stages at CHARA. The first stage occurs while the star light is still in vacuum with fixed delay lines referred to as the "Pipes of Pan" (PoPs). The Pops introduce a fixed amount of delay into the beams with mirrors placed at intervals of 0, 36.6, 73.2, 109.7, and 143.1m that reflect the light into the second continuous stage of the delay system. Stage 2 of the delay is provided with OPLE carts riding on precision-aligned cylindrical steel rails, that help track the diurnal motion of the star as it moves across the sky. A servo

system with a laser metrology unit, helps provide 92m of path length compensation with typical rms errors of 10nm.

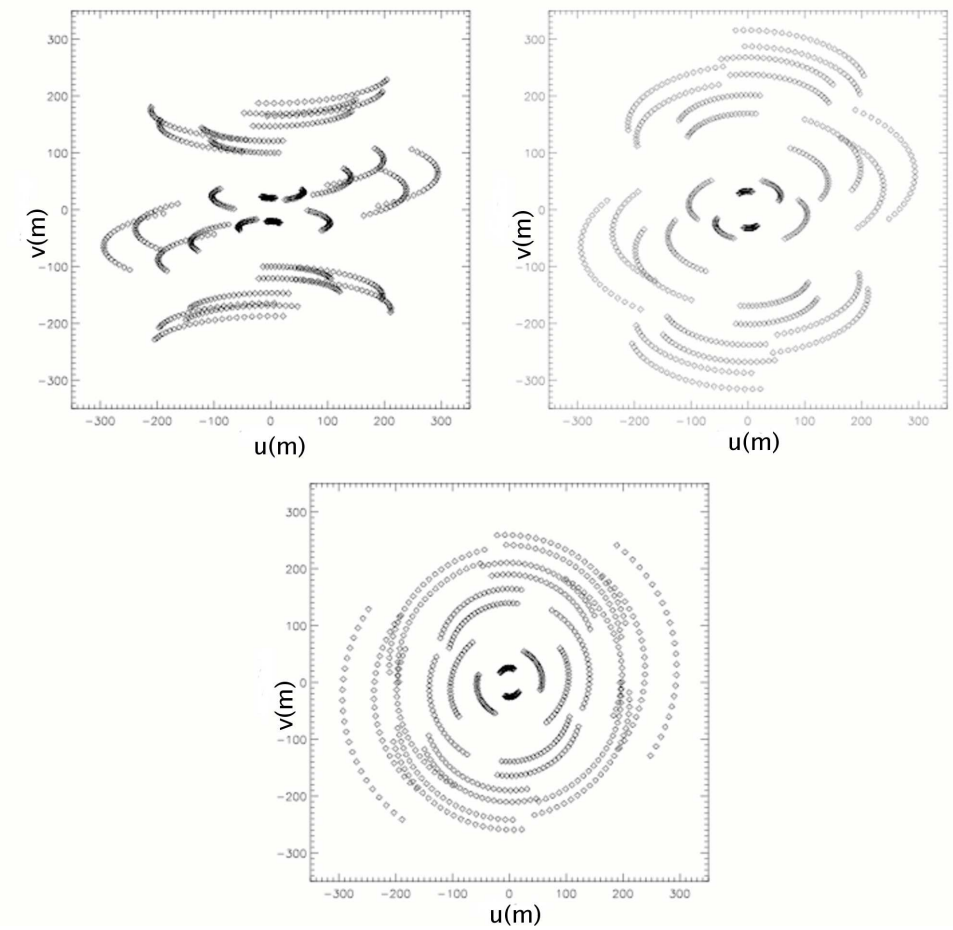

Figure 3.2 uv coverage of the CHARA Array for 3 declinations. -15^o (top left), +30^o (top right) and +75^o (bottom). The plots show the coverage resulting from all six telescopes within 3hrs from transit (Diagram from ten Brummelaar et al. [2005])

All observations for this thesis were performed in the K-band with the "CHARA Classic" combiner. CHARA Classic is a 2-telescope pupil-plane combiner. The interfering beams are imaged on two spots in a beam combining camera after passing through a beam splitter. Fringes are detected in scanning mode (Fig 3.3) provided by a dither mirror mounted on a piezoelectric translation stage.

CHARA provides a resolution of slightly better than 1 milli-arcsecond at K band,

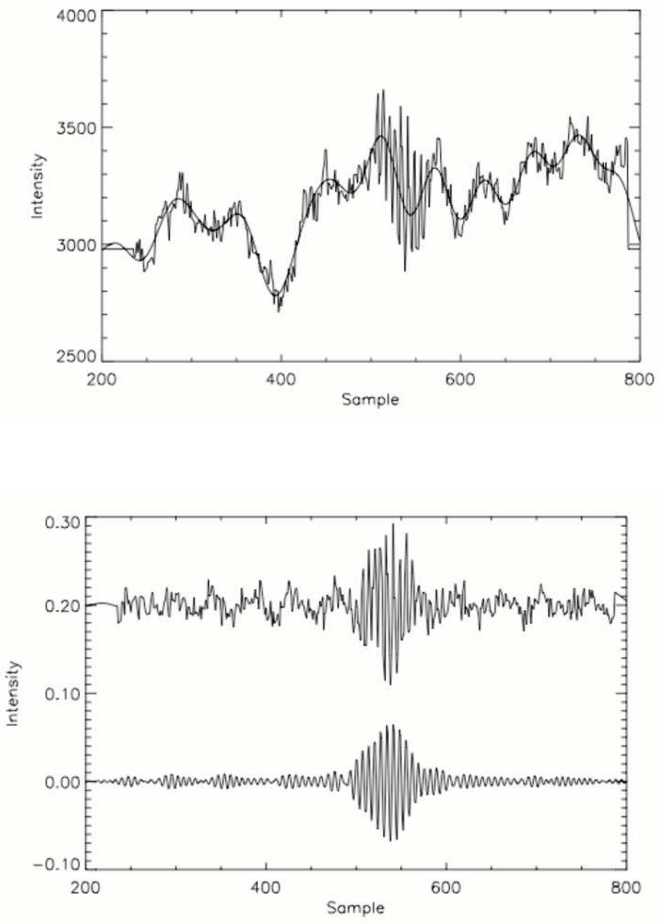

Figure 3.3 CHARA Fringes. The raw signal from the fringe scan (top) with a low-pass filtered version superimposed on it. The bottom panel shows the same scan, with an offset of 0.2, after normalization, and finally after implementation of the band pass filter (Diagram from ten Brummelaar et al. [2005])

where resolution is defined as $\frac{\lambda}{2B}$ (λ is wavelength of observation and B is the interferometer baseline length). The limiting magnitudes for CHARA Classic are K$\leq$ 6.5, H$\leq$7 and V$\leq$ 9. The V band limit is set by the tip/tilt system, which helps lock the star light onto specified pixels of the beam combining camera. Besides the K band, CHARA also operates at H band (1.67μm) and at optical wavelengths.

3.3 Observations

3.3.1 The Interferometric Observable: Visibility

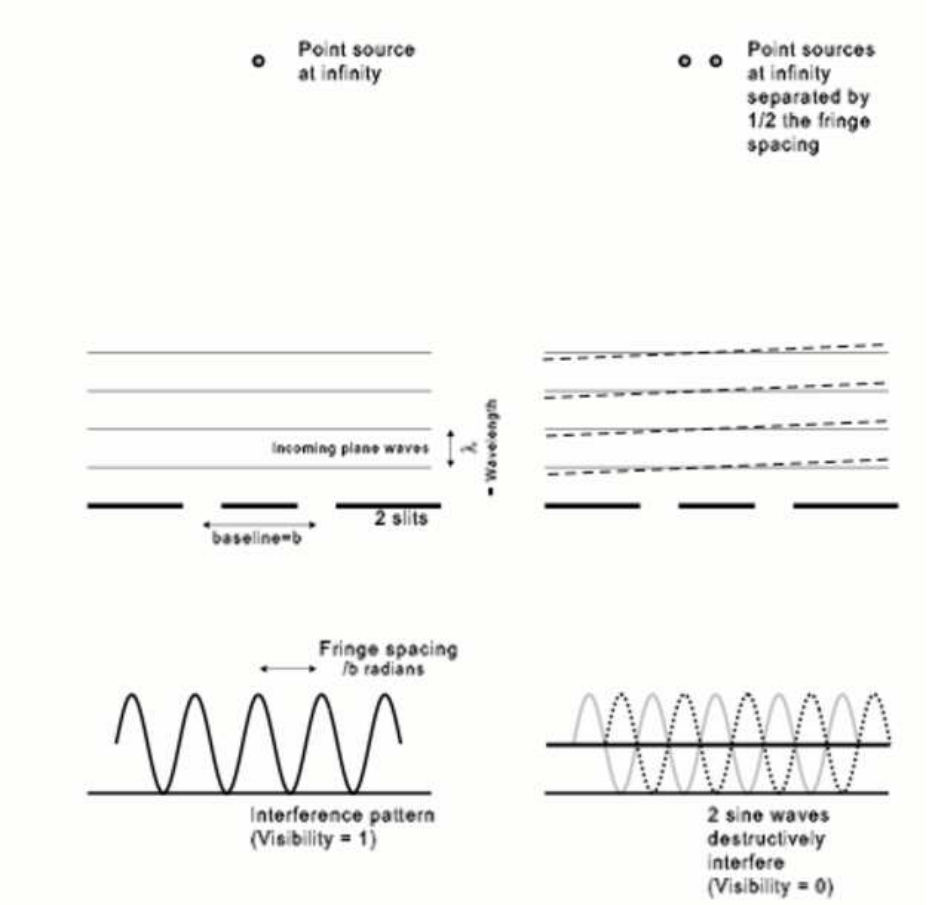

Figure 3.4 Interferometry as a form of Young's Double Slit Experiment. The left panel is for a single point source and the right panel is for two point sources separated at half the fringe spacing. (Diagram from Dr. J. D. Monnier's PhD thesis)

2-telescope interferometry is essentially the Young's Double Slit experiment performed on the sky. Figure 3.4 shows a schematic of such a setup. Light from a distant source (like a star) arrives at the telescopes (represented by slits). The electric field at each of the telescope is then propagated to a beam combiner camera (represented by the screen behind the slits) where the light constructively or destructively interferes

(light has a wave nature), because of relative path differences between the telescopes (slits). The angular spacing of the fringe maxima is given by -

$$\theta = \frac{\lambda}{B} \tag{3.1}$$

where B is projected separation between the telescopes (slits). The presence of another star (incoherent with the first and of equal brightness) at an angular separation of $\frac{\lambda}{2B}$, will produce a fringe pattern out of phase from the first star (see right panel in Fig. 3.4). The two interference patterns cancel each other out and uniformly illuminate the detector (screen). The fringing in the illumination pattern is quantified by the *visibility*

$$V = \frac{I_{max} - I_{min}}{I_{max} + I_{min}} = \frac{\text{Fringe Amplitude}}{\text{Average Intensity}} \tag{3.2}$$

I_{max} and I_{min} denote the maximum and minimum intensity of the fringes. Hence, the fringe patterns in the left and right panels of Figure 3.4 have visibilities of 1 and 0 respectively. The visibility is a very important measurable as it is relates to the Fourier Transform of the illumination-source surface-brightness distribution via the van Cittert-Zernike theorem -

$$\tilde{V}(\vec{B}) = \frac{\int I(\vec{s}) e^{-i\vec{B}.\vec{s}} d\vec{s}}{\int I(\vec{s}) d\vec{s}}, \tag{3.3}$$

where $\vec{B}$ is the baseline vector, $\vec{s}$ is the sky coordinate and $I(\vec{s})$ is the intensity distribution of the source. In 2-telescope beam combination, the phase component of $\tilde{V}$ is lost to atmospheric turbulence and the only good measurable is the magnitude of $\tilde{V}$, i.e.V (eqn 3.2). As an illustration, Fig 3.5 shows the K-band visibility-amplitude curves as a function of projected baseline length for a Gaussian and a Uniform Disk

(constant surface brightness profile). At short baselines the sources look like points and the visibility is high. As the baseline increases and the sources begin to get resolved, the visibilities drop. At long baselines the Uniform Disk visibility shows ringing because of the presence of a sharp outer edge.

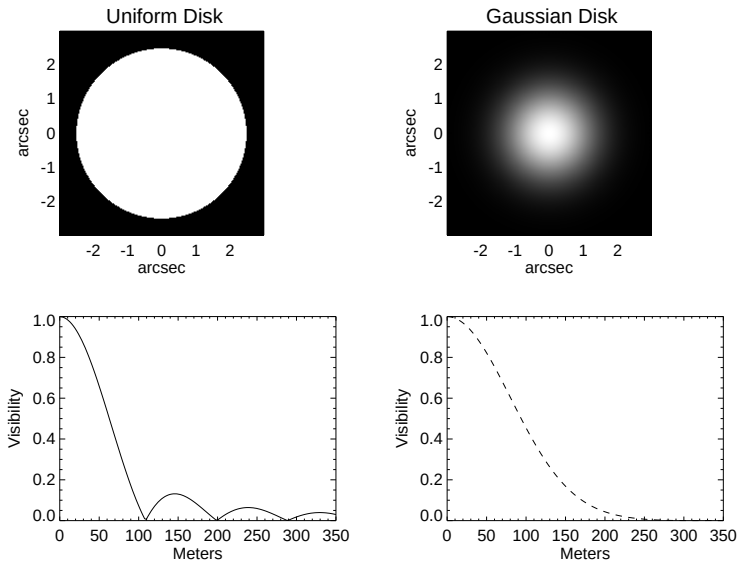

Figure 3.5 Illustrative visibility curves. a) The left panels show the image and corresponding Visibility curve for a Uniform Disk of diameter 5 mas. b) The right panels show the same for a Gaussian Disk with Full Width Half Maximum of 2.5 mas.

A measurement of fringe visibilities can thus be used to constrain surface brightness properties of light sources in the sky and differentiate between various physical models. Interferometers have been successful in measuring stellar diameters (Michelson & Pease [1921]), determining binary orbits, probing the circumstellar environments of young as well as evolved stars (McCarthy & Low [1975]; Millan-Gabet et al. [1999]), and imaging of stars outside the solar system (Monnieret al. [2007]).

3.3.2 CHARA observations of MWC275 and AB Aur

As discussed in Chapter 2, current models assume that the entire NIR excess observed in Herbig Ae stars arises solely from dust rims. However, recent observational results have begun to indicate that these models are inadequate in explaining some of the observed YSO properties. Akeson et al. [2005b] noted that NIR emission from the the dust rim alone was not sufficient to explain the spectral energy distribution (SED) of some T Tauri stars. Isella et al. [2006] pointed out that the dust evaporation temperatures of well studied astronomical dust types (Pollack et al. [1994]) were too low (producing dust rims with large inner radii) to explain the anomalously small NIR size of AB Aur. Eisner [2007] had to invoke gas emission to account for the apparent decrease in NIR sizes of Herbig Ae/Be stars with decreasing wavelength. Most recently, Kraus et al. [2008a] showed that the NIR visibilities of Herbig Be star MWC147 could not be explained without including emission from inside the dust evaporation radius. Due to the lack of sufficient spatial resolution, some of these conclusions are tentative and based on indirect arguments with multiple interpretations.

To unambiguously constrain the NIR disk structure in YSOs, we began an observation campaign with the CHARA Array using the CHARA Classic beam combiner. Our targets were MWC275 (V=6.86, K=4.59) and AB Aur (V=7.01, K=4.37). The targets (properties listed in Table 3.1) were observed at K band (central wavelength of 2.13 microns) with the long baselines of CHARA at a variety of orientations in 8 runs between June 2004 and June 2007 (see Tables 3.2 and 3.3 for detailed observing

Table 3.1. Basic properties of stars.

Name	Spectral Type	T_{eff} (K)	L_* $L_\odot$	D pcp	M_* $M_\odot$
MWC275 (HD163296)	A1e	9500	36	122	2.3
AB Aur (HD31293)	A0pe	9772	47	144	2.4

logs). The longest baseline observation for MWC275 was 325m (resolution [1] of 0.67 milli-arcseconds) and 320m (resolution of 0.68 milli-arcseconds) for AB Aur.

Even though our targets are 2 magnitudes brighter than the sensitivity limit of CHARA, we realized early on that the low expected visibilities (see Fig 3.6) at baselines $>$ 100m (based on fits to short baseline data) would make our experiment challenging. In order to maximize the chances of observing fringes, we adopted the following strategy -

1. Most of the science observations were done at a dither rate of 250Hz. For a star with K magnitude of 4.5 (with calibrated visibility < 0.3), the 250Hz dither rate seems to optimize the trade off between maximizing photon counts and maintaining photon phase.

2. To locate weak fringes on targets, we first obtained fringes on nearby calibrator stars (within 15^o from the target) and noted the OPLE offset at which the fringes were located. We then moved to the target and scanned a 2cm region around the calibrator offset for fringes. The OPLE carts were re-positioned in small steps and at each cart location we waited for several dithers to be completed before moving the cart again.

[1]Resolution is defined as $\frac{\lambda}{2B}$ -lambda is wavelength of observation and B is the interferometer baseline length.

Table 3.2. CHARA uv coverage and visibility data for MWC275.

UT-Date of Observation	u(m)	v(m)	Telescope pair	Calibrated Visibility	Calibrator Names
2004July09	-210.61	138.79	S1W1	0.150±0.008	HD164031
	-200.38	127.78		0.143±0.009	
2005July22	106.91	-11.88	W1W2	0.218±0.011	HD164031
	103.22	-18.38		0.227±0.009	
2005July26	102.45	5.03	W1W2	0.260±0.014	HD164031
	106.45	-1.61		0.241±0.011	
	107.18	-10.26		0.201±0.011	
	105.94	-13.95		0.232±0.011	
2006June22	-11.99	84.94	S2W2	0.345±0.016	HD164031
	-24.60	85.73		0.301±0.017	
	-42.30	87.77		0.203±0.013	
2006June23	-301.23	-85.20	E1W1	0.0715±0.0043	HD164031
	-302.93	-78.34		0.0730±0.0044	
2006June23	-84.05	98.77	S2W2	0.0925±0.0041	HD164031
2006Aug23	60.15	125.48	E2S2	0.181±0.010	HD164031,
	28.16	121.90		0.189±0.011	HD166295
2007June17	-94.21	66.98	S2W1	0.232±0.013	HD164031,
	-166.86	90.88		0.080±0.005	HD156365
	-184.56	102.73		0.096±0.006	
	-195.84	114.04		0.110±0.007	

Table 3.3. CHARA uv coverage and visibility data for AB Aur.

UT-Date of Observation	u(m)	v(m)	Telescope pair	Calibrated Visibility	Calibrator Names
2006Aug23	212.04	237.05	E1S1	0.095±0.005	HD29645, HD31233
	203.79	251.87		0.120±0.006	
	197.53	259.95		0.123±0.007	
2006Dec14	-5.77	-325.14	E1S1	0.115±0.007	HD29645, HD31233
2006Dec15	-93.57	8.26	E2W2	0.188±0.011	HD29645, HD31233

3. The OPLE carts try to equalize path lengths for star light based on an astrometric model. The models however are not perfect and cart positions for zero OPD (optical path difference) tend to drift relative to the model. To keep track of the OPLE offsets, we moved to a calibrator again after a 2cm scan on the target.

Steps 2 and 3 were repeated to identify and collect data on our target fringes.

Figure 3.6 shows a number of low visibility data points obtained with the manual 'fringe search' procedure.These would have been skipped over by an automated scan looking for high S/N fringes.

3.4 Data Reduction and Analysis

Figure 3.7 show a typical CHARA data scan. The fringe data were reduced based on power spectrum analysis detailed in ten Brummelaar et al. [2005]. Briefly, the total power in the fringe is related to the visibility by the following functional form -

$$Power = T^2 \frac{V^2 V_{sys}^2}{\Delta\sigma v_g} \tag{3.4}$$

where T is the intensity transmission function, $\Delta\sigma$ is the band pass, v_g is the fringe group velocity due to dither motion, V is source visibility and V_{sys} is the instrument visibility. The source visibility can thus be estimated from measurements of total fringe power. The top panel in Fig 3.8 shows the total raw power in the data. This includes noise from the detector, scintillation and photon noise in the signal. The noise is power is estimated using the shutter data (see Fig 3.7) in the scan which includes counts from each telescope separately as well the background counts from the detector. The bottom panel in Fig 3.8 shows the fringe power in the astronomical target after subtraction of noise from the raw power spectrum. The instrument

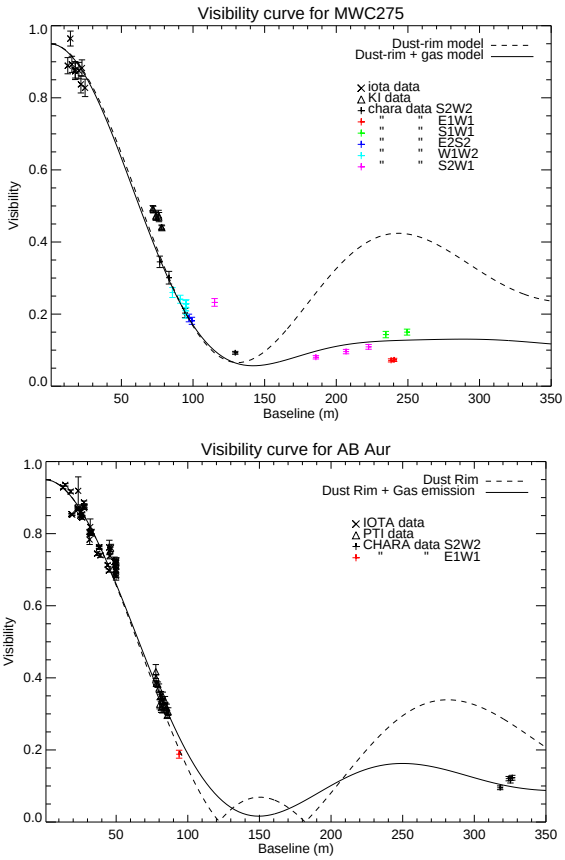

Figure 3.6 Visibility data and models for MWC275 (top) and AB Aur (bottom). MWC275 visibilities are plotted as a function of "effective baseline" (see §3.4), which accounts for the change in resolution due to disk inclination and PA.
The dotted lines correspond to "Standard" rim models tuned to fit visibility data for each source for baselines shorter than 100m. The solid lines correspond to dust rim+gas models. The model parameters are listed in Table 3.4.

visibility V_{sys} can be calibrated out from equation 3.4 to get the source visibility V by comparing the fringe power of the target with the fringe power in a calibrator having a known intrinsic visibility.

The data were reduced using standard CHARA reduction software (ten Brummelaar et al. [2005]) and these results were cross checked with an independent code developed at University of Michigan by Prof. John Monnier. Fig 3.9 shows the difference in squared visibilities for the calibrators and science targets computed with the

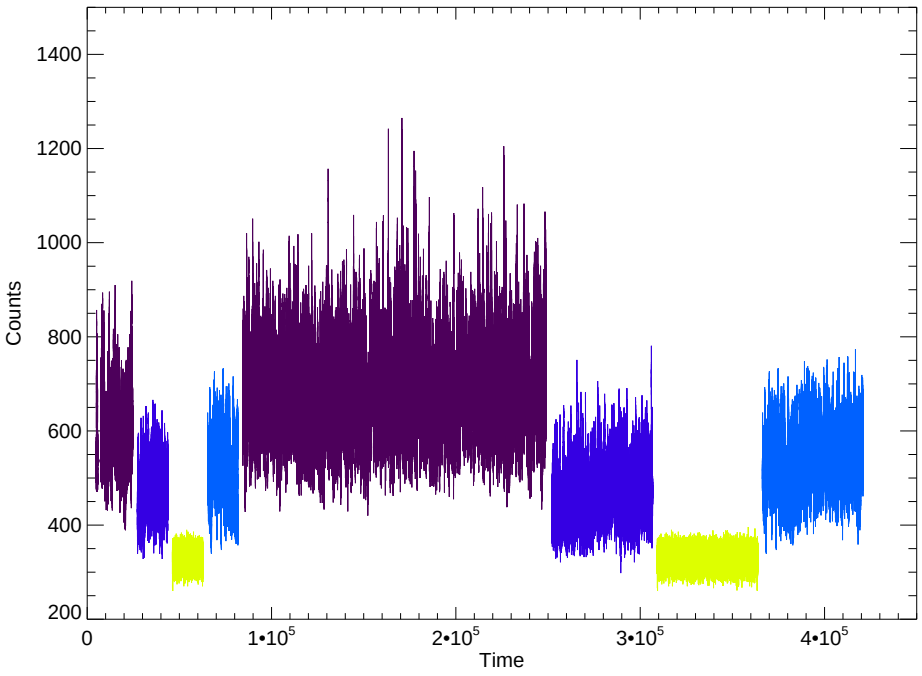

Figure 3.7 Sample CHARA data scan from one side of the beam splitter. The x-axis shows time and the y-axis represents signal strength. The lines in purple show the superposed signal from both telescopes, the dark blue lines are the signal from telescope 1 and light blue lines are signal from telescope 2. The background flux is presented in yellow.

2 codes. V^2 for the calibrators agree at the 2% level and V^2 for the objects (having a factor of 4 lower intrinsic visibility than the calibrators at CHARA baselines) agree to within 5%. These results give us high confidence in the robustness of our data analysis tools.

HD164031 , HD166295 (Merand et al. [2005]) and HD156365 with uniform-disk (UD) diameters of 0.83± 0.08 mas, 1.274±0.018 mas and 0.44±0.06 mas were used as calibrators for MWC275. AB Aur visibilities were calibrated with HD29645 (UD diameter=0.54±0.07 mas) and HD31233 (UD diameter=0.76±0.13 mas). During the data reduction procedure the flux ratios between the two interferometer telescopes were carefully monitored for the source and the calibrators (Fig 3.10). Data

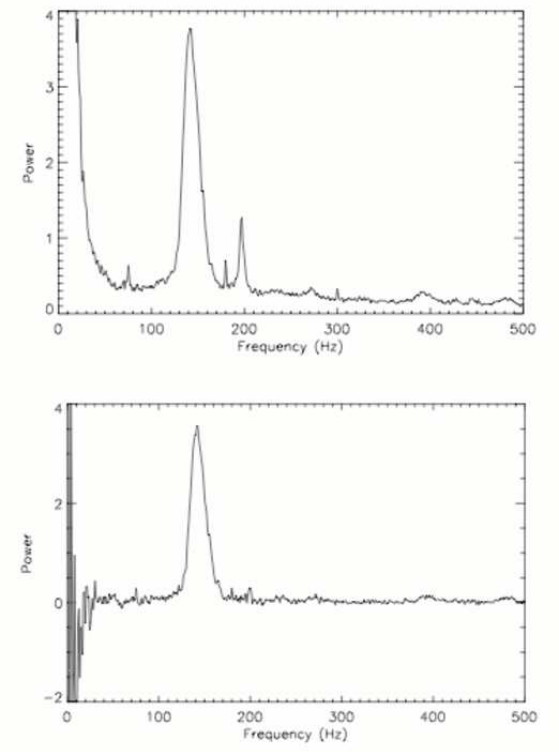

Figure 3.8 Sample power spectra. The top panel shows the raw spectrum with the fringe signal, photon noise, scintillation noise and camera noise. The bottom panel shows fringe with some of the noise sources measured and removed. (Diagram from ten Brummelaar et al. [2005])

points having a sudden flux ratio variation of greater than 10% from the mean were eliminated, as these seemed to coincide with large and uncertain calibration errors. Based on this criterion, we eliminated 3 data points on MWC275. The procedure was adopted to minimize calibration errors caused by differences in beam overlap in the source and calibrator. The final visibility errors (which include calibration errors, statistics and errors due to finite calibrator size) are at the $\sim$6% level (Tables 3.2 and 3.3) , typical for CHARA Classic. The new fringe-visibility data from CHARA were combined with past measurements from IOTA (Monnier et al. [2006]), PTI (Eisner et al. [2004]) and the Keck Interferometer (Monnier et al. [2005]) providing a baseline

coverage from 15m-320m on the targets, placing strong constraints on the geometry of the inner-most disk regions.

The baseline orientations used have allowed us to clearly detect the asymmetry of the MWC275 disk (details in Appendix C), as having inclination=$48^o \pm 2^o$, PA=$136^o \pm 2^o$, consistent with the inclination of 51^{+11}_{-9} degrees, and PA of $139^o \pm 15^o$ determined in Wassell et al. [2006]. Thus, in Fig 3.6 the visibility of MWC275 is shown as a function of "effective baseline" -

$$B_{eff} = B_{projected}\sqrt{cos^2(\theta) + cos^2(\phi)sin^2(\theta)}$$

where θ is the angle between the uv vector for the observation and the major axis of the disk and ϕ is the inclination of the disk. Under the flat disk assumption, the effective baseline correctly accounts for the change in resolution due to the disk inclination and PA (geometry of finitely thick disks is represented only approximately with optical depth effects and 3-D geometry of thick disks not being taken into account), allowing us to plot the visibility measurements as a function of one coordinate, simplifying presentation and analysis. As the AB Aur disk is near face on (Eisner et al. [2004]), we have plotted its visibility as a function of true projected baseline (Fig 3.6).

3.5 Modeling

To elucidate the structure of the inner disk and the dust rim, we constructed dust-only rim models for MWC275 and AB Aur and fit the models to the visibility data. In these models, all of the K-band emission is assumed to come from the inner dust rim

and the central star ("standard" model). The rim is in hydrostatic equilibrium and its shape is set by the pressure dependence of the dust grain evaporation temperatures (Isella & Natta [2005]; Tannirkulam et al. [2007]). The normalization of the pressure dependence of the evaporation temperatures (discussed in more detail in Chapter 5) is adjusted so that the model rims fit the short baseline (< 100m) visibility data. As can be seen in Fig 5.4, a realistic treatment of dust physics produces a curved inner rim with a sharp inner edge, set by dust destruction, and a sharp outer edge, set by the fact that the rim shadows (Dullemond et al. [2001]) a portion of the disk behind it preventing direct star-light from reaching the region.

We are able to fit the standard model to the visibility data for MWC275 and AB Aur at baselines shorter than 100m (Fig 3.6) fairly well [2] (a result already established in multiple previous studies; Monnier & Millan-Gabet [2002]; Eisner et al. [2004]; Isella et al. [2006]). Rim radii from the model fit are 0.19 AU (thickness 0.04 AU) for MWC275 and 0.21AU (thickness 0.05 AU) for AB Aur (see Table 3.4 for details). However, the standard model fails glaringly at fitting the long-baseline data. For baselines longer than 110m the standard rim predicts strong bounces in the visibility response which are not observed in the data.

The lack of bounce in visibility cannot be explained in the framework of the standard rim model. Models for NIR excess in Herbig Ae stars in which all of the

[2]The near-IR disk size obtained from the Keck Interferometer data is ∼20% larger than the size obtained with the CHARA data (June2004-Aug2006 epochs). The size determined from the S2W1 June2007 data also differs at the ∼25% level from the size obtained from earlier CHARA epochs. The size fluctuations could be related to the observed variability in the infrared photometry of MWC275 (Sitko et al. [2008]). Variability does not affect any of our conclusions.

excess arises in rims will display bounces in visibility at long baselines because of the presence of sharp ring-like features with high spatial frequency components in the corresponding images, even for the smoothest rims physically plausible.

The only explanation for the absence of long-baseline visibility bounce in the data is the presence of an additional smooth emission component within the dust destruction radius that suppresses the large visibility bounces seen in a rim-only model. The bottom panel in Fig 3.11 shows a standard model to which NIR emission has been added within the dust evaporation radius. Our data cannot uniquely constrain this emission profile and we assume a constant surface brightness disk (a uniform disk), which is a simple model. A rim + uniform disk model in which the uniform disk emission (refer Table 3.4 for details) accounts for 40-60% of the total K-band emission provides a good fit to the visibility (Fig 3.6) over the whole baseline range.

Besides the interferometry, emission inside the dust evaporation radius can also help explain the NIR flux budget of MWC275 and AB Aur. MWC275 and AB Aur have total K-band emission a factor of 10 larger than the stellar photospheric K-band emission, whereas the total emission produced by standard rim models (Isella & Natta [2005]) is only a factor of 3.5 larger (SED analysis will be presented in Chapter 5) than the photospheric emission. The emission component inside the dust rim can supply the "missing" K-band flux in MWC275 and AB Aur. In the next section we discuss candidates for the physical origin of this emission.

Table 3.4. MWC275 and AB Aur model parameters for K-band emission.

Star	model type	star emission (%)	dust-rim emission (%)	gas-disk emission (%)	rim inner radius AU
MWC275[a]	dust rim only	25	69	-	0.19
	dust rim+gas	10	29	56	0.22
AB Aur[a]	dust rim only	22	73	-	0.21
	dust rim+gas	8	22	65	0.24

[a]The models also include extended envelopes contributing 5% of the K -band emission (Monnier et al. [2006]).

3.6 Physical Interpretation

We consider 3 opacity candidates for providing the smooth K-band emission component: a) a dusty spherical halo around the stars (Vinkovic et al. [2006]), b) highly optically transparent/refractory dust extending inside the rim and c) gas inside the dust evaporation front. Vinkovic et al. [2006] showed that halo models can fit NIR SED and some early NIR interferometry data on Herbig Ae stars. However, the detection of asymmetries in NIR emission of MWC275 (§3.4) and other Herbig Ae/Be stars (Eisner et al. [2004]) supports a disk model over the spherically symmetric halo model of Vinkovic et al. [2006]. The gas densities in the inner disk are not high enough to let dust survive beyond 1900K (Pollack et al. [1994]), making optically transparent/refractory dust an unlikely candidate for the excess K-band emission.

Hot gas is an excellent candidate as a NIR emission source inside the dust sublimation radius. Molecular gas is known to have dense NIR opacity features at kilo-kelvin temperatures (Carr et al. [2004]; Ferguson et al. [2005]). The required gas emission levels to explain the long-baseline visibility data can be obtained with optically thin gas emission (optical depth $\tau \sim 0.15$, see §5.4.1 for a discussion on gas opacity) with

a temperature range of 2000K-3000K (Muzerolle et al. [2004]; Eisner [2007]). Our claim regarding the presence of gas emission inside the dust rim is further supported by the detection of the Brγ line in young star HD104327 (Tatulli et al. [2007]) on size scales similar to the dust destruction radius.

At first thought, presence of binary companions or source variability would also seem good explanations for the excess K-band emission and the lack of visibility bounce at long baselines. However, the presence of a binary companion within 0.5 AU of MWC275 that contributes $\sim$50% of the total near-IR emission will cause changes of $\sim$0.5 in the absolute visibility of the system at any given baseline over the multiple CHARA observation epochs. This variation is not seen in the data (see Fig. 3.6). Furthermore, Monnier et al. [2006] obtained NIR visibility and closure-phase data on MWC275 and found no evidence for a binary companion ruling out binarity as an explanation for the observations. A comparison between the Keck Interferometer and CHARA data (taken in different observation epochs) in Fig. 3.6 shows that MWC275 visibilities are time variable at the $\sim$20% level, suggesting that variability could complicate our analysis. However, the data from the S2W1 CHARA telescope pair (Fig. 3.6) were obtained on a single night and show a similar visibility-baseline trend as the rest of the data, disfavoring variability as an explanation for the observed trends. Thus, our conclusion on the presence of smooth gas emission inside the dust destruction radius is robust.

3.7 Discussion

In this work, we have conclusively shown the presence of strong NIR emission between the magnetospheric co-rotation radius and the dust sublimation radius in Herbig Ae stars MWC275 and AB Aur. The underlying mechanism for this emission is not known, requiring high resolution NIR spectroscopy and self-consistent modeling of the gas-dust transition region to identify the gas species and the physical processes responsible for the emission.

The detection of gas emission within the dust destruction radius through long-baseline interferometry is of special importance to understanding the star-disk connection. Accretion models for YSOs have tended to focus on two separate physical scales (i) the process of mass and angular momentum transport in the outer disk and (ii) gas accretion from a few stellar radii on to the stellar photosphere. Milli-meter interferometry and direct imaging in the mid-IR have allowed observational access to the outer disk while high-resolution optical-spectroscopy can probe the circumstellar environment around YSOs on scales of a few stellar radii. Our near-IR interferometry results on MWC275 and AB Aur provides exciting prospects for connecting the two scales and determining the structure of the gas flow from a few tenths of an AU down to the stellar surface. In the following paragraph, we describe NIR interferometry as a tool in probing accretion physics inside the dust rim.

In the regime where in the inner gas disk is optically thin, the Shakura-Sunyaev viscosity parameter for the gas disk can be constrained using a combination of NIR interferometry and optical spectroscopy. NIR interferometry in J, H and K bands can constrain the inner gas-disk surface density and temperature profiles. The surface

density of the disk is related to the mass accretion rate and the viscosity parameter in quasi-steady-state disks (Shakura & Sunyaev [1973]). Thus, simultaneous measurements of mass in-fall rates (through modeling of optical-emission lines and optical continuum excess above photospheric emission (Calvet & Gullbring [1998]; Muzerolle et al. [2001]) and the gas surface density profiles will directly constrain the viscosity parameter 'α' in the inner disk. This is key to understanding angular momentum transport in circumstellar disks.

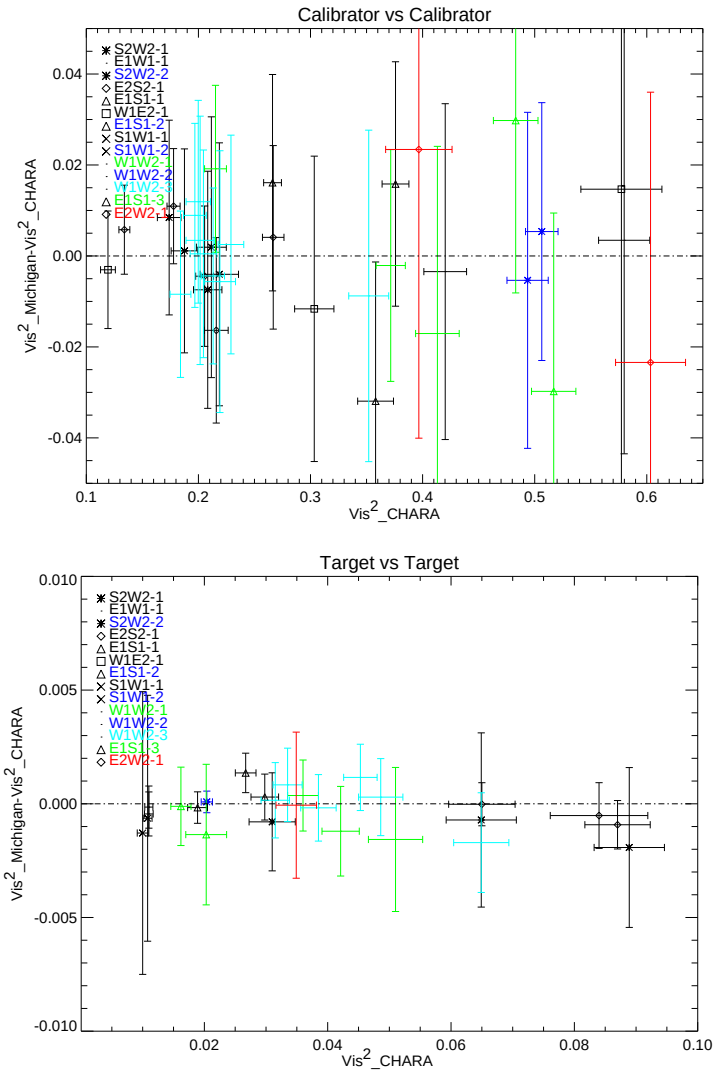

Figure 3.9 Comparison of CHARA V^2 results from two independent codes. The top panel shows differences in V^2 for the calibrators computed with the standard CHARA reduction package(V^2CHARA) and the code developed by Dr. John Monnier (V^2Michigan). The bottom panel shows differences for the science targets.
The uncertainty in V^2, caused by photon noise, read noise and scintillation noise, is estimated by measuring the distribution of V^2 determined from individual data scans.

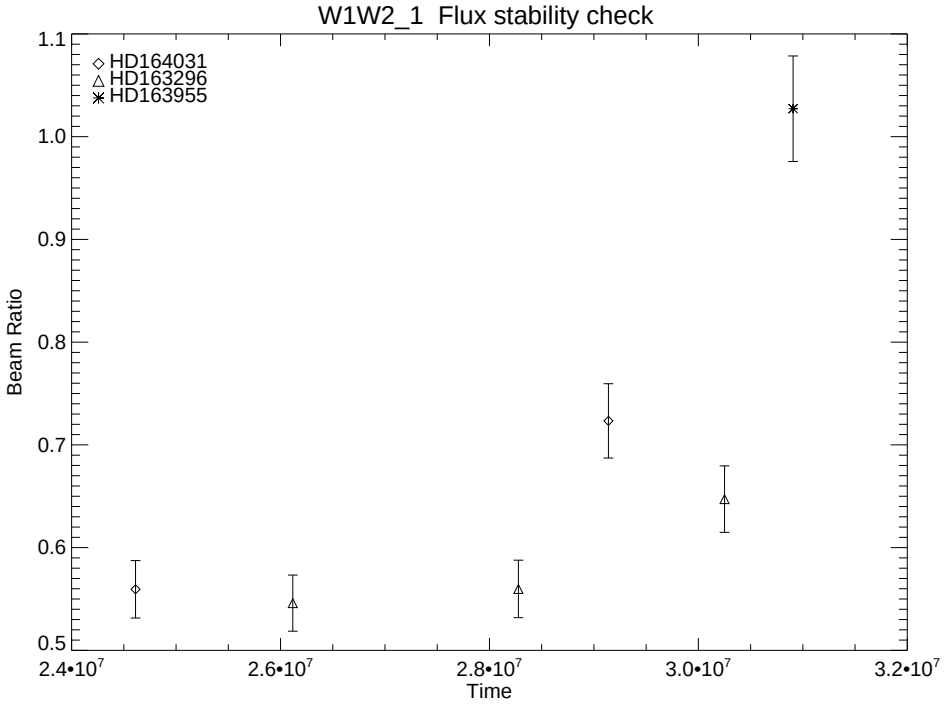

Figure 3.10 CHARA beam ratio stability. The near-infrared flux ratio of telescopes W1 and W2 as a function of time on MWC275 data set (July 22nd, 2006).

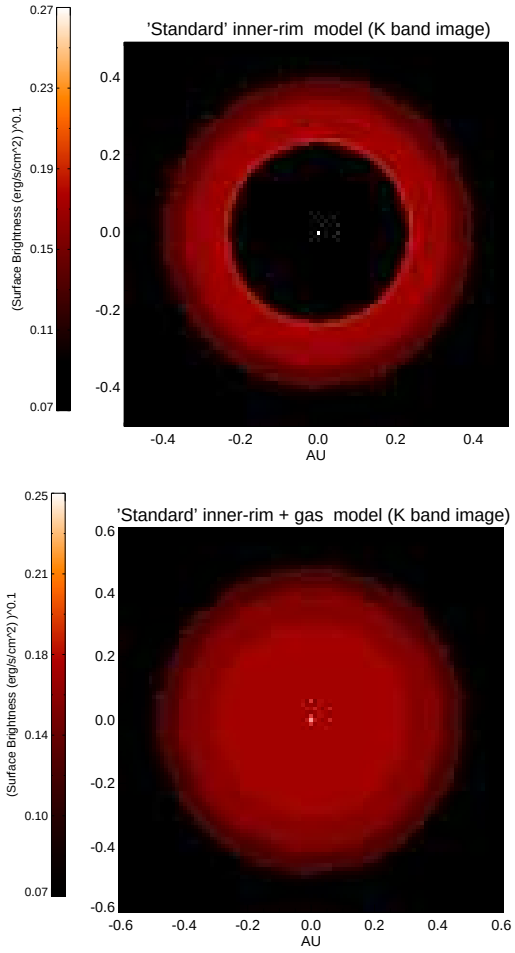

Figure 3.11 Representative models for near-IR emission in Herbig Ae stars. a) Top panel. A standard curved dust-rim-only model (Isella & Natta [2005]; Tannirkulam et al. [2007]) where the dust sublimation temperature is a power-law function of gas density (Pollack et al. [1994]). b) Bottom panel. Gas emission (modeled as a uniform disk centered on the star) has been added inside the dust rim in order to smooth out the emission profile.

Chapter 4

Circumstellar Disks in Mid-Infrared Emission

Abstract: The inner 30AU in circumstellar disks is the birth site for planets and understanding the temperature and density structure of this region has become an important goal of modern astrophysics. This portion of the disk emits strongly in mid-infrared (MIR) wavelengths making MIR spectroscopy and interferometry good tools for probing structure. In this chapter, we describe modeling results for MIR disk emission and make predictions for future observations with long-baseline MIR interferometry. We present preliminary work on characterizing the geometry of circumstellar disks based on observations from a novel Keck Segment Tilting Experiment. We also discuss the discovery of a circumbinary disk with Keck Experiment around the Herbig Be star v892 Tau first reported in Monnier et al. [2008a].

4.1 MIR emission morphology

Chapters 2 and 3 discussed the NIR emitting region in Herbig Ae disks. In the NIR, bulk of the emission arises from the dust evaporation front and hot gas inside the gas-dust transition region. However, at MIR wavelengths, emission comes from the rim as well as the flared disk beyond it. Figure 4.1 shows synthetic 10.7μm TORUS images of three rim+disk models introduced in Chapter 2. The rim has a high

surface brightness at 10.7μm, but only contributes about 30-50% of the integrated light (more precisely 38% in the large grain model, 55% in the dust segregation model and 32% in the small grain model). In contrast to 2.2μm emission, a large fraction of the emission at 10.7μm comes from the flared disk (Kenyon & Hartmann [1987]; Chiang & Goldreich [1997]) region on larger scales. Between the inner rim and the flared disk, there is a 'shadow region' (Dullemond et al. [2001]) which is not illuminated by the star directly. As discussed in van Boekel et al. [2005] and Tannirkulam et al. [2007], the two distinct regions of emission cause a knee in the visibility curves (Figure 4.2). The size and shape of the knee is affected both by the inner rim as well as the flared disk structure (van Boekel et al. [2005]).

van Boekel et al. [2004] studied the silicate feature in Herbig disks using mid-infrared interferometry (with VLTI-MIDI), and showed that dust on AU scales in Herbig disks are significantly more crystalline compared to the dust at tens of AU scale. The discussion in this section demonstrates that the present generation of long-baseline mid-infrared interferometers can be used to distinguish between models of the inner rim, thus providing information on dust processes that take place on even smaller scales at fractions of an AU.

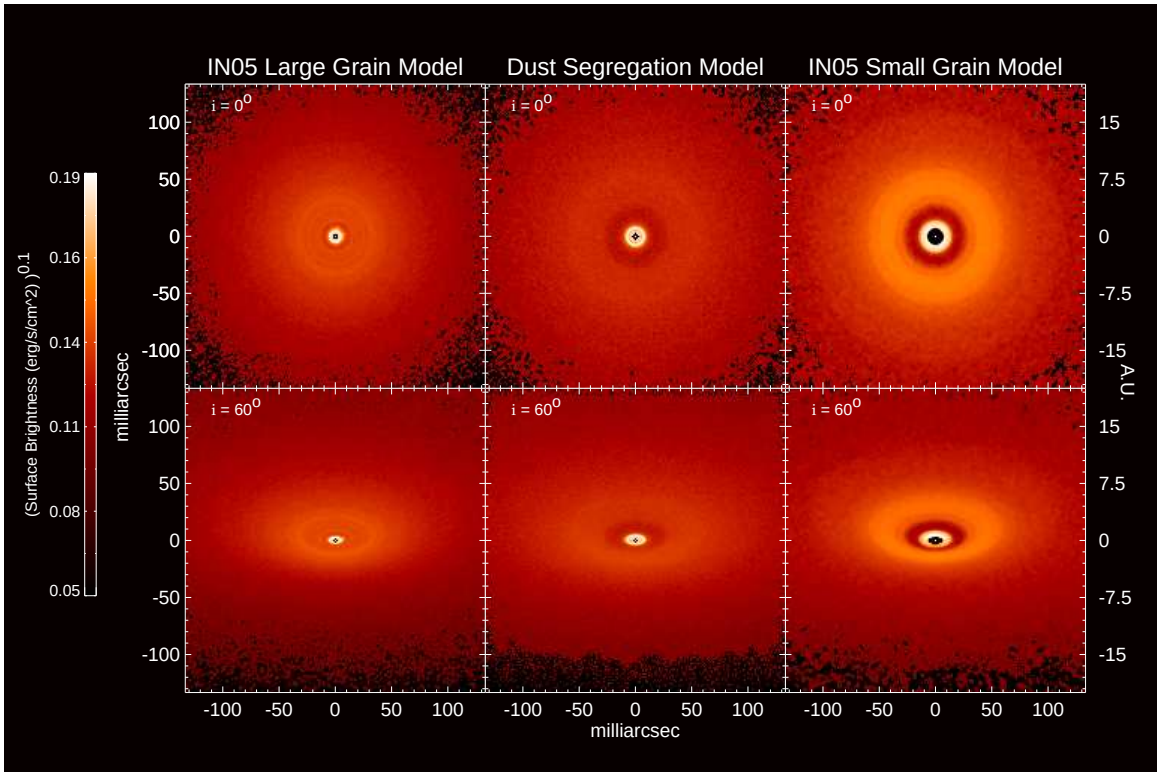

Figure 4.1 Synthetic 10.7μm images for rim models discussed in Chapter 2. The panels on the left and right are IN05 rims computed for 1.2μm (large grain) and 0.1μm (small grain) silicate dust. The center panels are images for the dust segregation model. The star is placed at 150pc with the stellar parameters described in Table 2.1. The star is unresolved at the image scale and is just one bright pixel at the center.

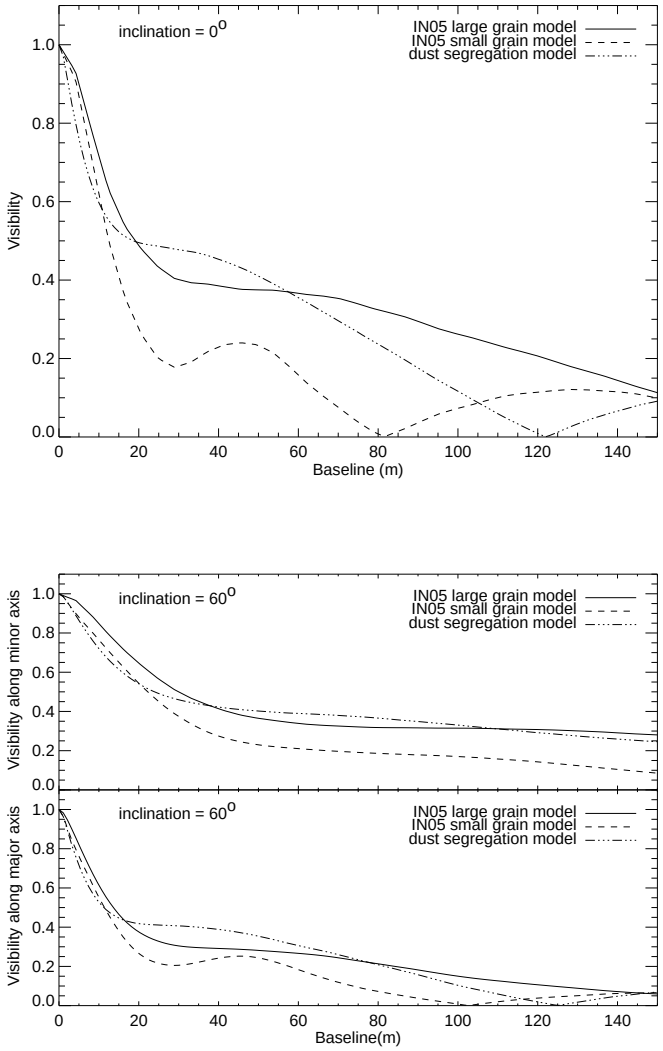

Figure 4.2 10.7μm visibilities for the IN05 and dust segregation models. The panel on top shows the visibilities for a face-on disk and the bottom panel shows visibilities computed along the major and minor axis for an inclined disk.

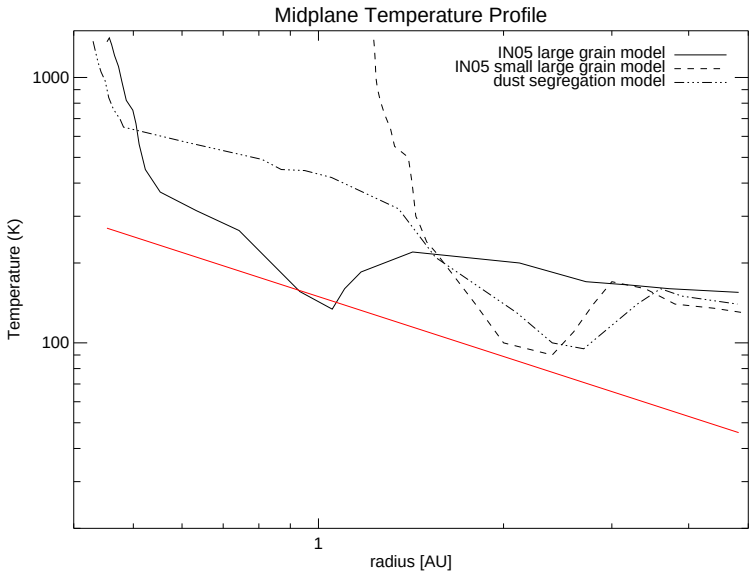

Figure 4.3 Midplane temperature profiles for disk models. The models differ in their inner-rim structure. The solid-red line is the viscous temperature for an accretion rate of $4\times10^{-8}M_{\odot}yr^{-1}$.

Fig 4.3 shows the midplane temperature profiles for the passive-disk models in Fig 4.1. The MIR shadow seen in Fig 4.1 is also reflected in the temperature structure. Moving away from the star in the radial direction, temperatures begin to fall. As the disk emerges out of the shadow of the inner rim, there is a small increase in temperature after which temperatures continue to fall again. In the models presented, the mass enclosed in the shadow is $\sim 0.002M_{\odot}$. Depending on the rim model, $\sim$ 1-15 Neptune masses of material in the shadow is below 150K which is the sublimation temperature of water ice. The presence of this cold reservoir of material close to the star (closer than expected in a disk model with no inner rim) could have important implications for chemistry and the abundance of volatile elements in planets.

The above discussion however assumes that the disk is passively heated and neglects the contribution of accretion energy. In the presence of disk accretion, the

viscous temperature in the midplane is given by (Hillenbrand et al. [1992]; Shakura & Sunyaev [1973])

$$T_{visc} = 26890 \left(\frac{M_*}{M_\odot}\right)^{0.25} \left(\frac{\dot{M}}{10^{-5} M_\odot yr^{-1}}\right)^{0.25} \left(\frac{R}{R_\odot}\right)^{-0.75} \left[1 - \left(\frac{R_*}{R}\right)^{0.5}\right]^{0.25}, \quad (4.1)$$

where M_* is the mass of the star, R_* is the stellar radius and $\dot{M}$ is accretion rate. A modest accretion rate of $4{\times}10^{-8} M_\odot yr^{-1}$ will increase the temperature in the shadow of the IN05 large grain model (Fig 4.3) by $\sim$ 30K, pushing the temperature above the sublimation point of water ice.

Having discussed the effects of the inner rim on disk structure and corresponding observable consequences, we now move on to study the disk at a larger scale of $\sim$ 10-30AU. In the following section, we describe the Keck Segment Tilting Experiment in the mid-infrared wavelengths and attempt at establishing trends between stellar spectral type, disk surface brightness and MIR colors, and the shape of the MIR SED. We also report the detection of a circumbinary disk around the Herbig Be star v892 Tau.

4.2 The Keck Segment Tilting Experiment

I was fortunate to be part of an exciting experiment designed and executed at the Keck Telescope by Prof. John Monnier and his collaborators -Dr. Peter Tuthill, Dr. Michael Ireland and Dr. R. Cohen. Precise measurements of partially resolved objects with 10-m class telescopes are delicate due to changes in atmospheric seeing between the science target and a Point Spread Function Calibrator. In order to avoid this problem, a novel experiment was conducted where four subsets of Keck

primary mirror segments were repointed and rephased so as to achieve four separate sparse aperture Fizeau interferometers, each with a separate pointing origin on the LWS detector (Jones & Puetter [1993]). Each mirror segment is 1.8m across and is smaller than the atmospheric coherence length of 5-10m at 10μm. This makes calibrations of seeing more robust.

Fig 4.4a shows one of the patterns color coded by the applied tilt to the mirror segments. The tilts cause star light to split into 5 separate images as illustrated in Fig 4.4b. Four images used for science and extracting fringe visibilities are arranged in 5"×5"squares on the LWS detector. The fifth image is projected 20" away from the detector. The segments contributing to the science light are arranged in a non-redundant pattern (giving 15 baselines between 2.6m and 9.3m) to extract fringe visibilities using Fourier analysis. Details of the experiment and the data reduction procedure are provided in Monnier et al. [2004]; Weiner et al. [2006]; Monnier et al. [2008b].

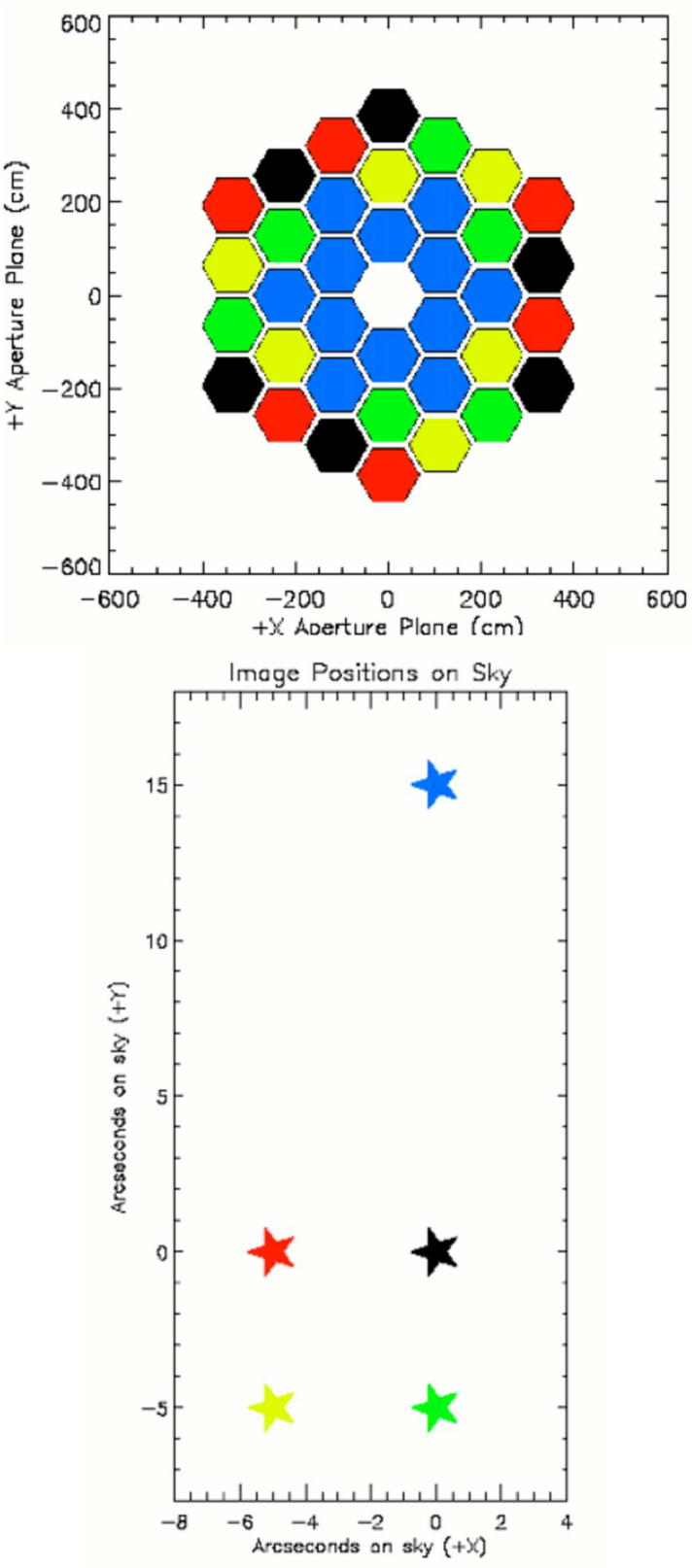

Figure 4.4 Keck Segment map. a) Top Panel. One of the Keck mirror tilt patterns known as "pattern 6". b) Bottom Panel. Corresponding image positions.

4.2.1 Geometric Models for MIR Emission in HAe/Be stars

Leinert et al. [2004] resolved 6 Herbig Ae/Be stars with the MIDI instrument on the VLT interferometer. A plot of the 12.5μm physical sizes vs their IRAS colors (Fig 4.5) hinted that Group I sources are larger and redder than the Group II sources (see section 1.3.1 for definition of Group I and Group II). This gave some evidence to the interpretation that Group I sources have disks that are more flared than Group II sources. To further investigate the relation between MIR observables and disk geometry, we surveyed 12 Herbig Ae and 13 Herbig Be stars (Monnier et al. [2008b]) with the Segment Tilting Experiment. While angular resolution of this experiment (30 mas) is much lower than that of VLTI-MIDI, we were able to observe a larger sample in a short time. The snapshot 2-dimensional uv coverage on the sky allowed us to detect disk asymmetries and we discuss the very interesting asymmetric disk of v892 Tau in section 4.3.

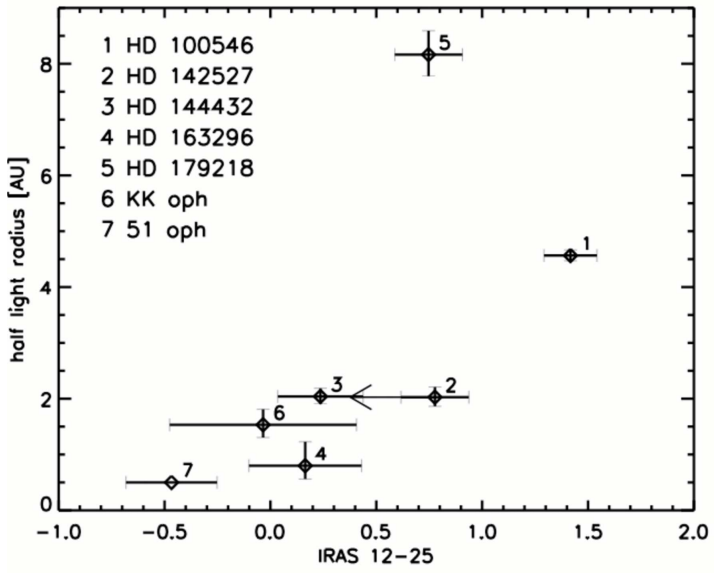

Figure 4.5 Disk size vs color. VLTI-MIDI 12.5μm size vs IRAS 12μm - 25μm color (Leinert et al. [2004]). The largest sources are red and belong to the Group I classification.

Fig 4.6 shows a summary plot of our results. In the HAe case, the Group II sources are clearly and bluer than Group I sources. There also appears to be a smooth trend between disk color and surface brightness. The HBe disks have a much higher surface brightness than predicted by passive flared disk models. We also note that the fraction of Group II sources in HBe systems is much smaller than in HAe systems. This seems to hold true even for the larger sample of HAe/Be stars whose ISO SEDs were analyzed in B. Acke's Thesis.

To motivate the choice of observables plotted in Fig 4.6 and to understand scaling relations between disk size, MIR flux and stellar luminosity, we follow the radiative transfer scheme and corresponding equations and notations presented in Chiang & Goldreich [1997]. The calculations are simple and conserve energy only approximately. More sophisticated, semi-analytic radiative transfer calculations are presented in Calvet et al. [1991] and Chiang et al. [2001]. The circumstellar disk is assumed to be a passive re-processor of stellar radiation. The model disk (Fig 4.7) consists of 2 layers - (i) an optically thin surface layer that absorbs stellar radiation. The super-heated dust in this layer radiates half of the IR radiation inward into the disk and the other half is radiated outwards. (ii) the inner disk which is optically thick to stellar radiation. The inner disk absorbs radiation from the surface layer and re-radaites at longer wavelengths. The inner disk is assumed to be isothermal perpendicular to the midplane.

The temperature of the surface layer is (Chiang & Goldreich [1997])

$$T_{ds} \approx \left(\frac{1}{\epsilon_s^{0.25}}\right)\left(\frac{R_*}{2R}\right)^{0.5} T_* \tag{4.2}$$

where ϵ is the ratio of planck-mean opacities of dust at the disk surface temperature and the stellar effective temperature, R is the cylindrical radius, R_* is stellar radius and T_* is the stellar effective temperature.

The inner disk can be divided into three regions. In region 1, the disk is opaque to surface radiation and to its own radiation. The temperature in region 1 is

$$T_i \approx \left(\frac{\alpha}{4}\right)^{0.25} \left(\frac{R_*}{R}\right)^{0.5} T_*. \tag{4.3}$$

α is the grazing angle at which starlight strikes the disk. In the flaring region of the disk, α can be approximated as

$$\alpha \approx \frac{0.4R_*}{R} + R\frac{d}{dR}\left(\frac{H}{R}\right), \tag{4.4}$$

H is the height of the visible photosphere above the disk midplane. For a power-law disk with $H = CR^{\gamma}$ ($\gamma > 1$),

$$\alpha \approx \frac{0.4R_*}{R} + CR^{\gamma-1}, \tag{4.5}$$

The temperature in region 2 of the inner disk, where the disk is optically thin to its own radiation but opaque to radiation from the surface is

$$T_i \approx \left(\frac{\alpha}{4\epsilon_i \kappa_V \Sigma}\right)^{0.25} \left(\frac{R_*}{R}\right)^{0.5} T_*, \tag{4.6}$$

κ_V is the dust opacity at visual wavelengths and Σ is the disk surface density.

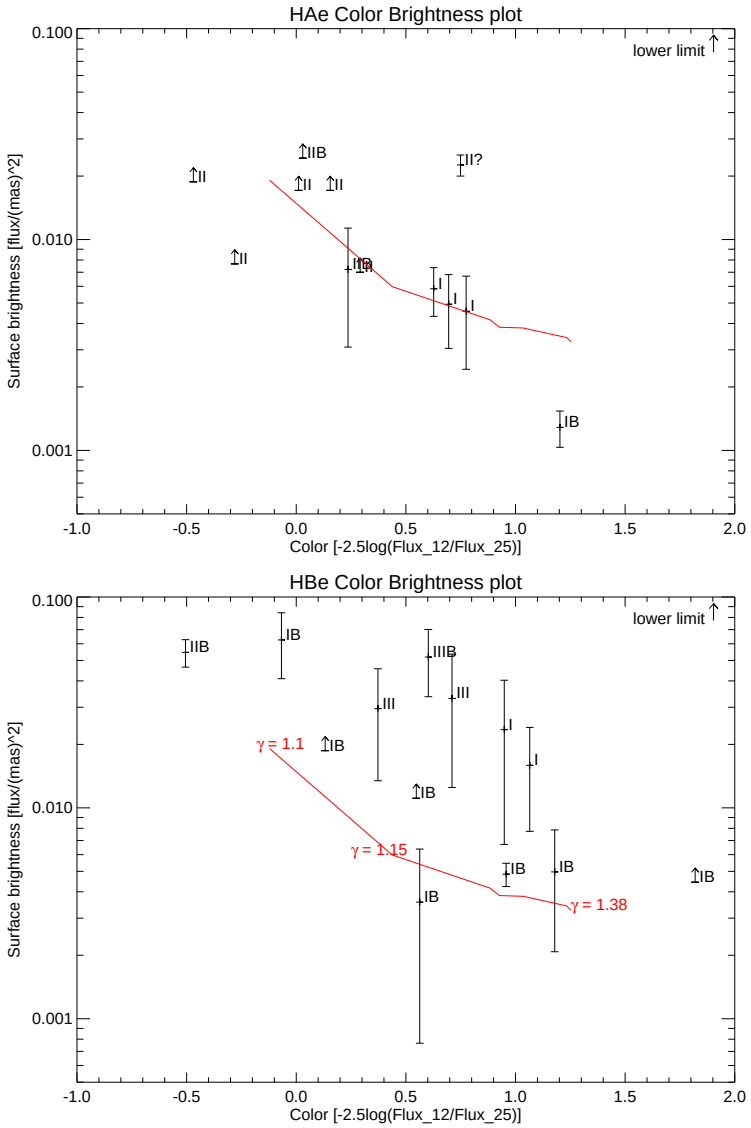

Figure 4.6 Surface brightness vs color. a) Top Panel. Surface brightness vs color plot for Herbig Ae stars. b) Botttom Panel. Surface brightness vs color plot for Herbig Be stars. The 10μm sizes and fluxes were measured with the Keck Segment Tilting Experiment. The x axis plots IRAS colors. Binaries are labeled B, and the Groups are indicated as I, II or III. Group III sources have large accretion rates/envelopes and cannot be treated in the framework of passive disk systems.
The solid-red line is a theoretical brightness vs color curve obtained for the disk models described in Fig 4.8. The disk-flaring parameter 'γ' is marked in the lower panel.

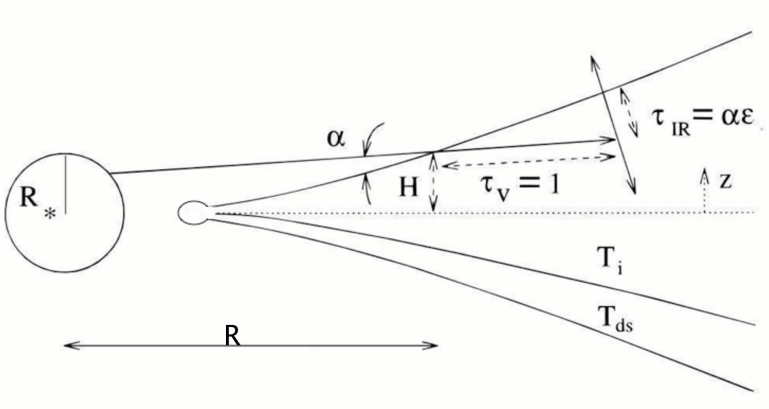

Figure 4.7 Chiang & Goldreich [1997] 2-layer passive-disk model. An inner rim has been added. Stellar radiation reaches the flared surface at an angle α. Starlight is absorbed in the surface layer, half of which is emitted to infinity and the other half heats the disk interior.

At large radii, the inner disk is transparent to the surface radiation as well and the temperature in this region is given by

$$T_i \approx \left(\frac{\alpha\epsilon_s}{4\epsilon_i}\right)^{0.25} \left(\frac{R_*}{R}\right)^{0.5} T_* \tag{4.7}$$

In addition to the flared disk, the inner rim also contributes to MIR emission. The radius of the inner rim is given by $R_{\rm evp}$ (see Isella et al. [2006]; Calvet et al. [1991]) is

$$R_{\rm evp}\,[\rm AU] = 0.034\,[\rm AU] \left(\frac{1500K}{T_{\rm evp}}\right)^2 \left[\left(\frac{L_*}{L_\odot}\right)\left(B + \frac{1}{\epsilon}\right)\right]^{1/2}, \tag{4.8}$$

L_* is luminosity of the star in solar units and $\rm T_{evp}$ is dust sublimation temperature. B is a dimensionless diffuse heating term, characterizing the rim optical depth to its own thermal emission. The thickness of the rim depends on dust composition and spatial distribution (Chapter 2).

Equations (4.2), (4.3), (4.6), (4.7) and (4.8) show that for a fixed temperature, the size of the emitting region depends on dust composition, the disk flaring parameter

γ (γ controls α) and $L_*^{0.5}$. The SED for a face-on disk can be computed from

$$L_\nu = 8\pi^2\nu \int_{R_i}^{R_o} RdR \int_{-\infty}^{+\infty} dz \frac{d\tau_\nu}{dz} e^{-\tau_\nu} B_\nu(T). \tag{4.9}$$

(4.9) can be approximated as

$$L_\nu \sim 8\pi^2 R^2 \nu B_\nu(T)\tau_\nu \sim \alpha L_*/2 \tag{4.10}$$

for the surface layer and as

$$L_\nu \sim 8\pi^2 R^2 \sigma T_i^4 \sim \alpha L_*/2 \tag{4.11}$$

for the opaque interior.

Equations (4.10) and (4.11) show that the disk color, which is the ratio of fluxes at two wavelengths is independent of stellar luminosity and depends on disk geometry and dust distribution. The surface brightness of the disk which is given by

$$L_\nu/(\text{size})^2 \sim \alpha L_*/L_* \tag{4.12}$$

is also independent of stellar luminosity. Both surface brightness and color are independent of distance (many YSO distances are not well known). Thus, we argue that plotting MIR surface brightness vs color (Fig 4.6) is a good way to probe disk geometry.

To study the dependence of surface brightness and color on disk geometry, we constructed a series of disk models with flaring parameter γ varying between 1.1 and 1.38 (Fig 4.8). The disks are composed of 1.2μm grains, have a total mass of $0.01 M_\odot$ with a gas to dust mass ratio of 100:1. The surface density varies as $(\text{radius})^{-1}$. The central star is blackbody with $T_{eff} = 10{,}000$K and luminosity $45 L_\odot$.

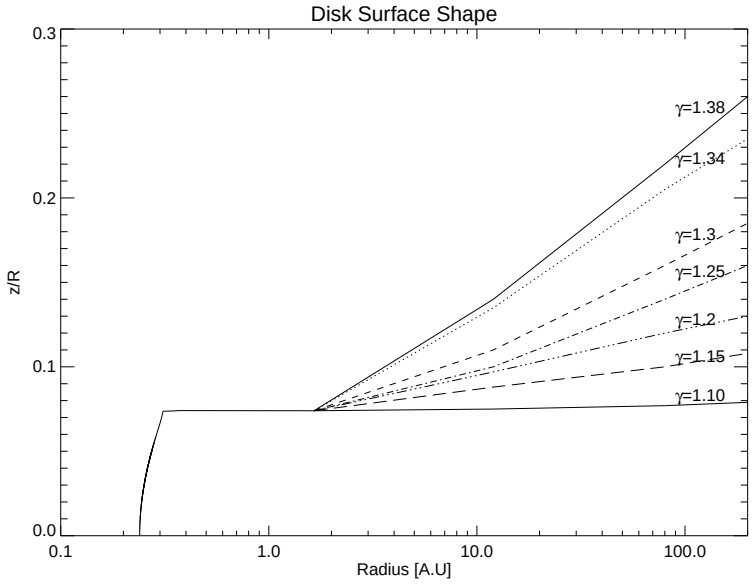

Figure 4.8 Disk geometries used to construct theoretical color-brightness track. The figure shows the τ=1 surface at 5500Å. The y axis is the polar angle (0 is the mid-plane) in radians.

The radiative transfer was computed using TORUS (Chapter 2). The solid green line in Fig 4.6 shows the model surface brightness-color relationship. For γ=1.1, the MIR emission entirely arises in the inner rim. The surface brightness is high and the disk appears blue at MIR wavelengths. As γ is increased, the flared disk becomes the dominant MIR flux contributor. The disk becomes redder and the surface brightness falls sharply. The theoretical track traces the observed trend for Herbig Ae stars. However, Herbig Be stars typically have a much higher surface brightness for the same color. This agrees well with NIR interferometry results (Eisner et al. [2004]; Monnier et al. [2005]) showing that early Herbig Be stars are too small to be consistent with the size-lumionosity relations found for lower luminosity stars. The smaller size and the larger surface brightness might be caused by high accretion rates in these systems, in which case passive disk models are not appropriate.

For Herbig Ae sytems, our results lend support to previous work (Dullemond & Dominik [2004]; Leinert et al. [2004]; Acke & van den Ancker [2004b]) arguing that Group I sources are more flared than Group II sources. Acke & van den Ancker [2004b] demonstrated that Group I sources have a smaller amount of cold grains than Group II sources based on sub-mm SED slopes. Under the assumption that grains grow as disks evolve in time, Acke & van den Ancker [2004b] favor an evolution scenario where Group I sources transition to Group II sources.

The work presented here is preliminary and we will be refining our calculations and arguments for a journal publication in the near future. We will also be investigating the influence of companions on our interpretation of the data.

4.3 The Circumbinary Disk in V892 Tau

Here, we present the discovery of a circumbinary disk around the Herbig Be system v892 Tau first reported in Monnier et al. [2008a]. v892 Tau (Elias-1, Elias 3-1) is a young stellar object in the Taurus-Aurigae star forming region ($d = 140\ pc$, Kenyon et al. [1994]). Its visible spectrum is classified as spectral type B8V (Hernández et al. [2004]). The spectral energy distribution (SED) of v892 Tau is dominated by bright thermal emission in the mid-infrared (Hillenbrand et al. [1992]), with relatively large line-of-sight extinction in the visible. Despite being one of the closest Herbig stars and after decades of multi-wavelength observations, the nature of v892 Tau is still uncertain.

The SED suggests v892 Tau is either a young embedded Class I source (Lada [1987]) still surrounded by its nascent envelope or a more evolved, Class II object (i.e,

Herbig Ae/Be star) seen through its edge-on disk. Indeed, recent studies (Robitaille et al. [2006]) suggest between 7-20% of disk objects would appear embedded due to geometrical projection when based solely on SED analysis. Spatially-resolved imaging can easily distinguish between these two scenarios, and early speckle interferometry (Kataza & Maihara [1991]; Haas et al. [1997]; Leinert et al. [2001]) suggested the presence of an extended and elongated nebula in the near-infrared that could be due to scattering in bipolar lobes.

The high-resolution speckle imaging of Smith et al. [2005] clearly resolved the K band ($\lambda = 2.2\mu$m) emission to be coming from two unresolved stars in v892 Tau with little or no sign of a nebula or extended emission. The two stars of roughly equal brightness had an apparent separation of 55 milliarcseconds (7.7 AU) and some evidence of orbital motion was seen between epochs separated by 7 years.

Although this binary should have a dramatic effect on the infrared emission, carving out a large hole in the circumbinary disk, recent analysis of the SED of v892 Tau including ISO data (Acke & van den Ancker [2004a]) uncovered no distinct signature of the underlying binary[1]. Other workers (Liu et al. [2005, 2007]) made use of the technique of nulling interferometry in the mid-infrared ($\lambda = 10.3\mu$m) to marginally resolve v892 Tau (FWHM $\sim$20 AU) along PA 164° consistent with normal (single-star) disk emission.

To resolve these some of these mysteries, we observed v892 Tau with the Keck Segment Tilting Experiment ($\lambda_0 = 10.7\mu$m, $\Delta\lambda = 1.55\mu$m) on UT2004Aug31, UT

[1]Acke & van den Ancker [2004a] did note strong PAH emission and anomalous infrared colors.

2004Sep01, and UT2005Feb19 at the Keck-1 telescope, discovering extended resolved emission which we interpret to be coming from a circumbinary disk. We also present a new SED analysis which provides an improved determination of the system luminosity and our viewing geometry. In addition to the MIR observations, Dr. Monnier and collaborators also observed v892 Tau in the K-band (λ =2.21μm, $\Delta\lambda$ =0.43μm) on UT2004Sep04 with NIRC camera (Matthews et al. [1996]) in conjunction with an annulus aperture mask (Tuthill et al. [2000]) placed in front of the secondary mirror.

4.3.1 Analysis

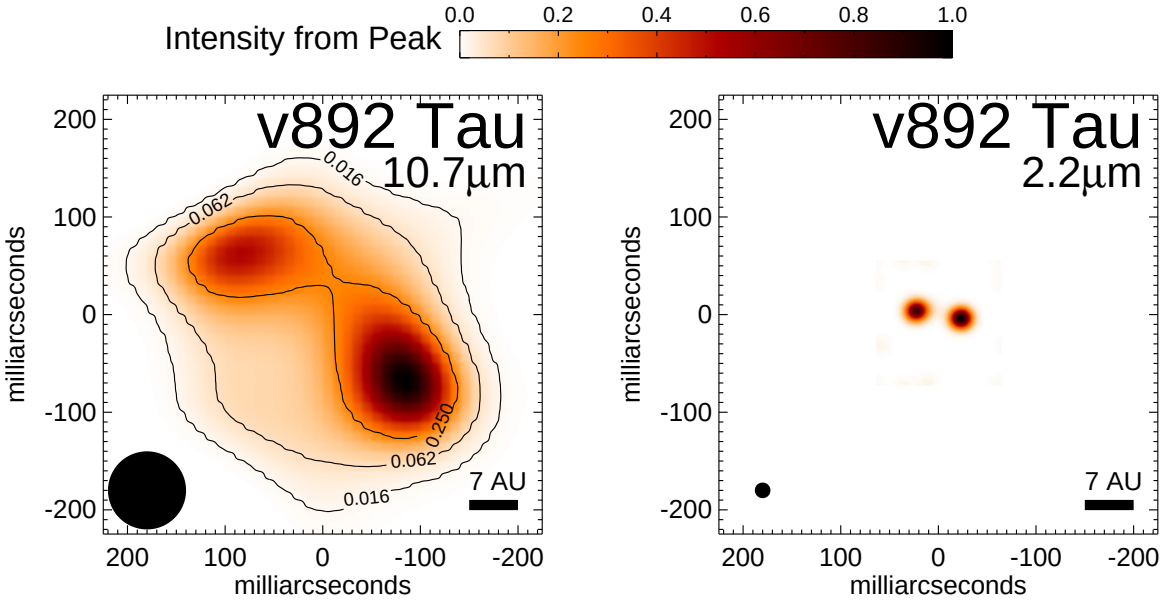

Figure 4.9 Image reconstructions of v892 Tau using the BSMEM software. At the bottom-left of each panel, an estimate of the resolution of each image is included, corresponding here to 80 mas at 10.7μm and 16 mas at 2.2μm. Contour levels are shown for the extended emission in the mid-infrared spaced logarythmically in factors of 4: 25%, 6.3%, and 1.6% of the peak. The scale bar applies for a distance of 140 pc. For orientation, East points left and North points up.

Using the BSMEM (Buscher [1994]; Lawson et al. [2004, 2006]) image reconstruction software Dr. Monnier created aperture synthesis images of v892 Tau in the mid and near-infrared (Fig 4.9).

The mid-infrared image shows elongated emission, approximately 320 mas by 180 mas in full extent, elongated along PA 50°. The two bright lobes in the image are separated by 210 mas (30 AU) with the south-west side being significantly brighter. A two-dimensional Gaussian fit to the visibility data gives a FWHM 244±6 mas × 123±9 mas along PA 49±1°. A more suitable model for a circumbinary or transitional disk would be a tilted and asymmetric ring of emission that is nearly unresolved along the minor axis. Following the parameterization of Monnier et al. [2006], Dr. Monnier fitted a "skewed asymmetric ring model" to the interferometry data here to better estimate the inner hole diameter. The best fitting model had an inner-hole diameter of 247×121 mas (35×17 AU) along PA 53°, with a 40% skew along PA 284° (the thickness of the ring followed a gaussian profile with a FWHM of 25% ring radius). For purposes of §4.3.2, we will assume the central hole in the circumbinary disk has a radius of 17.5 AU. The scale of the MIR emission is more than 4× larger than the separation of the binary at the heart of this system, and the elongation is along a distinctly-different position angle.

Figure 4.9 shows the BSMEM image of v892 Tau at 2.2μm. The binary nature of this target as first reported by Smith et al. [2005] is confirmed here. Combining the new binary measurement (at 2004.67) with the 1996.75 and 2003.76 measurements from Smith et al. [2005], Dr. Monnier obtained rough estimates for the binary parameters. The best fit parameters are e =0.1, P = 13.6 yrs, a = 73.5 mas (10 AU), $i = 64.4°$, $\omega = 224.4°$, $\Omega = 33.6°$ and T_O = 55355.8 MJD.

4.3.2 Discussion and Conclusion

We interpret the mid-infrared emission of v892 Tau as a circumbinary disk based on several arguments. The MIR emitting region is much larger than the separation between the binary components, ruling out models which have all the MIR emission coming from disks around the individual stars. In theoretical models of tidal truncation (Artymowicz & Lubow [1994]), the circumbinary disk has an inner hole approximately 1.8-2.6× larger than the semi-major axis of the binary system (for eccentricity between 0 and 0.25). For comparison, our best estimates of the hole radius and orbital semi-major axis are 17.5 AU and 10 AU respectively – giving a ratio of 1.75 which is close to the theoretical expectation. Additionally, the position angle and derived inclination angle of the mid-infrared emission (PA$\sim$50°, i $\sim$60°) is similar to those derived from the orbit (PA$\sim$34°, i $\sim$64°) and the mild asymmetry in the mid-IR emission suggests dynamical interactions between an eccentric binary and the surrounding disk (via resonances or disk warping).

We further test the circumbinary disk hypothesis by analyzing the spectral energy distribution (SED). The SED shows a large mid-IR bump similar to that seen in "transitional" disks (Calvet et al. [2002]; Espaillat et al. [2007]). By reddening template Kurucz spectra for B8V stars, we can fit the near-IR emission with mostly photospheric light (some NIR emission from hot dust is allowed but not well constrained) assuming $A_V = 10.95$ yielding a combined stellar luminosity of 400 $L_\odot$, reasonable for two B8V stars. Our new proposed SED decomposition for v892 Tau can be found in Figure 4.10, showing that the rising MIR flux can be roughly characterized as a T$\sim$ 450 K blackbody, consistent with emission from the warm inner

wall of the circumbinary disk.

Using equation (2.9), the predicted radius for the warm inner wall for the above stellar luminosity (assuming 0.25 μm dust grains) is 18 AU – consistent with our derived inner hole radius of 17.5 AU based on imaging. Furthermore, we find that the scale height of this wall at 18 AU is $\sim$ 1.8 AU (Dullemond et al. [2001]) which can produce the observed line-of-sight $A_V \sim 11$ for the disk inclination of $\sim 65^o$. This latter phenomena may not be widely appreciated – circumbinary (or transitional) disks have warm puffed-up inner walls (the rim scale height is a stronger function of radius than temperature) at large radii that effectively increases the possibility that central stars will be obscured or at least reddened as seen by distant observers.

In the following chapter, we generate models that explain the SED (Appendix B), NIR interferometry from CHARA (Chapter 3) and MIR interferometry from the Keck Segment Tilting Experiment for Herbig Ae stars MWC275 and AB Aur.

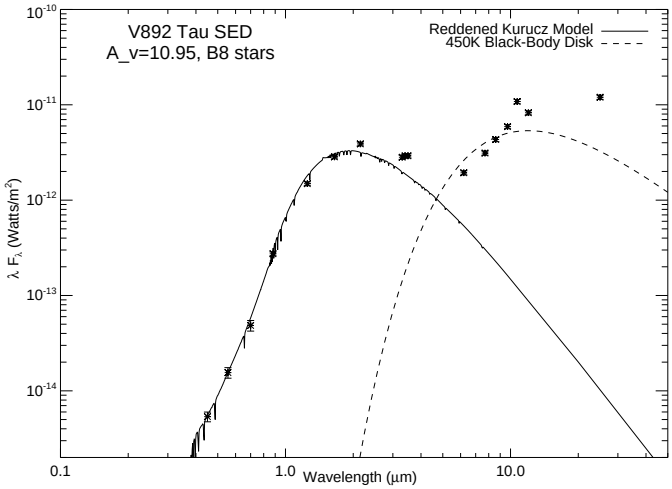

Figure 4.10 SED for v892 Tau. The photometry is from Strom & Strom [1994]; Acke & van den Ancker [2004a]; Herbst & Shevchenko [1999] and our own JHK observations from MDM Observatory. The solid and dotted lines represent our proposed decomposition of star plus disk. We have plotted the contribution from the reddened ($A_V = 10.95, R_V = 6.4$) stellar photospheres (2×B8V, system luminosity of $400L_\odot$) and the contribution from the "warm inner wall" of the circumbinary disk with temperature T∼450K.

Chapter 5

Comprehensive Models for SED and Interferometry

Abstract: We present comprehensive models for the Herbig Ae stars MWC275 and AB Aur that aim to explain their spectral energy distribution (from UV to millimeter) and long baseline interferometry (from near-infrared to millimeter) simultaneously. Data from the literature, combined with new mid-infrared (MIR) interferometry from the Keck Segment Tilting Experiment, are modeled using an axisymmetric Monte Carlo radiative transfer code. Models in which most of the near-infrared (NIR) emission arises from a dust rim fail to fit the NIR spectral energy distribution (SED) and sub-milli-arcsecond NIR CHARA interferometry. Following Chapter 3, we include an additional gas emission component with similar size scale to the dust rim, inside the sublimation radius, to fit the NIR SED and long-baseline NIR interferometry on MWC275 and AB Aur. In the absence of shielding of star light by gas, we show that the gas-dust transition region in these YSOs will have to contain highly refractory dust, sublimating at $\sim$1850K. Despite having nearly identical structure in the thermal NIR, the outer disks of MWC275 and AB Aur differ substantially. In contrast to the AB Aur disk, MWC275 lacks small grains in the disk atmosphere capable of producing significant 10-20 μm emission beyond $\sim$7AU,

forcing the outer regions into the "shadow" of the inner disk.

5.1 Introduction

Most interferometric studies of Herbig Ae (HAe) stars have relied on simple geometric models (Mannings & Sargent [1997]; Millan-Gabet et al. [1999, 2001]; Eisner et al. [2003, 2004]; Monnier et al. [2005]) that explain the emission geometry of the system in only narrow wavelength ranges. This method, albeit extremely useful in elucidating some of the morphology details, is not adequate for exploring the interdependency in structure of the inner and outer parts of the disk. A number of studies (Dullemond et al. [2001]; Dullemond & Dominik [2004]; van Boekel et al. [2005]) have shown that the structure of the inner disk at fractions of an AU scale clearly affects the structure of the outer disk. A complete understanding of the circumstellar disk structure in HAe stars therefore requires models that simultaneously explain the SED and interferometry over a large wavelength range. Such models have begun to appear in the literature only recently (Pontoppidan et al. [2007]; Kraus et al. [2008a]).

In this chapter, we develop comprehensive disk models to explain the SED and interferometry of the HAe stars MWC275 and AB Aur. MWC275 and AB Aur are prototype pre-main-sequence stars of similar ages and spectral type with extensive circumstellar disks. Due to the availability of photometric and interferometric data over a large wavelength range, MWC275 and AB Aur are ideal candidates for testing disk models for YSOs. The extent of their circumstellar-dust disks was first measured by Mannings & Sargent [1997] to be several 100AU using the Owens Valley Radio Observatory (OWRO). Natta et al. [2004] resolved the MWC275 disk in the mm and

reported a de-convolved dust-disk size of 300AU×180AU. More recently, Isella et al. [2007] analyzed IRAM, SMA and VLA continuum and ^{12}CO, ^{13}CO and ^{18}CO line data constraining the gas-disk radius to be 540AU with the gas in Keplerian rotation around the central star. Scattered light studies of MWC275 (Grady et al. [2000]) and AB Aur (Grady et al. [1999]; Oppenheimer et al. [2008]) show the presence of arcs and rings in the circumstellar disk. Corder et al. [2005] resolved the AB Aur CO disk radius to be ∼600AU, finding strong evidence for Keplerian rotation for the bulk of the disk. Corder et al. [2005] and Lin et al. [2006] detected spiral arms in CO emission with radii of ∼150AU, while Fukagawa et al. [2004] detected similar structure in Subaru H-band scattered light images. AB Aur also has substantial envelope material on scales larger then 600 AU (Grady et al. [1999]; Semenov et al. [2005]; Corder et al. [2005]; Lin et al. [2006]).

As discussed in Chapter 4, MIR emission probes the giant planet formation region in circumstellar disks (Calvet et al. [1991]; Chiang & Goldreich [1997]; Dullemond et al. [2001]) with the emission arising from warm dust (T > 150K). Meeus et al. [2001] and van Boekel et al. [2005] used the 10μm MIR silicate emission feature from MWC275 and AB Aur to show that dust grains in these systems had grown larger than the typical interstellar medium grain sizes. Mariñas et al. [2006] imaged AB Aur at 11.7μm and found the emission FWHM size to be 17±4 AU consistent with the flared disk models of Dullemond & Dominik [2004]. In this chapter, we present new 10μm measurements of AB Aur and MWC275 with the Keck Segment Tilting Experiment (described in §5.2, Monnier et al. [2004]). In contrast to AB Aur, the MWC275 disk is unresolved by the Segment Tilting Experiment (maximum baseline

of 10m), requiring the VLT Interferometer (100m baseline) to probe to its MIR structure (Leinert et al. [2004]). These observations suggest that MWC275 disk differs considerably from AB Aur and we present a detailed comparison of the two disk structures in the discussion (§5.6).

Thermal NIR emission probes hot regions (typically the inner AU) of the disk with temperatures greater than 700K. The NIR disks of MWC275 and AB Aur were first resolved with IOTA by Millan-Gabet et al. [1999, 2001] and subsequently observed at higher resolution with PTI (Eisner et al. [2004], Keck Interferometer (Monnier et al. [2005]), and the CHARA interferometer array (Tannirkulam et al. [2008]). In Chapter 3, we showed that inner-disk models in which the majority of the K-band emission arises in a dust rim (Dullemond et al. [2001]; Isella & Natta [2005]; Tannirkulam et al. [2007]) fail to fit the CHARA data at milli-arcsecond resolution. We also demonstrated that the presence of additional NIR emission (presumably from hot gas) inside the dust destruction radius can help explain the CHARA data and the NIR SED. First calculations for the effects of gas on rim structure (Muzerolle et al. [2004]) showed that for plausible disk parameters, presence of gas does not modify dust-rim geometry significantly. Besides a poorly understood interferometric visibility profile, MWC275 also displays as yet ill-understood NIR and MIR SED time variability (Sitko et al. [2008]) which has been interpreted as variations of the inner disk structure. In §5.4 and §5.5 we present a detailed analysis of the NIR visibility and SED for MWC275 and AB Aur, placing constraints on the wavelength dependence of the opacity source inside the dust destruction radius.

In this study, we focus on (i) explaining the inner-disk structure and discuss

important open problems and (ii) modeling the MIR emission morphology of the disks and the shape of the MIR spectrum. The chapter is organized into 7 sections with §5.2 detailing the observations. §5.3 explains the disk model and the modeling strategy. §5.4 and §5.5 analyze MWC275 and AB Aur SED and visibilities in relation to the disk models. We present a discussion on our results and our conclusions in §5.6 and §5.7 respectively.

5.2 New Observations and Literature Data

The properties of the circumstellar disks in MWC275 and AB Aur have been constrained using IR and mm interferometry and the SED. We include NIR interferometry from the CHARA array presented in Chapter 3, MIR interferometry from the Keck Segment Tilting Experiment and mm interferometry from the literature in our analysis. Optical and NIR photometry obtained at the MDM Observatories, and mid and far-infrared data from ISO are also included to constrain model SED. We describe the data in detail in the following paragraphs.

MW275 and AB Aur were observed with the Keck Segment Tilting Experiment (Chapter 4) to study their MIR emission morphology. The calibrated data are listed in Table 5.1. In addition to the Keck Segment Tilting data, we also include MWC275 MIR intereferometry from VLTI-MIDI (Leinert et al. [2004]) in our analysis.

Millimeter interferometry from Mannings & Sargent [1997], Natta et al. [2004], Semenov et al. [2005], Lin et al. [2006] and Isella et al. [2007] are used to constrain the circumstellar disk masses and disk sizes and surface density profile. In conjunction with the interferometry, the shape of the mm SED provides information on sizes of

Table 5.1 Keck Segment Tilting uv-averaged data for MWC275 and AB Aur.

UT-Date of Observation	Baseline(m)	Calibrated Visibility	Calibrator Names
		MWC275	
2004Sep01	3.03	0.969±0.049	v3879 Sgr
”	4.72	0.944±0.040	”
”	5.49	0.946±0.036	”
”	7.21	0.942±0.033	”
”	8.43	0.963±0.033	”
		AB Aur	
2004Aug30, 31 & Sep01	3.03	0.870±0.039	iota Aur
”	4.72	0.823±0.027	”
”	5.49	0.807±0.033	”
”	7.21	0.753±0.047	”
”	8.43	0.708±0.039	”

the dust grains in the bulk of the circumstellar disks.

To constrain the SED computed from radiative transfer models we obtained optical and NIR photometry on MWC275 and AB Aur with the MDM 2.4m telescope at Kitt Peak (refer §B.2). Due to the high brightness of our targets, we defocussed the telescope during observations to avoid camera saturation. After bias correction, flat fielding, and background subtraction, the reduced images were used to obtain source counts using ATV - an aperture photometry code (Barth [2001]). Targets were calibrated using Landoldt standards (Landolt [1983]). The calibrated UBVRI-JHK photometry are listed in Tables B.2 and B.3 in the Appendix. We also include photometry for a number of other YSOs that we observed. NIR photometry from Sitko et al. [2008] , mid and far-IR SED from Meeus et al. [2001] and mm fluxes (Mannings & Sargent [1997]; Natta et al. [2004]; Semenov et al. [2005]; Lin et al. [2006]) were also used in the model analysis. van Boekel et al. [2005] modeled the 10μm spectra of a large sample of Herbig Ae stars and derived the mineralogy and

Table 5.2. Basic stellar properties and photometry for MWC275.

Property	Value
RA	$17^h\ 56^m\ 21.29^s$
Dec	$-21^o\ 57'\ 21.8''$
Spectral Type	A1e[a]
T_{eff}	9500K[a]
Luminosity	36 $L_\odot$[a]
Distance	122pc[a]
Mass	$2.3M_\odot$[a]
U	-
B	$6.98\pm.08$[b]mag
V	$6.84\pm.06$[b]mag
R	$6.86\pm.05$[b]mag
I	$6.71\pm.07$[b]mag
J	$6.20\pm.08$[b]mag
H	$5.48\pm.07$[b]mag
K	$4.59\pm.08$[b]mag

[a]Stellar parameters from Monnier et al. [2006], Natta et al. [2004] and references therein.

[b]Photometry obtained at MDM Observatories (longitude: -111.67^o, latitude:31.95^o) in 2006 June.

typical grain sizes responsible for the emission. We use results from van Boekel et al. [2005] for fixing the composition of dust grains in the atmosphere of the MWC275 and AB Aur disks.

A compilation of stellar properties and circumstellar disk properties extracted from the literature is listed in Tables 5.2, 5.3, 5.4 and 5.5.

5.3 Circumstellar Disk Modeling

The circumstellar material around MWC275 and AB Aur is modeled as a passive dust disk reprocessing stellar radiation (Dullemond et al. [2001]). The disk is in

Table 5.3. Basic stellar properties and photometry for AB Aur.

Property	Value
RA	$04^h\ 55^m\ 45.84^s$
Dec	$+30^o\ 33'\ 04.29''$
Spectral Type	A0pe[a]
T_{eff}	9772K[a]
Luminosity	47 $L_\odot$[a]
Distance	144pc[a]
Mass	2.4$M_\odot$[a]
U	7.18±.08[b]mag
B	7.14±.04[b]mag
V	7.01±.04[b]mag
R	6.96±.05[b]mag
I	6.70±.09 [b]mag
J	5.99±.05[b]mag
H	5.28±.05[b]mag
K	4.37±.05[b]mag

[a]Stellar parameters from Monnier et al. [2006], Isella et al. [2006] and references therein.

[b]Photometry obtained at MDM Observatories in 2005 December.

Table 5.4. MWC275 disk properties from the literature.

Dust Disk		
Mass		0.0007$M_\odot$[a]
Dust to Gas Ratio		0.01
Surface Density Profile		r^{-1} [a,b]
Outer Radius		200 AU [b]
Inclination		48^o±2^o (this work, c)
Position Angle		136^o±2^o (this work, c)
Relative Mass Fractions	of μm and sub-μm grains	in the disk atmosphere[d]
0.1μm silicates	1.5μm silicates	PAH
$0.19^{+0.009}_{-0.018}$	$0.8^{+0.05}_{-0.04}$	$0.01^{+0.001}_{-0.001}$

[a]Natta et al. [2004]

[b]Isella et al. [2007]

[c]Wassell et al. [2006]

[d]van Boekel et al. [2005]

Table 5.5. AB Aur disk properties from the literature.

Dust Disk		
Mass		$0.0001 M_{\odot}$[a]
Dust to Gas Ratio		0.01
Surface Density Profile		r^{-1}[b]
Outer Radius		300 AU[a]
Inclination		$21^{o} \pm 0.5^{o}$[b]
Position Angle		$58.6^{o} \pm 0.5^{o}$[b]
Relative Mass Fractions	of μm and sub-μm grains	in the disk atmosphere[c]
0.1μm silicates	1.5μm silicates	PAH
$0.5^{+0.03}_{-0.03}$	$0.48^{+0.03}_{-0.04}$	$0.02^{+0.001}_{-0.002}$

[a]Lin et al. [2006]

[b]Corder et al. [2005]

[c]van Boekel et al. [2005]

thermal and hydrostatic equilibrium and can be divided into 3 distinct regions (Fig 1.18) -

- **Curved Inner Rim** Sufficiently close to the star (distance depends on stellar luminosity and dust sublimation temperatures), dust in the circumstellar disk reaches sublimation temperatures and evaporates. Inside of the evaporation radius, the disk is optically thin. The truncated dust disk is frontally illuminated by the star and forms a 'rim' whose shape depends sensitively on dust properties (Isella & Natta [2005]; Tannirkulam et al. [2007]). The rim puffs up, traps a significant fraction of stellar photons and re-radiates predominantly in the NIR (Dullemond et al. [2001]).
- **Shadow Region** The inner rim casts a geometric shadow on the region behind it (Dullemond et al. [2001]; Dullemond & Dominik [2004]), preventing it from receiving direct star light. The shadow is heated by scattered photons from the

rim edge and through diffusion. The size of the shadow depends on the rim geometry, mass of dust in the outer disk and dust grain properties in the outer disk.

- **Flared Disk** If sufficient dust is present in the outer disk, the disk eventually emerges from the shadow and "flares". The flared disk emits radiation in the MIR and longer wavelengths.

Details of the modeling procedure and comparison to data are described below.

5.3.1 The Monte Carlo Transfer Code - TORUS

The calculations in this chapter were performed using the TORUS Monte-Carlo radiative-transfer code (Harries [2000]; Harries et al. [2004]; Kurosawa et al. [2004], Chapter 2). Radiative equilibrium is computed using Lucy's (Lucy [1999]) algorithm on a two-dimensional, cylindrical adaptive-mesh grid. The initial density structure for the disk calculations is based on the canonical description of the α-disk developed by Shakura & Sunyaev [1973], viz

$$\rho(r,z) = \rho_0 \left(\frac{r}{r_0}\right)^{-\alpha} \exp\left[-\frac{1}{2}\frac{z^2}{h(r)^2}\right] \tag{5.1}$$

where r is the radial distance in the mid-plane, r_0 is some characteristic radius, z is the distance perpendicular to the mid-plane, and $h(r)$ is the scaleheight, given by

$$h(r) = h_0 \left(\frac{r}{r_0}\right)^{\beta} \tag{5.2}$$

with parameters of $\alpha = 2.125$ and $\beta = 1.125$, giving a radial dependence of the surface density of $\Sigma(r) \propto r^{-1.0}$. Once the temperature (we assume that the disk is in local thermodynamic equilibrium passively heated by the star, and gas and

dust are thermally coupled) and dust sublimation (see next paragraph) structures have converged using the Lucy algorithm, the vertical disk structure is modified via the equation of hydrostatic equilibrium following a similar algorithm to that detailed by Walker et al. [2004]. A self-consistent calculation for dust sublimation and disk temperature followed by a hydrostatic equilibrium calculation is repeated until the disk density structure has converged. Convergence is typically achieved in four iterations. Images and SEDs are subsequently calculated using a separate Monte Carlo algorithm based on the dust emissivities and opacities (Harries [2000]). The shape of the dust evaporation front is computed following Chapter 2.

We use Kurucz (Kurucz [1970]) stellar atmosphere models as input spectra for the stars. We consider a mixture of 0.1, 1.3 and 50 micron warm silicates (Ossenkopf et al. [1992]) and power-law opacity mm grains (Mannings & Sargent [1997]; Natta et al. [2004]) to model the opacity in the disk. The micron and sub-micron grain mixture is based on work by Meeus et al. [2001] and van Boekel et al. [2005]. To keep the analysis simple, the grain species are assumed to be well mixed with gas (Kamp & Dullemond [2004]) following a delta function size distribution. Dust scattering is not included in the models. Scattering does not seem to have significant impact on disk structure and interpretation of infrared interferometry for HAe stars (Dullemond & Natta [2003]; Pinte et al. [2008]).

During the course of our modeling and as outlined in Chapter 3, we realized that an additional emission component (Fig 1.18) which we argue to be gas (§5.4.1), is needed inside the dust destruction radius to explain the NIR SED and interferometry of MWC275 and AB Aur. This additional component is not treated self consistently

in our modeling and is added after the dust-opacity-dominated circumstellar-disk model converges in structure. Calculations by Muzerolle et al. [2004] have shown that for parameters suitable to MWC275 and AB Aur, gas does not significantly alter the structure of the dust rim, justifying our simple treatment for the NIR emission geometry.

5.3.2 Comprehensive models for SED and Interferometry

To fit the SED and visibilities of MWC275 and AB Aur we adopted the following algorithm: First, we computed models for the dust evaporation front as described in §5.3.1. The inner edge of the dust disk is assumed to be dominated by grains larger than 1 micron (Tuthill et al. [2001]; Isella et al. [2006]) and the evaporation front shape is set by the density dependence of dust sublimation temperatures (Isella & Natta [2005]; Tannirkulam et al. [2007]). The K-band visibilities are computed for the model and compared with data. The normalization of the dust evaporation law is then adjusted so that the model visibilities fit the visibility data before the first visibility minimum. These models fail to fit the visibility beyond the minimum and do not have sufficient emission to explain the observed NIR SED. Therefore an additional emission component has been added inside the dust sublimation radius to reconcile the model with the visibility data and NIR SED.

With the inner-rim parameters fixed, we next focus on MIR and the mm disk. Millimeter interferometry results from the literature are used to fix disk masses and sizes. The majority of the dust mass is placed in mm sized grains with a power-law opacity function (Natta et al. [2004]). A small fraction ($\sim$10%) of the dust mass is

in micron and sub-micron (small) grains with their relative mass fractions based on literature results (Meeus et al. [2001]; van Boekel et al. [2005]). The physical extent of small grains is constrained with MIR imaging and interferometry. The model is then allowed to run to convergence. The model SED is compared with MIR and far-infrared data, the mass of the small grain population is then adjusted and models are recomputed until a good fit to the MIR and far-infrared SED is obtained.

The MIR visibilities are computed for the SED-converged model and compared with the data and the spatial distribution of the small grain component is adjusted until model visibilities match with data. The only free parameters in our models are the absolute masses of the small grains, the mass of the 50μm silicate grain and their spatial distribution. Each of the models is computationally expensive. To achieve fast convergence, the parameter space was varied by hand, until a good fit was found for the observable quantities.

5.4 MWC275: Analysis

MWC275 is a Herbig Ae star (refer to Table 5.2 for basic properties and photometry) with a total luminosity of 36$L_\odot$. The large stellar luminosity, coupled with the fact that the mass accretion rate is $\leq 10^{-7} M_\odot$/year (Garcia Lopez et al. [2006]) allows us to ignore accretion heating and model the MWC275 circumstellar disk as a passive disk, reprocessing stellar radiation (Chiang & Goldreich [1997]; Dullemond et al. [2001]). For our models, we choose the MWC275 disk mass to be between 0.05-0.1 $M_\odot$ (Natta et al. [2004]) and a surface density profile that varies radially as r^{-1} (Isella et al. [2007]). The disk outer edge is truncated at 200AU and bulk ($\sim$80%) of the

dust mass is assumed to reside in mm grains having an opacity with a wavelength dependence of λ^{-1} at long wavelengths. Here, we describe in detail our modeling results for the NIR and MIR morphology of MWC275.

5.4.1 The Thermal NIR Disk

Visibilities

Like many other Herbig Ae stars, MWC275 shows a strong NIR excess over stellar photospheric values (Hillenbrand et al. [1992]). This excess has been traditionally interpreted in terms of the dust disk being truncated by sublimation and forming a 'rim'. The rim intercepts stellar photons, re-radiatiing predominantly in the NIR (Dullemond et al. [2001]; Isella & Natta [2005]; Tannirkulam et al. [2007]). However, in Chapter 3 we had conclusively shown that models in which all of the NIR excess arises from dust rims alone cannot explain the CHARA interferometry data on MWC275. Our arguments in Chapter 3 were brief. We present a more elaborate analysis in this section.

MWC275 observations allow us to clearly detect the asymmetry of the MWC275 disk (see Appendix C), as having inclination=$48^o \pm 2^o$, PA=$136^o \pm 2^o$, consistent with the inclination of 51^{+11}_{-9} degrees, PA of $139^o \pm 15^o$ determined in Wassell et al. [2006] and inclination of $46^o \pm 4^o$, PA of $128^o \pm 4^o$ determined in Isella et al. [2007]. The complete visibility data along each of the baselines are presented in Fig 5.2. Following Chapter 3, we show the data in a concise manner in Fig 5.3 using the notion of an "effective baseline" -

$$B_{eff} = B_{projected}\sqrt{\cos^2(\theta) + \cos^2(\phi)\sin^2(\theta)}$$

where θ is the angle between the uv vector for the observation and the major axis of the disk and ϕ is the inclination of the disk. Under the flat disk assumption, the effective baseline correctly accounts for the change in resolution due to the disk inclination and PA (the geometry of thick disks is represented only approximately with optical depth effects and 3-D geometry of thick disks not being taken into account), allowing us to plot the visibility measurements as a function of one coordinate, simplifying presentation and analysis.

We attempt at fitting the visibilities with a curved inner-rim model (the "standard" model) where the rim curvature (variation in cylindrical radius between rim midplane and the atmosphere) is set by the density dependence of dust sublimation temperatures, taken from Pollack et al. [1994]. In this model, silicate grains sublimate at a higher temperature compared to other grains and hence fix the rim location. The rim is assumed to be composed of 1.3μm grains, as larger grains do not affect the rim shape and location significantly (Isella & Natta [2005]), at the same time making numerical convergence slower due to strong back-warming effects (Isella & Natta [2005]; Tannirkulam et al. [2007]). For silicate dust, the evaporation temperature $T_{\rm evp}$ can be parameterized as

$$T_{\rm evp} = G \left[\frac{\rho_{\rm gas}(r,z)}{1{\rm g\ cm^{-3}}} \right]^{\gamma} \tag{5.3}$$

where $G = 2000K$, $\gamma = 1.95 \times 10^{-2}$ and $\rho_{\rm gas}$ is the density of gas in gcm^{-3} (see IN05 eq. [16]). This parameterization, derived from a fit to sublimation temperatures recorded in the laboratory (Pollack et al. [1994]), produces a dust rim with an inner edge at 0.36 AU (Fig 5.4a). The rim radius is too large to fit even the relatively

short baseline visibility data from IOTA (Figs 5.2 and 5.3). In order to fit the data before the first visibility minimum, we had to increase the T_{evp} normalization-G by $\sim$30% from 2000K to 2600K. This increases the sublimation temperature at the base of the rim from $\sim$1350K to $\sim$1800K (for physical implications refer §5.6). Fig 5.4b shows the synthetic K-band image for the rim with the increased normalization. The dashed line in Fig 5.2 traces the visibility for this model and provides a good fit to the short baseline ($<$ 100m) data.

However, as already demonstrated in Chapter 3, rim models which are sharply truncated due to dust sublimation and produce all of the NIR excess, fail to fit observations beyond the first visibility minimum. These models display bounces in visibility at long baselines (not seen in the data) because of the presence of sharp ring-like features with high spatial frequency components in the corresponding images, even for the smoothest rims physically plausible. In Chapter 3, we showed that the presence of a smooth emission component inside the dust destruction radius (Fig 5.4c) providing 56% of the total K band emission helps fit the data well (solid line in Figs 5.2 and 5.3). The NIR visibility data cannot constrain the surface brightness profile of the smooth emission component (we have adopted a constant surface brightness profile - a Uniform Disk for simplicity), but can constrain the size scale of the emission fairly robustly. Fig 5.5 shows a series of visibility curves where the smooth emission component is fixed to be 56% of the total emission and the radius of the Uniform Disk component is decreased by 15% successively from the initial radius of 0.23AU radius. The model image is then rescaled to maintain a good visibility fit at baselines shorter than 100m. It can be seen in Fig 5.5 that for Uniform Disk (UD) radii smaller than

0.19AU, the model visibilities begin to deviate significantly from the observations. Thus, the CHARA data constrains the smooth emission component to be on the same length scale as the dust sublimation rim filling the region between the disk and the central star.

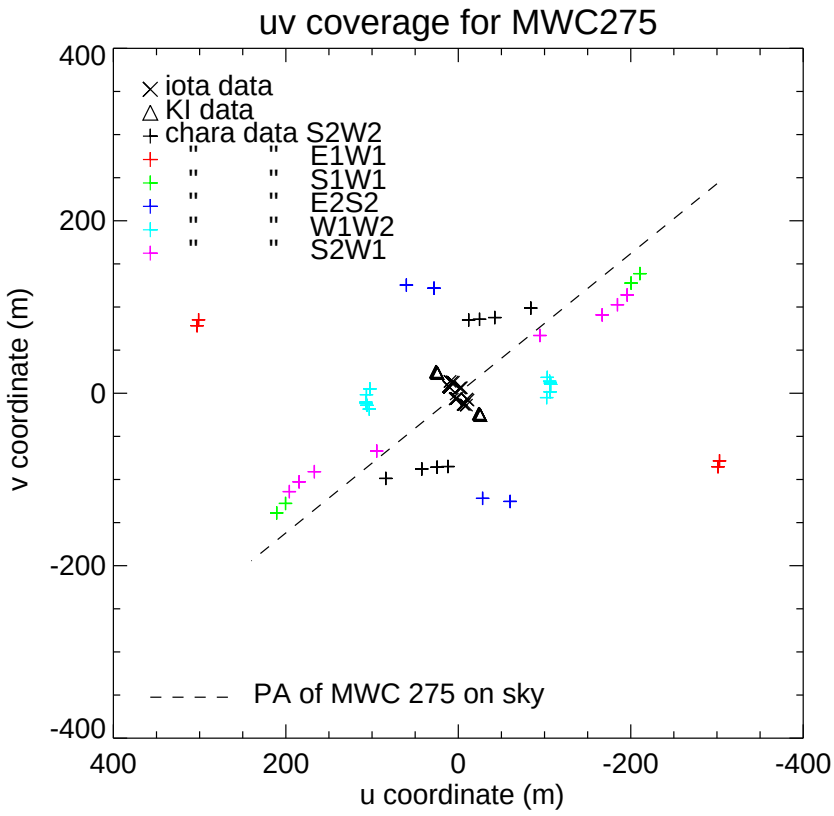

Figure 5.1 uv coverage for MWC275. We include data from KI (Monnier et al. [2005]), IOTA (Monnier et al. [2006]) and CHARA (Tannirkulam et al. [2008]) in our analysis. A position angle (measured East of North) of 136^o for MWC275 is marked in the left panel.

SED

Fig 5.6 shows the NIR SED for MWC275. Besides failing to explain the NIR interferometry, the standard model also fails at producing sufficient NIR emission to explain the MWC275 SED even in its 'low' state. In Chapter 3, we had shown that

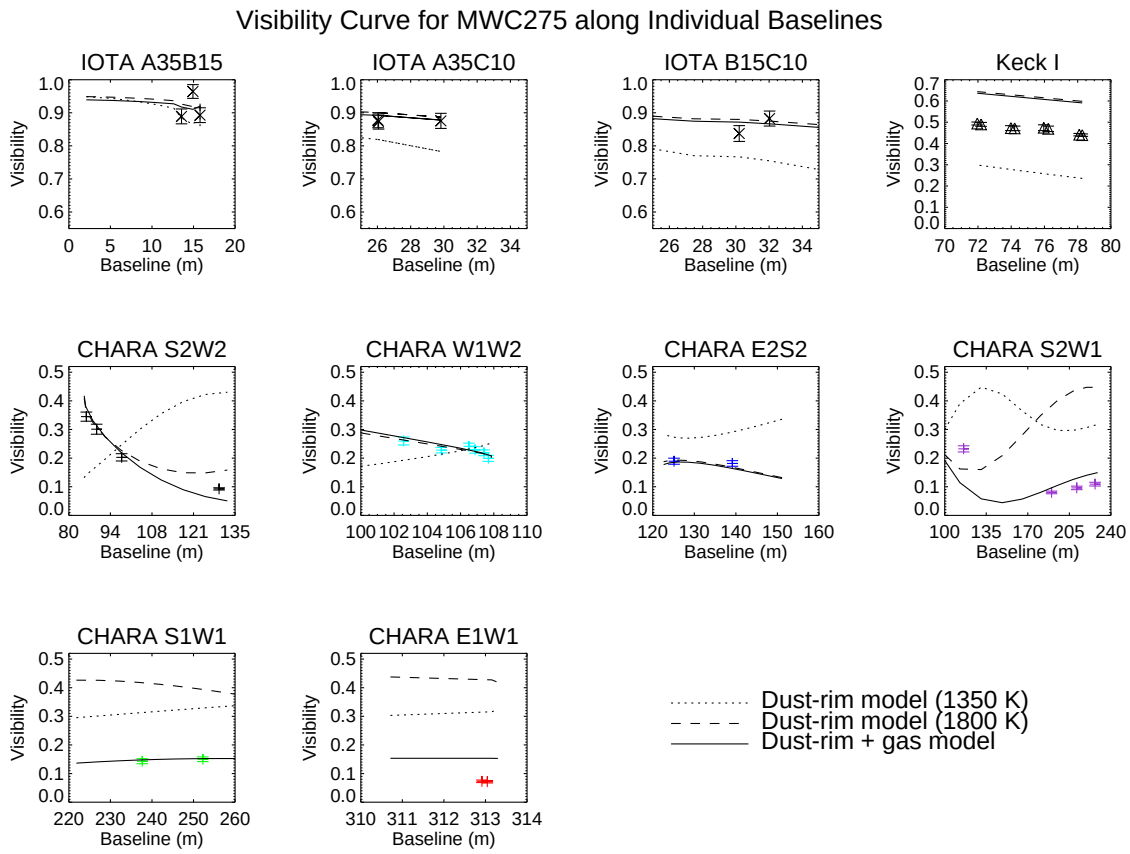

Figure 5.2 MWC 275 visibility data and model curves. The quoted model temperatures are at the base of the dust rim. The NIR size deduced from the Keck Interferometer data (triangles) is ∼20% larger than the size obtained with the CHARA data. This variability of MWC275 is discussed in §5.4.1.

binarity and source variability cannot account for the discrepancy between the standard model and data. We had argued that the presence of smooth emission inside the dust destruction radius can help explain the NIR visibility and account for the "missing" NIR flux in standard models. Opacity candidates for the smooth emission component are: (1) a dusty spherical halo around the stars (Vinkovic et al. [2006]) and (2) gas inside the evaporation front. However, to fit the visibility data, the halo emission would have to be closer to the star than the dust destruction radius in

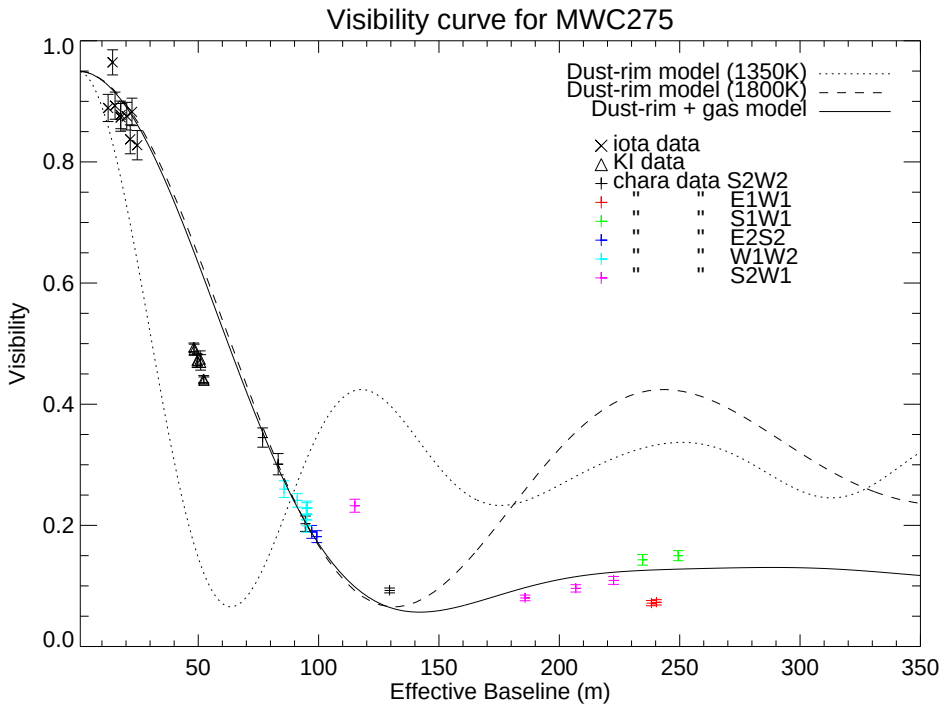

Figure 5.3 MWC275 visibility vs 'Effective Baseline'. Effective Baselines are useful in presenting data along multiple uv vectors in a concise manner (under the assumption of axial symmetry). The NIR size deduced from the Keck Interferometer data (triangles) is ∼20% larger than the size obtained with the CHARA data. This variability of MWC275 is discussed in §5.4.1

the disk. This would require even higher dust-sublimation temperatures than the ∼ 1850K we are adopting.

The most plausible physical mechanism for the smooth emission is hot gas. The required emission levels to explain the long-baseline K-band visibility data can be obtained with optically thin gas ($\tau \sim 0.15$) with a temperature range of 2000K-3000K (Muzerolle et al. [2004]; Eisner [2007]). Assuming that the gas has sufficient opacity to produce the difference in flux between the standard model and the observed photometry, we can place limits on the wavelength dependence of gas opacity. Fig 5.7 plots limits on the gas opacity (normalized at K band) such that flux from the gas component + the standard model falls within 10% of the observed photometry (we

have assumed that gas does not significantly alter the geometry of the dust rim). In the next 2 paragraphs we compare theoretical gas-opacity curves with our empirically derived opacity from SED.

Fig. 5.7 shows the wavelength dependence of molecular (Ferguson et al. [2005]; Zhu et al. [2007]) and free-free+free-bound (henceforth FF-BF) opacity, both good candidates for the gas emission (refer Chapter 3). At 5000K, FF-BF opacity (Ferguson et al. [2005]) agrees well with the derived opacity at long wavelengths but overshoots limits shortward of 2μm. At temperatures greater than 8000K , FF-BF opacities rise quickly with wavelength producing excessive mid-infrared light.

Theoretical molecular opacities compare fairly with empirical derivation between 1μm and 4μm. Beyond 4μm , theoretical molecular opacities rise rapidly with wavelength. However, the observed SED can be matched with models only if the gas opacity is flat between 4μm and 9μm. Also at 2000K and 2500K, strong opacity bands of CO and water vapor are present at 2.5μm and 5μm respectively, which have not been observed in MWC275. This suggests that if molecules were contributing to the bulk of NIR opacity, then some of the species providing opacity between 4-8 μm in Ferguson et al. [2005] and Zhu et al. [2007] are being destroyed in the vicinity of Herbig Ae star MWC275.

Sitko et al. [2008] have obtained fairly dense time coverage on the NIR and MIR SED of MWC275. The NIR SED shows variability at the 20% level. During the same period, the flux in the visible shows no detectable change, indicating that that stellar luminosity remained fairly constant. Sitko et al. [2008] interpret their observations as variations in the structure of the thermal NIR disk. A variation in

the NIR morphology of MWC275 was also detected in the interferometry. The NIR disk size deduced from the Keck Interferometer data (April 2003 epoch, Figs 5.2 and 5.3) is ∼20% larger than the size obtained with the CHARA data (June 2004-Aug 2006 epochs). The size determined from the S2W1 June2007 data also differs at the ∼25% level from the size obtained from earlier CHARA epochs. These variations are poorly understood and could be caused by changes in size/geometry, mass accretion rate and gas content in the inner disk.

5.4.2 MIR SED and Emission Morphology

van Boekel et al. [2005] analyzed the MIR SED (Fig 5.8) of MWC275 in detail and showed that the SED could be reproduced well with a grain mixture of 1.5μm and 0.1μm silicates with mass ratio of 4:1. We use results from van Boekel et al. [2005] in fixing the small grain composition in our disk models.

As seen in Fig 5.8, the MWC275 SED falls sharply between 20μm and 30μm. This drop and the 10μm silicate feature can be simultaneously reproduced only if the mass fraction of the small grain dust component relative to gas beyond 7AU is less than 20% of the mass fraction inside of 7AU (physical implication discussed in §5.6). If the small grain component is allowed to exist beyond 7AU, then the model far-infrared spectrum becomes much stronger than observed the SED. Fig 5.8 shows a TORUS model SED that fits the MIR and longer wavelength spectrum of MWC275 well. In this model, 40% of the 8μm emission arises from the dust rim, with the rim contribution declining to ∼20% at 13μm. This model also fits the MIDI-VLTI MIR visibilities (Leinert et al. [2004]) and reproduces the 0.8±0.1AU 11μm FWHM minor-

Table 5.6. MWC275 model-disk properties constrained by this work.

Dust Disk	
Inner Radius	0.22 AU[a]
K-band flux contribution from dust rim	29% [a]
Mass fractions of dust components	see Fig 5.10
NIR Gas Disk	
Surface Brightness Profile	constant (poorly constrained)
Outer Radius	0.22 AU [a]
K-band flux contribution	56% [a]
Temperature	> 1800K
Vertical Optical Depth	0.15 [a]
Gas-Opacity Profile	see Fig 5.7

[a]Chapter 3. The star contributes 10% of the K-band flux and an extended envelope (Monnier et al. [2006]) contributes 5%.

axis size of MWC275 (Fig 5.9), naturally explaining why MWC275 is unresolved by the Keck Segment Tilting Experiment. The quality of SED and 'visibility fit in the 8-15μm region is only moderate, probably due to the simple dust composition and distribution that we have assumed in the model. The initial model setup has been chosen to reproduce MWC275 mm-interferometry.

Table 5.6 lists disk parameters for the MWC275 model and Fig 5.10 shows the radial distribution of the small grain fractions. The mid-plane temperature profile and the "flaring" geometry of the disk surface are shown in Fig 5.11. The dust rim "shadows" (Dullemond et al. [2001]; Dullemond & Dominik [2004]) the region of the disk between 0.3 and 1AU beyond which the disk begins to flare. The τ=1 surface drops down in scale height steeply after 6.5AU where the small grain fraction reduces sharply.

5.5 AB Aur: Analysis

AB Aur is a Herbig Ae star (refer to Table 5.3 for basic properties and photometry) with a total luminosity of $47L_{\odot}$ (Isella et al. [2006]). As in the case of MWC275, AB Aur's large stellar luminosity dominates the circumstellar disk's energy budget Garcia Lopez et al. [2006, accretion rates $\leq 10^{-7}M_{\odot}$/year]. This allows us to ignore accretion heating and model the AB Aur circumstellar disk as a passive disk, reprocessing stellar radiation (Chiang & Goldreich [1997]; Dullemond et al. [2001]). For our models, we choose the AB Aur disk mass to be between 0.007-0.013 $M_{\odot}$ (Lin et al. [2006]) and a surface density profile that falls radially as r^{-1} (Corder et al. [2005]). The disk outer edge is truncated at 300AU and the bulk ($\sim$80%) of the dust mass is assumed to reside in mm grains with an opacity that depends on wavelength as λ^{-1} for long wavelenghts. Here, we describe in detail our modeling results for the NIR and MIR morphology, and SED of AB Aur.

5.5.1 The Thermal NIR Disk

We follow the procedure outlined in §5.4.1 to model the SED and visibilities of AB Aur. We first attempt at fitting a standard curved dust rim model (Fig 5.14) to the NIR visibilities. The rim is assumed to be composed of 1.3μm silicate grains and the dust evaporation temperature law is described by equation (5.3). This produces rim radii too large to fit baselines shorter than 100m and we had to increase the T_{evp} normalization to 2800K from 2000K. This increases the sublimation temperature at the base of the rim from $\sim$1350K to $\sim$1950K. The dashed line in Fig 5.13 traces the visibility for this model and provides a good fit to the data at baselines shorter than

Table 5.7. AB Aur model-disk properties constrained by this work.

Dust Disk	
Inner Radius	0.24 AU [a]
K-band flux contribution from dust rim	22% [a]
Mass fractions of dust components	refer Fig 5.10
NIR Gas Disk	
Surface Brightness Profile	constant (poorly constrained)
Outer Radius	0.24 AU [a]
K-band flux contribution	65%
Temperature	> 1900K
Vertical Optical Depth	0.14 [a]
Gas-Opacity Profile	refer Fig 5.7

[a]Chapter 3. The star contributes 8% of the K-band flux and an extended envelope (Monnier et al. [2006]) contributes 5%.

100m.

The dust-rim-only model produces large bounces in visibility beyond 150m and as in the case of MWC275, this bounce is not observed. We have scanned the 150m-300m baseline (Fig 5.13) range several times with CHARA and have failed to detect fringes, ruling out dust-rim only models for the AB Aur NIR emission. The addition of a Uniform Disk of emission interior to the dust destruction radius (Fig 5.14c) helps fit the data well (solid line in Fig 5.13). The gas component also helps fit the NIR SED (Fig 5.15). Parameters for the 'dust rim + Uniform Disk' model are listed in Table 5.7.

5.5.2 MIR SED and Emission Morphology

Liu et al. [2007] resolved the AB Aur disk at 10.3μm using nulling interferometry and measured a disk is inclination of 45^o- 65^o inconsistent with nearly face on measurements in the mm (Corder et al. [2005]) and the NIR (Millan-Gabet et al. [2001];

Eisner et al. [2004]). Liu et al. [2007] interpreted their result in terms of the AB Aur circumstellar environment being more complicated than a disk. Since AB Aur is well resolved by the Keck Segment Tilting Experiment (Fig 5.17), a disk inclination of 45^o- 65^o would have produced observable size difference between the major and minor axis of the disk. We do not find evidence for this size variation in our Segment Tilting data, and hence support a face on model for the mid-infrared disk around AB Aur consistent with the NIR and mm results.

The MIR spectrum of AB Aur in the 10.7μm to 20μm range can be modeled well with a dust grain mixture of 1.3μm and 0.1μm silicates with equal mass fractions (van Boekel et al. [2005]). In addition to the micron and sub-micron silicates, we include a 50μm silicate component to model the relatively flat spectrum of AB Aur between 35μm and 80μm .

Fig 5.16 shows a TORUS model SED that fits the MIR and longer wavelength spectrum of AB Aur well. In this model, $\sim$40% of the 8μm emission arises from the dust rim, with the rim contribution declining to $\sim$10% at 13μm. This model also fits the Keck Segment Tilting data visibilities reproducing the 10.5$\pm$0.7AU 10μm FWHM size of AB Aur (Fig 5.17). By initial design, the model fits AB Aur mm-interferometry and SED.

Table 5.7 lists disk parameters for the AB Aur model and Fig 5.10 shows the radial distribution of the small grain fractions. The mid-plane temperature profile and the τ=1 surface at 5500Å are shown in Fig 5.11. The inner rim shadows the disk between 0.3AU and 1AU, beyond which the disk surface takes a flared geometry.

5.6 Discussion

The simultaneous modeling of the infrared and millimeter SED and interferometry of MWC275 and AB Aur allows us to address several important issues regarding the structure of their circumstellar disks. To maintain clarity in our discussion we divide the disk into two regions (i) thermal NIR region (< 0.3 AU) (ii) outer disk (between 0.3AU and the disk outer edge).

5.6.1 The Thermal NIR Disk

Detailed modeling (§5.4.1 and §5.5.1) of the inner disk shows that models where the bulk of the NIR emission arises in a dust rim truncated by sublimation fail to fit the long-baseline interferometry data and under-estimate the NIR emission by a factor of 2 relative to observations. As mentioned in Chapter 3 and demonstrated in detail here, the presence of a gas emission component inside the dust destruction radius can solve the interferometry and SED problem simultaneously.

This however opens up a number of new questions, namely (i) What is the geometry of the gas-dust transition region? To date there has been no calculation of transition region structure that treats both gas and dust simultaneously in a self consistent manner. (ii) What are the relative contributions of accretion and stellar radiation to heating the gas? We have shown that an ad-hoc addition of an NIR emission component inside the dust destruction radius helps explain the data, but the current modeling does not shed any light on the energy budget question. (iii) What are the gas species that provide the NIR opacity? Is the opacity molecular in nature or is it from free-free and free-bound processes? If a significant portion of

the NIR emission were indeed arising from molecular gas, then Fig 5.7 shows that theoretical gas opacities depend much more sensitively on wavelength between 4 and 10μm than what is observed. This suggests that some of the molecules providing the model opacities might be getting destroyed by the stellar UV radiation field.

In the course of modeling the MWC275 and AB Aur disks, we realized (§5.4.1) that the observed K-band sizes could be reproduced only if the dust sublimation temperature at the base of the dust rims were increased to ∼1850K from the experimentally measured silicate evaporation temperatures of ∼1400K (Pollack et al. [1994]). A simple treatment of the gas-dust transition region by Muzerolle et al. [2004] suggests that gas is not effective in modifying rim geometry. In the absence of shielding by gas, the large dust sublimation temperatures indicate that the grains in the inner disks of young stars are significantly more refractory and/or optically transparent than has been assumed in the literature. There is also the possibility that the gas gets optically thick along the mid-plane, shielding the dust from direct stellar radiation and allowing the dust rim to exist closer to the star (Monnier et al. [2005]; Vinkovic [2006]; Isella et al. [2006]). Future, high resolution NIR spectroscopic studies of MWC275 and AB Aur, combined with self consistent models of the gas density and temperature structure, will help address many of the questions raised here.

MWC275 and AB Aur require gas emission to explain the their SED interferometry. In contrast, past modeling work by Isella et al. [2006] seems to suggest that dust rims alone are probably sufficient to explain the NIR data on the young stars V1295 Aql (A2 IVe) and CQ Tau (F2 IVe). A larger sample of young stars will therefore

have to be observed with milli-arcsecond interferometry to establish and understand trends between spectral type, stellar mass, accretion rates and the contribution of gas emission to NIR SED.

A new and exciting observational domain will be opened with the commissioning of the fringe tracker (Berger et al. [2006]) for CHARA-MIRC (Monnieret al. [2007]) in the summer of 2008. This will sufficiently improve CHARA-MIRC sensitivities to combine light from 3 or more telescopes, allowing the first milli-arcsecond non-parametric imaging of MWC275 and AB Aur in the NIR. The snapshot multiple-baseline coverage will provide us a powerful tool in understanding the infrared time variability of YSO disks.

5.6.2 The Outer Disk

Our models for the MWC275 and AB Aur MIR interferometry and SED suggest that the outer disks of these systems are at different evolutionary stages. MWC275 10 micron size and MIR SED can only be reproduced if the disk is depleted in micron and sub-micron sized grains beyond ∼7AU (§5.4.2). This meshes well with the fact that the observed 10.7μm size of MWC275 is ∼3 times smaller than AB Aur. The depletion of small grains beyond 7AU in the disk atmosphere indicates that the dust particles in MWC275 have undergone significant settling. However, the presence of the 10μm silicate feature in MWC275 implies that there is some process (like planetesimal collisions) that maintains the supply of micron sized grains in the inner regions of the disk.

Our models predict that the inner dust rim shadows (Dullemond & Dominik

[2004]) the region of the disk between 0.3AU and 1AU. The structure and size of the shadow depends sensitively on the composition of grains in the circumstellar disk (Tannirkulam et al. [2007]) and hence is an important probe of dust physics. The presence of the shadow has not been observationally confirmed yet in any YSO system, although some indirect evidence has been found in VV Ser (Pontoppidan et al. [2007]).

5.7 Conclusions

We have presented the first set of comprehensive disk models for the SED and interferometry of Herbig Ae stars MWC275 and AB Aur. We have shown that 'standard' models for the dust evaporation front where the bulk of the near-infrared emission arises from a dust wall, fail to explain the near-infrared spectral energy distribution and interferometry. Standard models produce large bounces in visibility at high spatial frequency, which is not observed in the data. We have conclusively demonstrated that the presence of an additional smooth emission component (presumably hot gas) inside the dust destruction radius and on a similar size scale to the dust rim can ameliorate the situation. In the absence of shielding of star light by gas, we have established that dust grains in the gas-dust transition region will have to be highly refractory, sublimating at 1850K. The small mid-infrared size of MWC275 relative to AB Aur, shows that the dust grains in the outer disk MWC275 are significantly more evolved/settled than the grains in the AB Aur disk. We suggest that dynamical processes (like planetesimal collisions) that maintain the population of micron-sized grains producing the 10μm feature in the spectrum, are operational only in the inner

$\sim$7AU of MWC275. However, in AB-Aur the small-dust producing mechanisms exist at least out to $\sim$20 AU and maybe even beyond.

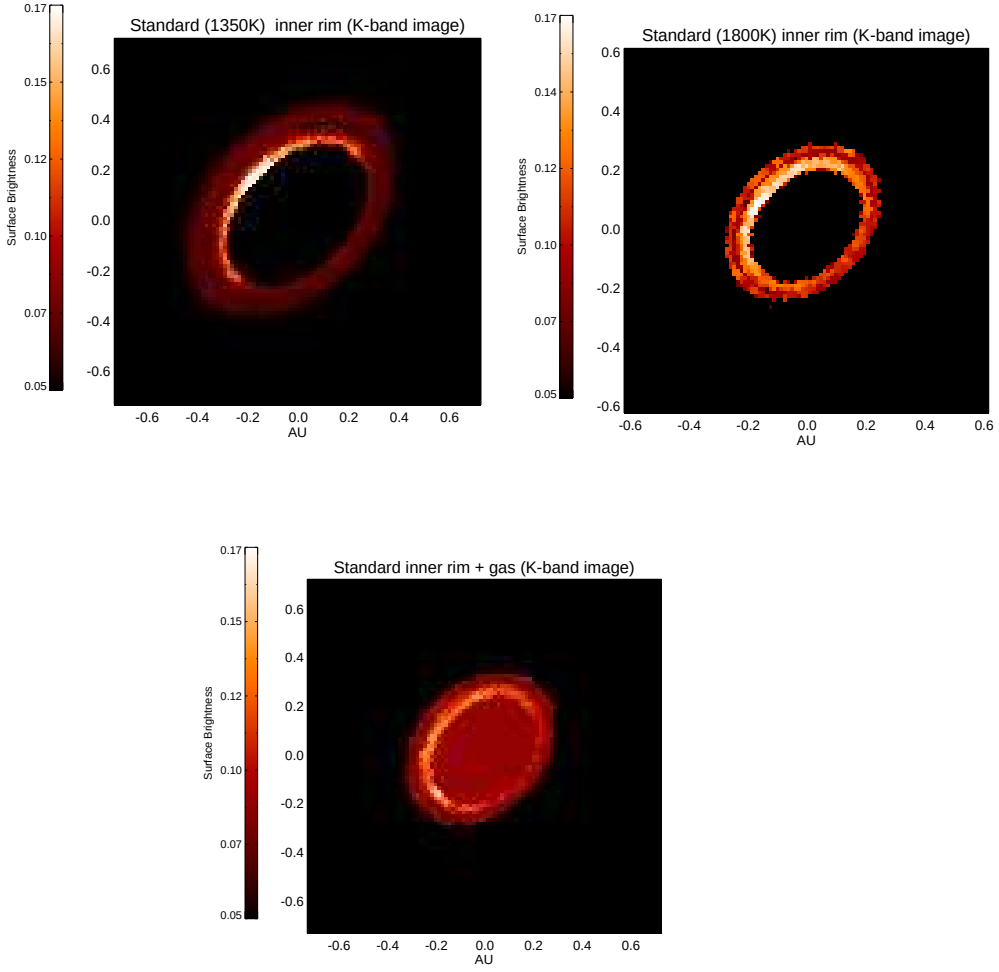

Figure 5.4 Inclined-disk models for NIR emission in MWC275. The disk has an inclination of 48^o and a PA of 136^o (North is towards the top and East is on the left). The sense of the inclination is from Grady et al. [1999] a) Top left panel. A standard curved dust-rim-only model with rim-base temperature ∼1350K. b) Top right panel. Standard curved dust-rim-only model with rim-base temperature ∼1800K. c) Bottom panel. Curved dust-rim model with gas emission (modeled as a uniform disk centered on the star) inside the dust rim to smooth out the emission profile.

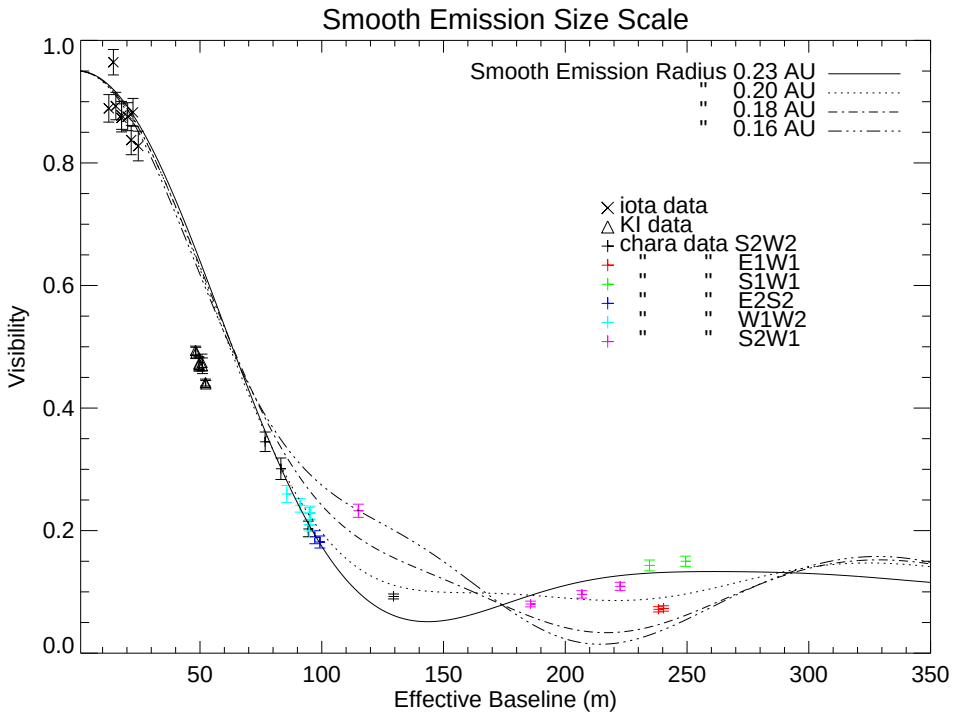

Figure 5.5 Constraining the size of the smooth emission component in MWC275. The model visibilities begin to deviate significantly from the data when the radius of the smooth emission component becomes smaller than 0.19 AU.

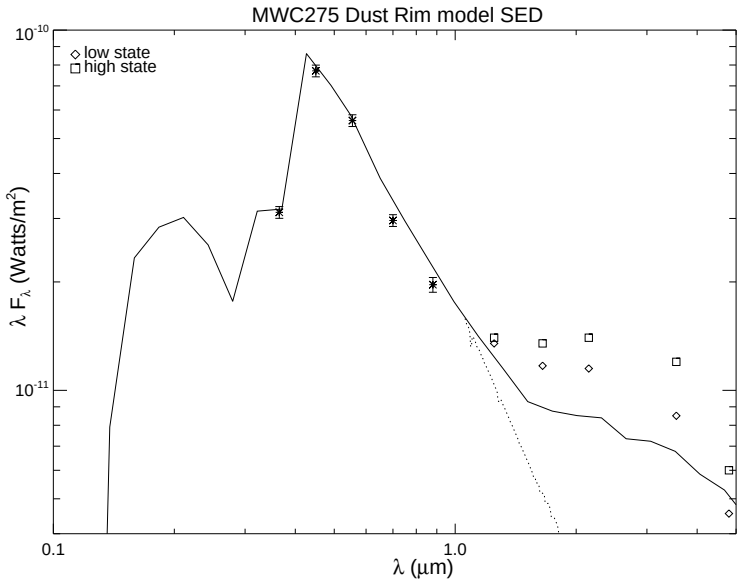

Figure 5.6 The NIR SED for MWC275. The 'stars' are photometry points from MDM (Appendix Table B.2). The 'squares' and 'diamonds' are high and low state measurements from Sitko et al. [2008]. The solid line is the SED produced by the 'star + dust-rim only' model in Fig 5.4b. The dotted line is the SED of the star.

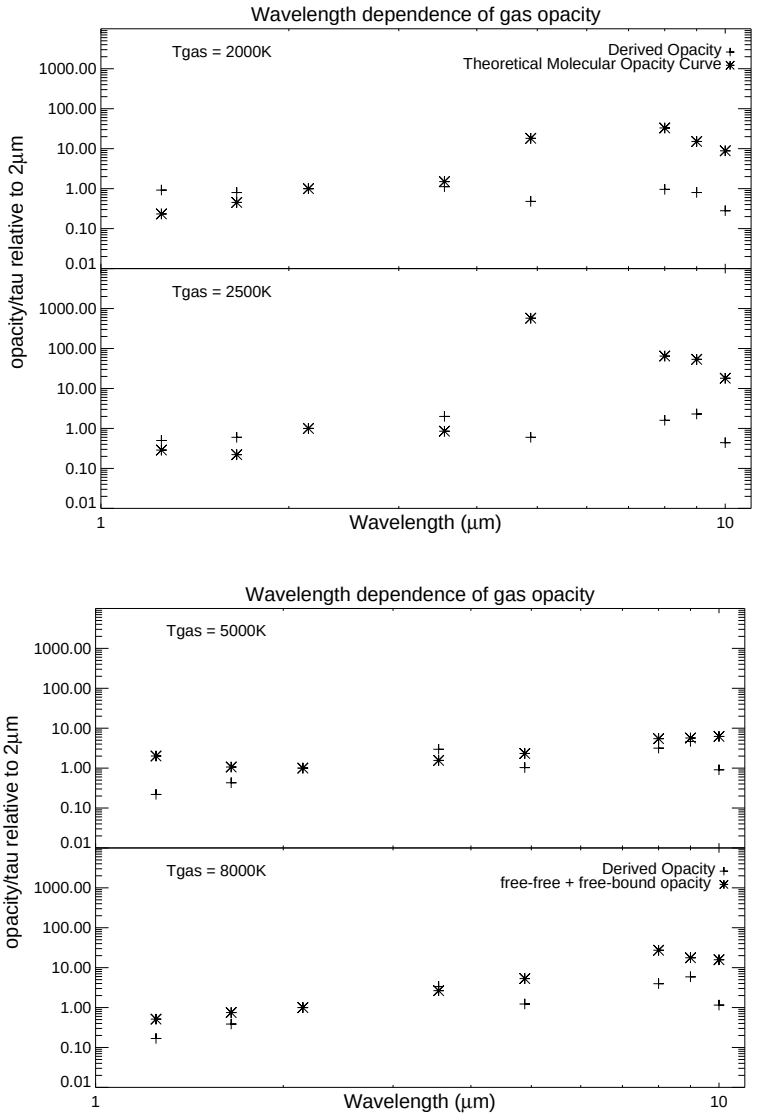

Figure 5.7 Gas opacity. The plusses (+) represent empirically derived gas opacities from observed photometry and NIR disk models for MWC275 (see Fig 5.4). a) Top panel. The stars represent fiducial theoretical molecular absorption opacities smoothed over the photometry band for 2000K and 2500K gas respectively (Zhu et al. [2007]). The opacity jump at 5μm is due to water vapor. b) Bottom Panel. The gas absorption opacity at infrared wavelengths is dominated by free-free and free-bound transitions of H^- at 5000K and by hydrogen at 8000K (Ferguson et al. [2005]; Zhu et al. [2007]).

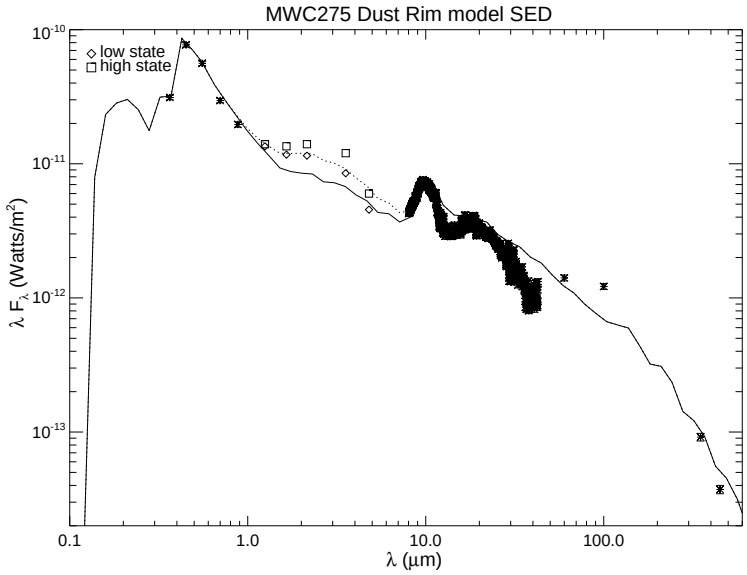

Figure 5.8 MWC275 SED from UV to mm.The mid, far-infrared and sub-mm data are from Meeus et al. [2001] and references therein. The solid line traces the dust-disk model SED (see §5.4.2). The dotted line traces the dust-disk+smooth emission SED. The smooth component is modeled as optically-thin grey emission at 2500K. The relative contributions of star, dust and gas to the total integrated flux are 0.79, 0.16 and 0.05 respectively.

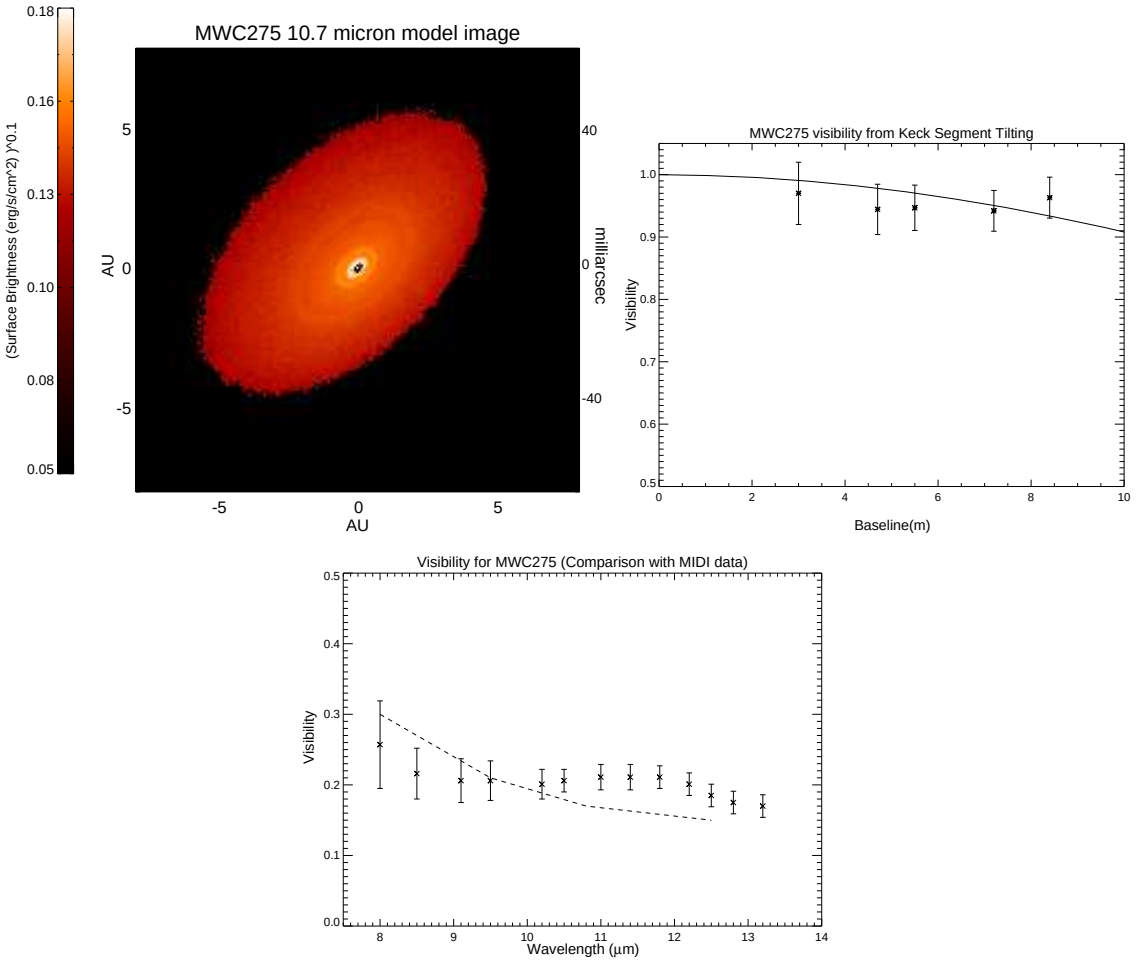

Figure 5.9 MIR image and visibilities for MWC275. The disk has an inclination of 48^o and a PA of 136^o (North is towards the top and East is on the left) a) Top panel. Synthetic 11μm TORUS image. b) Middle panel. Azimuthally averaged 10.7μm visibilities from the Keck Segment Tilting Experiment (Monnier et al. [2008b]). The 'stars' are measured values and the solid line is the model visibility. MWC275 is not resolved by Keck. c) Bottom panel. Model visibilities compared with MIDI (Leinert et al. [2004]) data. The MIDI data was obtained at a projected baseline of $\sim$ 99m and a PA of 16^o, nearly aligned with disk minor axis.

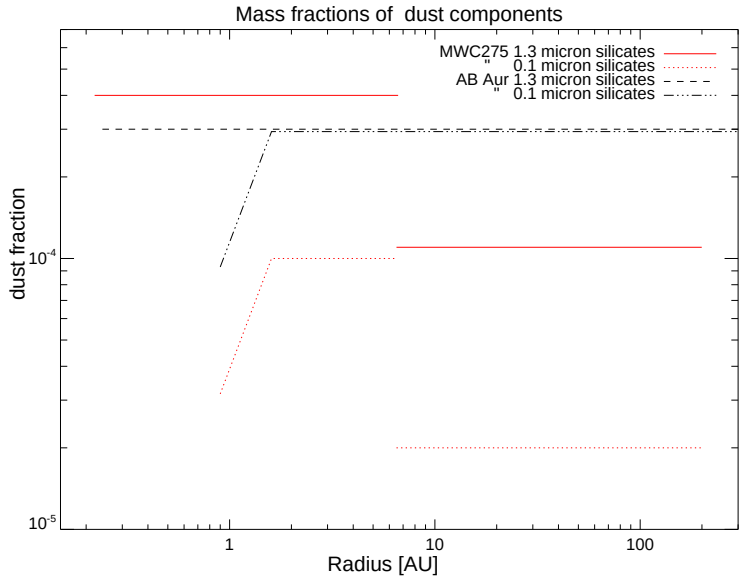

Figure 5.10 Mass fractions of dust components relative to gas. The micron and sub-micron grain fraction in MWC275 (red solid and dotted lines) have to be reduced below 20% of their values inside of 6.5AU at larger radii to fit the SED and interferometry. The silicate-grain opacities are from Ossenkopf et al. [1992] and the relative masses of dust grains are from van Boekel et al. [2005]. Between 0.9AU and 1.6 AU, 0.1μm grains are added smoothly to avoid the formation of two distinct dust rims.
The bulk of the dust mass is in mm sized grains with a power law opacity profile (Natta et al. [2004]). For AB Aur, we also add a 50μm silicate component to improve SED fits between 40μm and 100mum. The dust parameters are derived assuming gas and dust are well mixed.

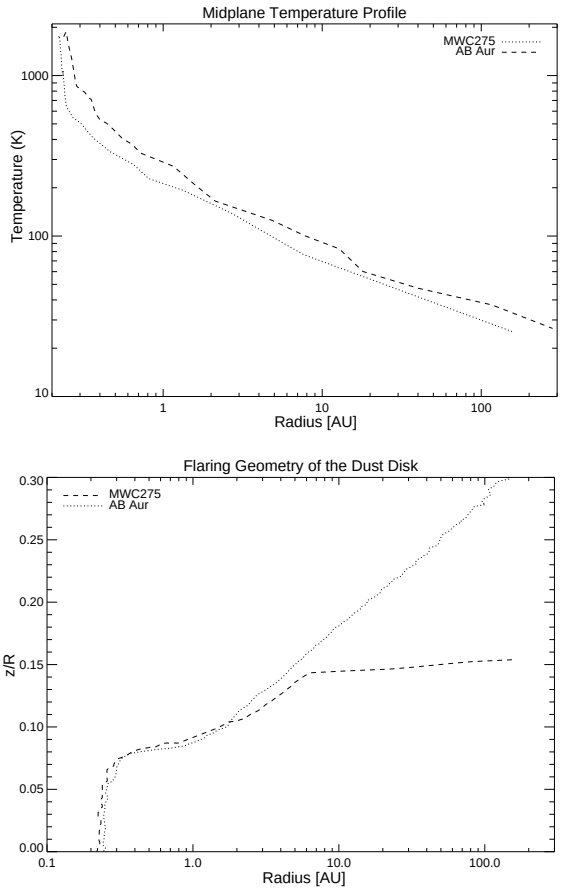

Figure 5.11 Temperature profile and disk-surface shapes for MWC275 and AB Aur. a) Top panel. Midplane temperature profile for MWC275 (dotted line) and AB Aur (dashed line). b) Bottom panel. The figure shows τ=1 at 5500Å surface of the disk measured along radial lines from the central star. The y axis is the polar angle (0 is the equatorial plane) in radians.

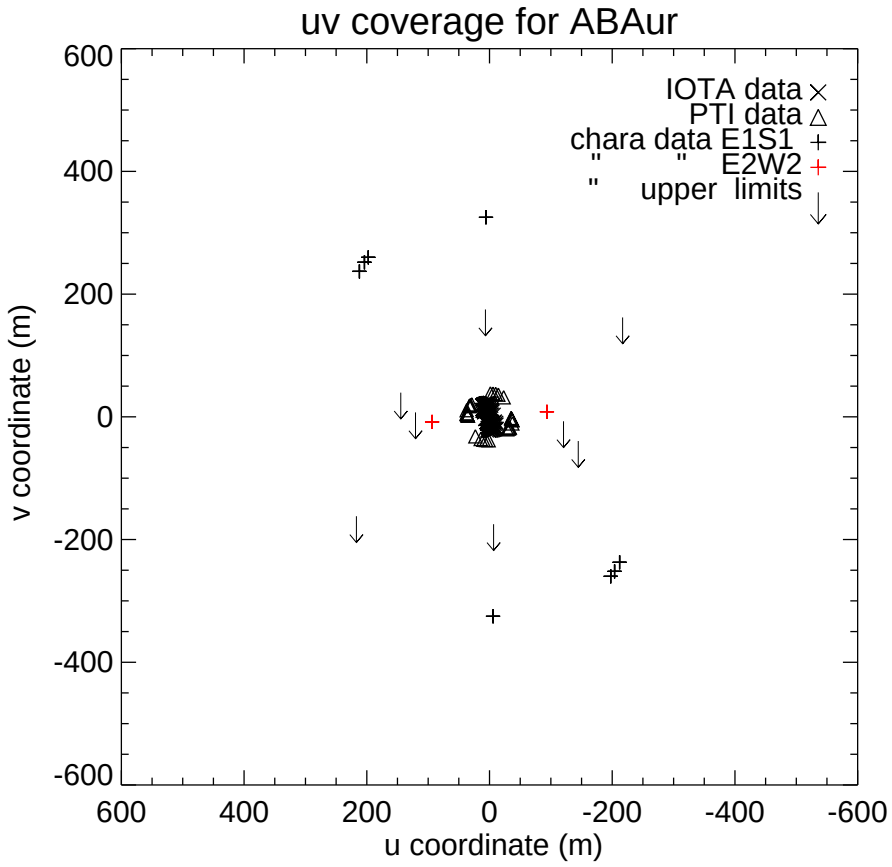

Figure 5.12 uv coverage for AB Aur. We include data from PTI (Eisner et al. [2004]), IOTA and CHARA (Tannirkulam et al. [2008]) in our analysis.

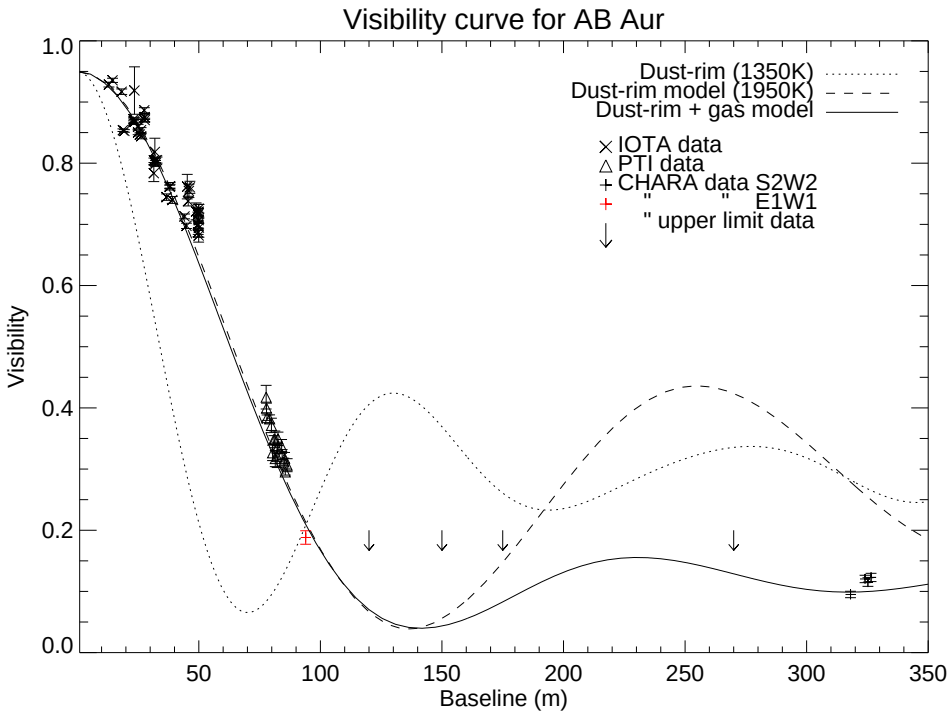

Figure 5.13 AB Aur visibility vs baseline. The arrows are upper limits on the visibility. The quoted model temperatures are at the base of the dust rims.

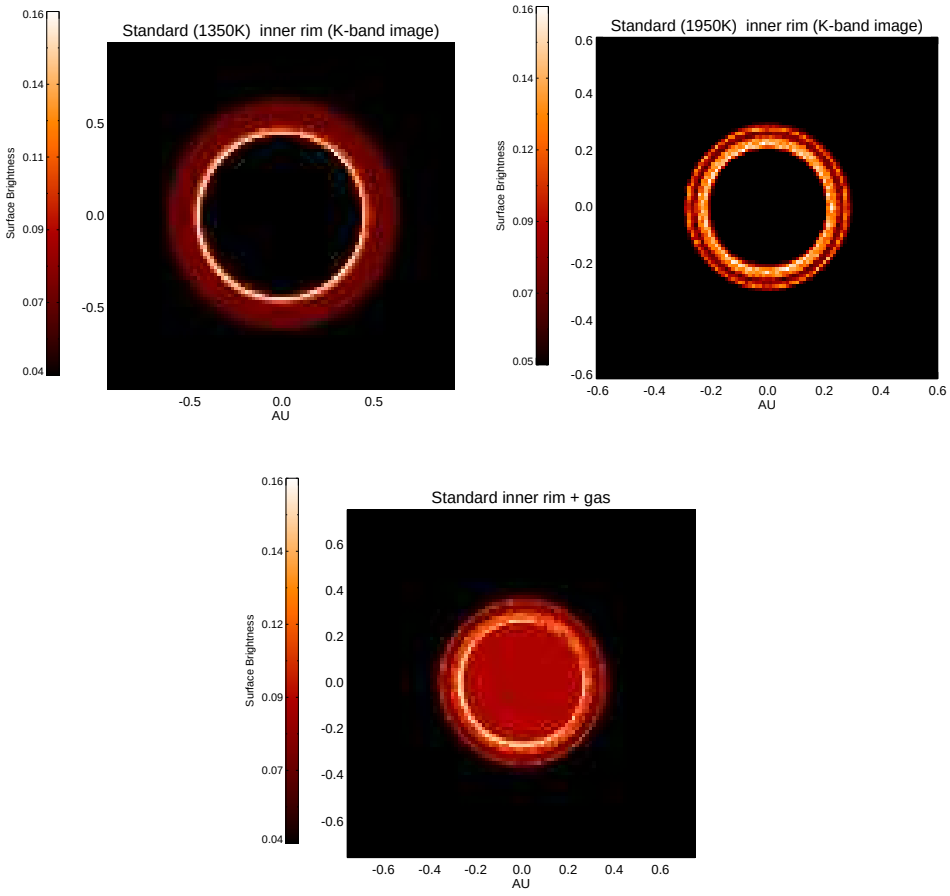

Figure 5.14 Face-on models for NIR emission in AB Aur. a) A standard curved dust-rim-only model with rim-base temperature ∼1350K. b) Top right panel. Standard curved dust-rim-only model with rim-base temperature ∼ 1950K. c) Bottom panel. Curved dust-rim model with gas emission (modeled as a uniform disk centered on the star) added inside the dust rim in to smooth out the emission profile. The central star has been suppressed in all the panels.

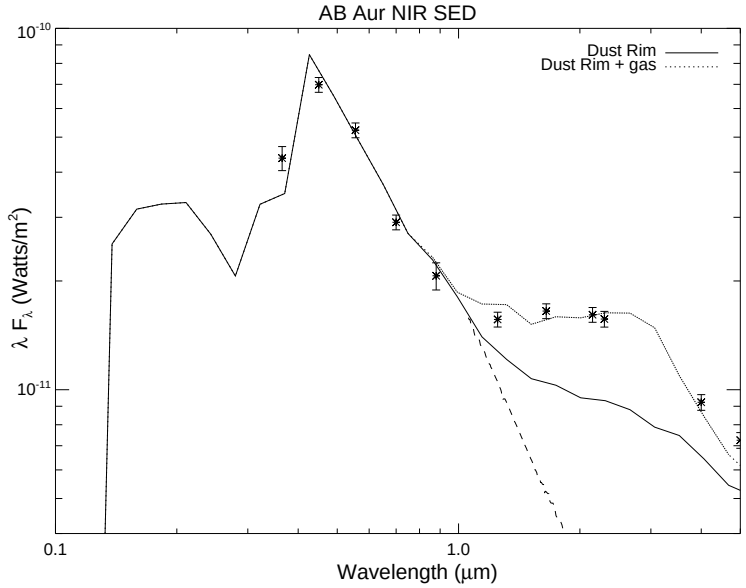

Figure 5.15 The NIR SED for AB Aur. The 'stars' are photometry points from MDM (Table 5.3). The solid line is the SED produced by the 'star + dust-rim only' model in Fig 5.14b. The dashed line traces the stellar SED. The dotted line includes emission from gas at 2500K, assuming that the gas opacity curve derived for MWC275 (see Fig. 5.7) is valid for AB Aur as well.

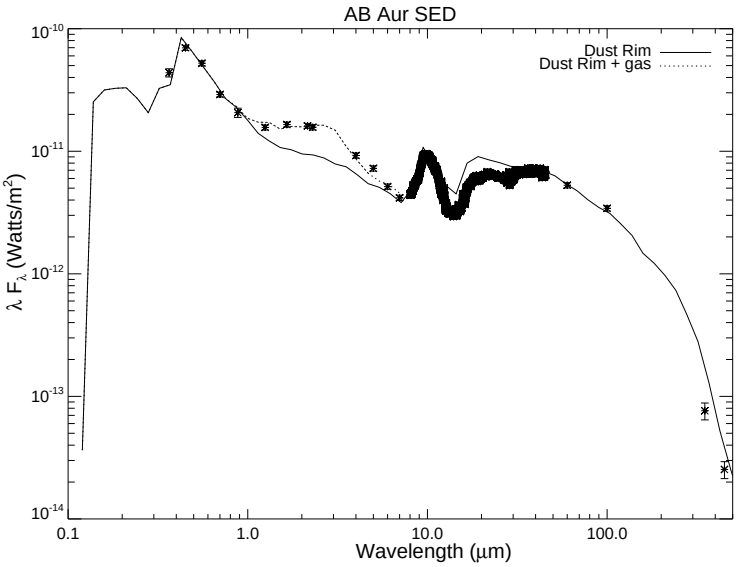

Figure 5.16 AB Aur SED from UV to mm. The mid, far-infrared and sub-millimeter data are from Meeus et al. [2001] and references therein. The solid line traces the dust-disk model SED (see §5.5.2). The dotted line traces the dust-disk + gas model. The relative contributions of star, dust and gas to the total integrated flux are 0.67, 0.27 and 0.06 respectively.

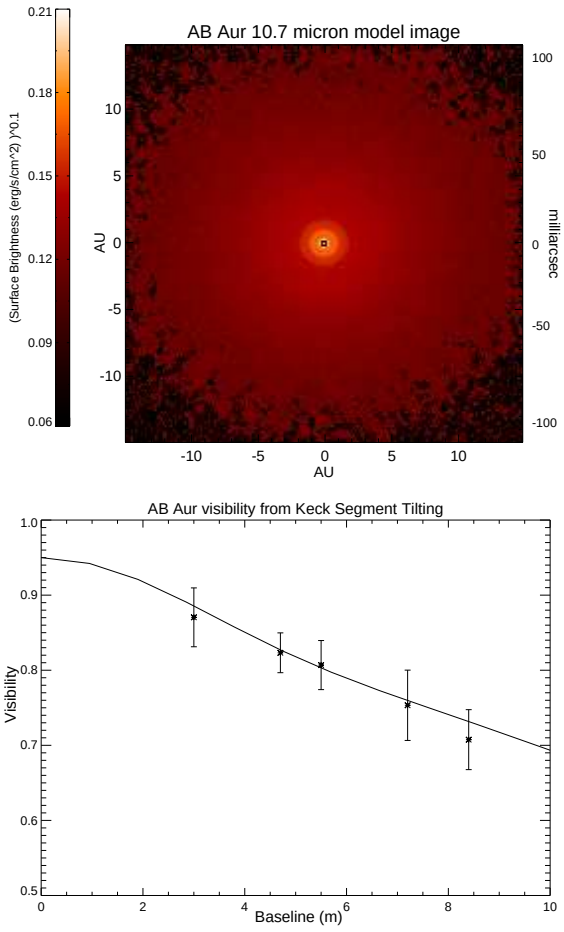

Figure 5.17 10.7μm image and visibilities for AB Aur. a) Top panel. Synthetic 10.7μm TORUS image b)Bottom panel. Model visibilities (solid line) compared with azimuthally averaged Keck Segment Tilting data (Monnier et al. [2004]). The model also includes 5% emission arising from an extended envelope.

Chapter 6

Summary and Future Work

This thesis studies several topics related to the structure of circumstellar disks in Herbig Ae stars. The first chapter introduces key results from long-baseline infrared interferometry in the last decade. Long-baseline interferometry has allowed us to make spatially resolved investigations of circumstellar disks and has helped revise long-held notions on disk morphology and evolution. Chapters 2 and 3 are focussed on theoretical models and observations of the gas-dust transition region (dust evaporation front) in proto-planetary systems. In Chapter 4, we presented preliminary results on the geometry of the planet formation region in disks from the novel Keck Segment Tilting Experiment. Chapter 5 discusses comprehensive models for the SED and interferometry on prototype Herbig Ae stars MWC275 and AB Aur. In this concluding chapter, we summarize the main contributions of this thesis and outline some future directions for research.

6.1 Key Contributions

(i) We developed a Monte-Carlo approach to calculate the structure of the dust evaporation front in a in a 2-D geometry. The advantage of this method over an analytic approach is that it allows for a self-consistent determination of the entire

disk structure. We showed that the geometry of the rim depends sensitively on dust properties. Dust growth and sedimentation may play a dominant role in determining the structure of the inner rim.

(ii) Current theories that explain the NIR excess (over stellar photospheric values) in Herbig Ae stars solely on the basis of a "puffed up inner rim" are too simplistic. Using long-baseline interferometry, we detected strong NIR emission inside to and on similar size scales to the dust destruction radius of Herbig Ae stars MWC275 and AB Aur. We argued that this new component corresponds to hot gas inside the dust sublimation radius. In the absence of shielding of star light by gas, we have also established that dust grains in the inner rim will have to be highly refractory sublimating at 1850K.

(iii) We presented the first set of comprehensive disk models for the SED and interferometry of Herbig Ae stars MWC275 and AB Aur. The small MIR size of MWC275 relative to AB Aur, shows that the dust grains in the outer disk are significantly more evolved/settled than the grains in the AB Aur disk. We suggest that dynamical processes (like planetesimal collisions) that maintain the population of micron-sized grains producing the 10μm feature in the spectrum, are operational only in the inner $\sim$7AU of MWC275. However, in AB-Aur the small-dust producing mechanisms exist at least out to $\sim$20 AU and maybe even beyond.

(iv) Using the Keck Segment Tilting Experiment designed by Prof. John Monnier and his collaborators, we resolved MIR emission in a number of Herbig Ae/Be systems. Preliminary analysis suggests that the colors and surface brightnesses of disks in Herbig Ae stars vary smoothly between Group I and Group II sources. As noted by

previous authors, Group I sources tend to be systematically redder and of lower surface brightness than Group II sources. This trend is reproduced by simple geometric models for circumstellar disks. The bulk of MIR emission arises from the inner rim in Group II sources, whereas emission in Group I sources is dominated by the outer flared disk. Disks in Herbig Be stars have larger surface brightness than predicted by passive flared-disk models, probably due to the presence of strong accretion heating. (v) With imaging from the Keck Segment Tilting Experiment, we presented the discovery of a circumbinary disk around the Herbig Be system v892 Tau, first reported in Monnier et al. [2008a]. We proposed a new SED decomposition for the system in terms of two B8V stars reddened by an A_V =10.95. The MIR flux in v892 Tau is characterized as a T $\sim$ 450K blackbody, consistent with emission from the warm inner wall of the circumbinary disk.

6.1.1 Relevance of work to planet formation studies

- **Determination of physical conditions in the inner regions of circumstellar disks.** We determined the geometry and the temperature structure of the MWC275 and AB Aur disks in Chapter 5. We also showed in Chapter 4 that for certain evaporation front models, the midplane temperature in the shadow region can fall below the sublimation temperature of water ice. The presence of a cold reservoir of material close to the star can have implications on the chemistry and abundance of volatile elements in planets. The concentration of ices (sensitive to pressure and temperature) can also significantly affect the ability of gas-giant planets to accrete (Lissauer & Stevenson [2007]).

We showed in Chapter 5 that the dust in the sublimation front could be significantly more refractory than assumed in the literature. Refractory dust grains may play a major role in fixing the abundance of elements in terrestrial planets.

- **Detection of early stages of planet formation.** The initial step in both giant (Pollack et al. [1996]) and terrestrial (Wetherill [1990]) planet formation is the coagulation of dust to form planetesimals. We suggest in Chapter 5 that planetesimal collisions are active in the inner 20AU of the AB Aur disk, making it an excellent laboratory for studying the first stages of planet formation. The dynamic nature of the AB Aur disk is further supported by the detection of arcs and rings (Grady et al. [1999]; Fukagawa et al. [2004]; Oppenheimer et al. [2008]) and a possible hot spot (Millan-Gabet et al. [2006]).
- **Determination of boundary conditions for planet migration.** The structure of the inner-gas disk plays an important role in determining the orbital properties of terrestrial planets (Najita et al. [2007]). Understanding inner-disk structure and measurements of the gas content will also shed light on how the inward radial migration of gas-giant planets is halted (Lin et al. [1996]). Thus, the spatially-resolved detection of gas inside the dust destruction radius (Chapters 3 and 5) provides exciting future possibilities for directly constraining boundary conditions in models of planet dynamics (Nagasawa et al. [2007]).

6.2 Way Forward

This thesis highlights a number of outstanding issues in our understanding of circumstellar disk structure, namely a) What is the geometry of the gas dust transition region? To date there has been no calculation of the transition region structure that treats both gas and dust simultaneously in a self consistent manner. b) What are the relative contributions of accretion and stellar radiation to heating gas inside the dust rim? c) What are the gas species that provide NIR opacity? d) Does the presence of a shadow affect chemistry in the planet formation region? and e) Do Groups I and II represent distinct stages in the evolution of circumstellar disks? Why are most Herbig Be disks Group I?

To address some of the questions regarding the structure of the inner disk,we recently submitted a NASA Origins of Solar Systems proposal (PI: Prof. John Monnier, Science PI: Ajay Tannirkulam, Co-Is: Prof. Nuria Calvet and Dr. Tim Harries, Collaborators: Dr. James Muzerolle, Dr. Theo ten Brummelaar, Dr. Rafael Millan-Gabet, Dr. Silvia Alencar, Dr. Jesus Hernandez and Zhaohuan Zhu) with the following scientific goals -

- **Determine the structure of the gas flow from a few tenths of an AU down to the stellar surface and clarify the "star-disk connection".** By measuring Balmer line profiles and modeling them with a hybrid magnetospheric accretion and wind model (Muzerolle et al. [2004]; Alencar et al. [2005]; Kurosawa et al. [2006]), we will obtain mass accretion rates for a well-selected sample of Herbig Ae/Be stars with known IR-disk properties. In addition, we will determine the structure of the inner gas-disk with resolved interferometry

of the gas-surface-brightness profile (Chapters 3 and 5). Conversion of surface brightness profiles into measurements of surface density and temperature structure will require accurate estimates of the wavelength dependence of gas opacity. First steps in this direction have been taken in Chapter 5 by deriving empirical estimates of gas opacity (Fig 6.1) from observed photometry and self-consistent models for the dust evaporation front. The surface density of the disk is directly related to the mass accretion rates, temperature and the viscosity parameter in quasi-steady-state disks (Shakura & Sunyaev [1973]). Simultaneous measurements of mass infall rates (through spectroscopy) and the gas surface density profiles (through interferometry) opens up the fascinating possibility of directly constraining the viscosity parameter-α in the inner disk. The viscosity parameter is key to understanding angular momentum transport in circumstellar disks.

HAe/Be stars power strong winds (Mottram et al. [2007]). The wind geometry and launch mechanism are poorly understood. Using NIR interferometry, Tatulli et al. [2007] and Kraus et al. [2008b] demonstrated that winds in some HAe/Be stars get launched on similar length scales to the dust sublimation radius. Combining continuum NIR interferometry measurements with the magnetospheric/wind models for accretion/ejection sensitive lines, new constraints on the geometry of the wind-launching region will be obtained. These will be crucial in informing and validating (e.g. Kurosawa et al. [2008]) detailed magneto-hydro-dynamic (MHD) simulations of the star-disk connection that are now available in the literature (e.g. Romanova et al. [2008]).

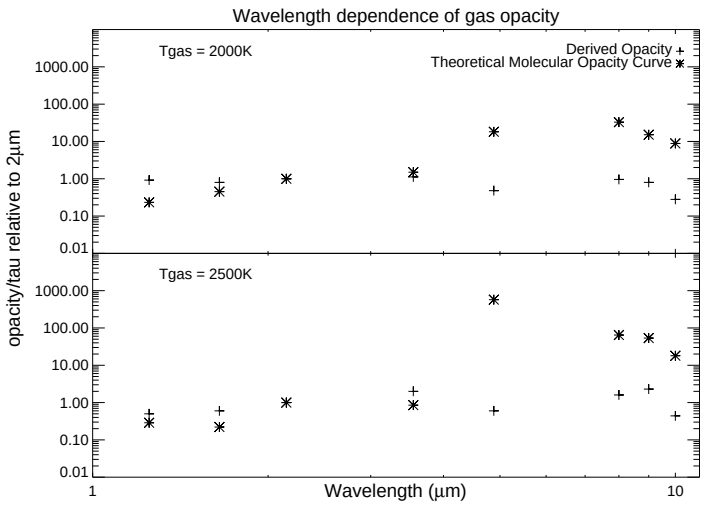

Figure 6.1 Empirically derived gas opacities. The plusses (+) represent empirically derived gas opacities from observed photometry and near-infrared disk models for MWC275. The stars represent fiducial theoretical molecular absorption opacities smoothed over the photometry band for 2000K and 2500K gas respectively (Zhu et al. [2007]). The opacity jump at 5μm is due to water vapor.

A complementary approach to optical-emission-line and NIR interferometric studies of the inner disk has been through high-resolution spectroscopy work on molecular lines of CO, HCN, H_2C_2 and H_2O (Najita et al. [2003]; Brittain et al. [2005]; Najita et al. [2007]; Gibb et al. [2007]). Some of these molecules have been shown to be good tracers of the total gas content in the inner disks of YSOs. Furthermore, column density measurements of these gas species have been compared with dust extinction to constrain dust evolution processes in disks. We have only begun to tap the full potential of gas diagnostics, which at the moment suffers from lack of knowledge of the gas composition and good physical models for the inner disk.

- **Determine the geometry of the dust evaporation front.** Models of the evaporation front in the literature (Dullemond et al. [2001]; Isella & Natta

[2005] and Chapter 2) ignore the effect of gas accretion heating and gas opacity on the structure of the inner rim. NIR interferometry studies (Akeson et al. [2005b]; Eisner [2007]; Kraus et al. [2008a] and Chapter 3) seem to directly challenge this assumption by detecting significant gas emission within the dust destruction radius. We plan to perform a self-consistent calculation of the front structure, including gas opacity and accretion heating.

In Chapter 5 we demonstrated that the temperature of the evaporation front could be as high as 1850K, much higher than ∼1400K value typically assumed in the literature. The high temperatures of the front make it an ideal site for thermal reprocessing of dust grains and gas-phase chemistry. Using MIR interferometry, van Boekel et al. [2004] showed that dust in the evaporation front is highly crystalline. The origins of the crystallinity are poorly understood. Some suggested mechanisms are gas-phase condensation and thermal annealing of grains (Gail [2004]). Our calculations of density and temperature in the evaporation front will provide critical input to models of dust phase-chemistry at the inner rim and contribute to our understanding of the evolution of dust from which Earth-like planets are built.

A major point to note here is that the evaporation front and the inner disk will not be resolvable even by Atacama Large Millimeter/submillimeter Array (ALMA), and near and mid-infrared interferometry are the most powerful tools currently available to study the inner disk structure.

We next outline the observations and modeling needed to achieve the scientific goals.

6.2.1 Observations

Spectroscopy

We wish to determine mass infall rates and model the wind profiles for our target pre-main-sequence stars by computing (see §6.2.3) the Hα, Hβ and Hγ line profiles. The forbidden lines of O[I] and S[II] which are wind/disk atmosphere diagnostics will be used to obtain mass outflow rates and constrain results from the Balmer line determinations. The modeling work requires kinematically resolved spectra of these lines with simultaneous measurements on all lines (this is important because the lines are known to be time variable). Fig 6.2 shows sample high resolution optical spectra that we obtained with MIKE (Magellan Inamori Kyocera Echelle spectrograph, Bernstein et al. [2003]). Mike is on Clay - a 6m class telescope at the Magellan Observatories.

The gas species providing NIR opacity (Fig 6.1) inside the dust-destruction radius have not been identified yet. High resolution NIR spectra are necessary to resolve and identify kilo-kelvin temperature molecular lines.

6.2.2 Near-Infrared Long-baseline Interferometry

Detailed, spatially-resolved studies of the dust rim and the inner-gas disk of even the closest ($\sim$ 150pc) Herbig Ae/Be stars require milli-arcsecond resolution. The CHARA array and VLTI are well suited for this task. Using CHARA, we have completely resolved the dust rim in AB Aur and MWC275 (Chapter 3) and detected gas emission inside the dust destruction radius. Besides the K-band data presented in Chapters 3 and 5, we have started H-band observations of YSOs. The spatial

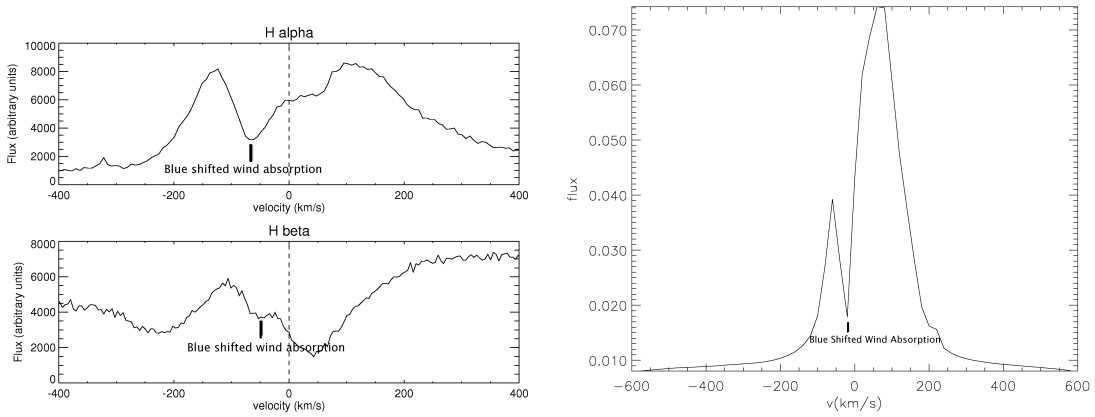

Figure 6.2 Hα and H$_\beta$ line profiles. (a) Left panel. Hα and H$_\beta$ line profiles for MWC275 obtained with MIKE . The blue shifted wind absorption feature seen in MWC275 is reproduced in our model on the right panel. (b) Right panel. Hα line profile (Lima et al. [2008], in prep) for a model characterized by parameters typical of a Classical T Tauri star: mass 0.5 M$_\odot$, radius 2R$_\odot$, stellar effective temperature 4000K, mass accretion rate 10^{-8}M$_\odot$yr^{-1}. The magnetospheric radius is $\sim$ 3 stellar radii, and the wind region extends from 3 to 20 stellar radii; the mass loss rate is 10^{-9} M$_\odot$ yr^{-1}. The T Tauri models will be extended into the HAe/Be regime to self-consistently determine mass accretion and mass loss rates.

resolution at H-band is significantly higher than K-band and H-band also probes hotter gas. Combined with the α-disk model, the surface brightness profile of the gas provides a new diagnostic for $\dot{M}$, and a direct connection between the disk properties and properties of the magnetospheric accretion flow.

The commissioning of the fringe tracker (Fig 6.3, Berger et al. [2006]) for CHARA-MIRC (Fig 6.3, Monnieret al. [2007]) in the summer of 2008 will open a new observational frontier. The fringe tracker will sufficiently improve CHARA-MIRC sensitivities to combine light from 3 or more telescopes, allowing the first milli-arcsecond non-parameteric imaging of MWC275 and AB Aur in the NIR. The snapshot multiple baseline coverage will provide us a powerful tool in understanding infrared time variability of YSO disks.

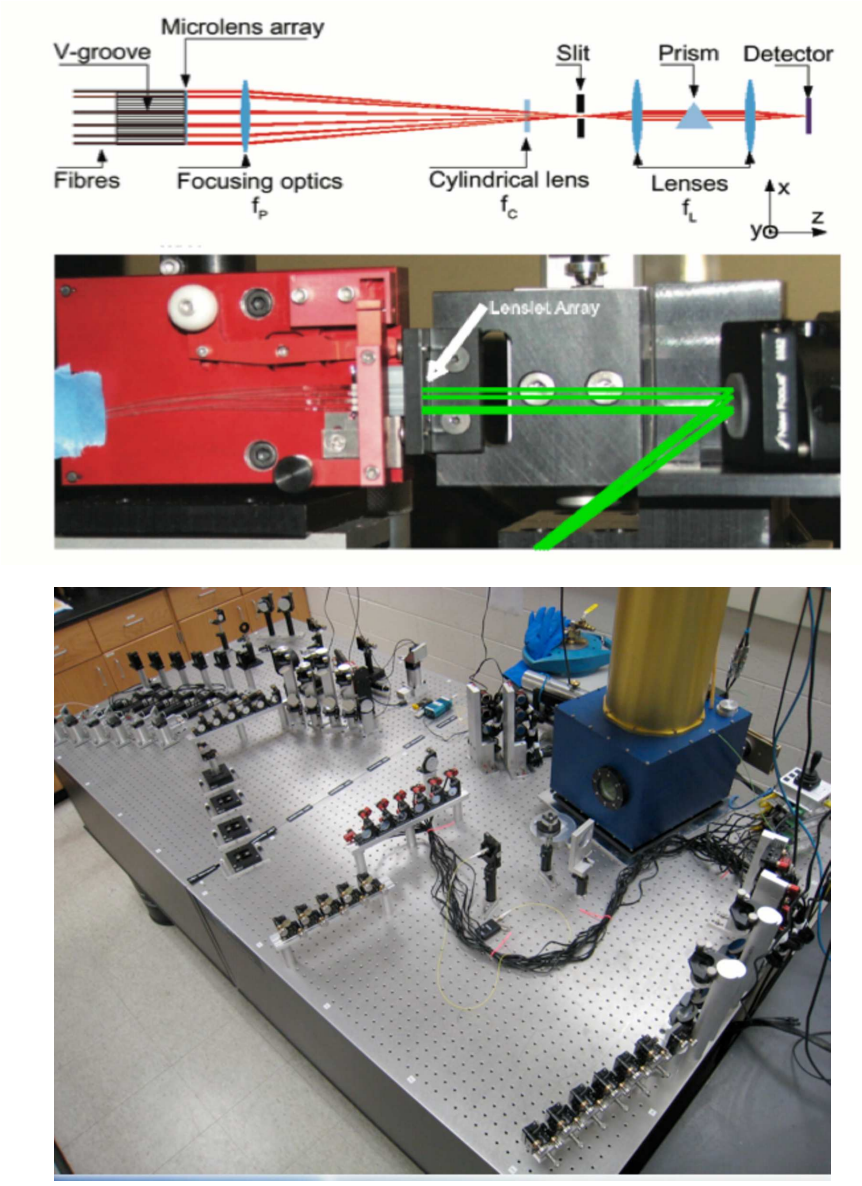

Figure 6.3 MIRC and CHAMP. (a) Top Panel. The MIRC combiner (Monnieret al. [2007]). (b) Bottom Panel. The fringe tracker CHAMP (Berger et al. [2006, 2008]).

6.2.3 Modeling

Accretion models have tended to focus on two separate physical scales (i) the processes of mass and angular momentum in the outer disk (extending from several 100 AU down to tens of stellar radii) (ii) gas accretion from a few stellar radii on to the stellar photosphere. There have been few studies directly connecting properties of gas falling onto the stellar photosphere with physical properties (density and temperature) of the inner disk.

We propose to bridge this gap by adopting a two-stage approach to modeling the accretion process. Balmer line profiles that are sensitive to accretion/ejection will be self-consistently modeled using a hybrid, magnetospheric accretion and wind model (Muzerolle et al. [2004]; Alencar et al. [2005]; Lima et al. 2008, in prep). The accretion rate determined from this model will be converted into a gas-disk surface density profile following the Sunyaev-Shakura prescription (Shakura & Sunyaev [1973]). The gas surface density profiles will then be fed into a Monte-Carlo radiative transfer code -TORUS and predictions will be made for SED and interferometric measurables of the inner disk. This two-stage modeling procedure links properties of the magnetospheric accretion flow to the properties of the disk providing new constraints on the physics of gas accretion, and its affects on the structure of the inner disk.

The hybrid, magnetospheric accretion and disc-wind model

The modeling strategy for magnetospheric accretion would follow the work of Hartmann et al. [1994]; Muzerolle et al. [1998, 2001]. The stellar magnetosphere is assumed to be a dipole, symmetric about the star's rotation axis and perpendicular to

the circumstellar disk. Material from the disk gets channeled along the magnetic field lines, and matter falls onto the star ballistically. The gas gets shocked and heated as it hits the stellar surface. Figure 6.2 shows the theoretical Hα line profile for a T Tauri star with typical parameters.

A significant difference between the T Tauri case and Herbig Ae/Be stars is the strong wind contribution to the Balmer lines (Mottram et al. [2007]). Our group has been successful (Kurosawa et al. [2006]; Lima et al. 2008, in prep) in combining a wind component with the magnetospheric model (Fig 6.2). The hybrid magnetospheric-accretion/disc-wind codes will be used to study the wind and disk-atmosphere components to the line strengths and line profiles of Herbig Ae/Be stars and constrain their mass accretion/ejection rates.

Continuum radiative transfer modeling

New modules will be incorporated into the TORUS code to explore the effects of gas on inner rim structure. The modeling of gas structure within the inner rim will help translate gas surface brightness profiles obtained from interferometry into a measure of mass accretion rates, complementing and constraining infall measurements made with the magnetospheric model.

The above outlined analysis of the inner-AU circumstellar-material properties for MWC275, AB Aur and V1295Aql, will strongly constrain models of accretion, winds and proto-planetary-disk structure and thereby inform planet-formation theories.

We also wish to emphasize that the VLT Interferometer along with the MIR combiner MIDI (Leinert et al. [2004]) will soon be observing several Herbig Ae/Be at multiple baseline orientations to validate the existence of the geometric "shadow"

behind the inner rim. These observations will also constrain the spatial distribution and composition of dust in the inner AU of circumstellar disks. As highlighted in Fig 4.2 MIDI observations will strongly inform our understanding of dust processes in the evaporation front and the terrestrial planet formation region.

6.3 Concluding Remarks

In this thesis, we have presented results on circumstellar disk structure combining state-of-the-art modeling techniques and cutting edge infrared interferometry. Our understanding of disk structure and evolution is rapidly progressing. The commissioning of new instruments at CHARA and VLTI allowing milli-arcsecond interferometric "imaging" of young stellar objects, and the Atacama Large Millimeter Array (ALMA) will soon revolutionize our notions of gas and dust physics in proto-planetary disks. Personally, graduate work in this fast changing field has been an exciting and rewarding journey.

Appendices

Appendix A

Analytic Estimate for Rim Shape

Here, we derive a general analytic formula for the rim shape of a dust segregation model (a case with specific numerical values for parameters, was discussed in §2.4.2).

Let the densities of the two dust components in the circumstellar disk be given by

$$\rho_{\rm large} = A_{\rm large}\rho_{o\_{\rm gas}} \exp\left[-\frac{1}{2}\frac{z^2}{(\zeta_{\rm large}h)^2}\right] \tag{A.1}$$

$$\rho_{\rm small} = A_{\rm small}\rho_{o\_{\rm gas}} \exp\left[-\frac{1}{2}\frac{z^2}{(\zeta_{\rm small}h)^2}\right] \tag{A.2}$$

where $\rho_{\rm large}$ and $\rho_{\rm small}$ are the densities of large and small grains respectively and $\rho_{o\_{\rm gas}}$ is the gas density in the mid-plane. $A_{\rm large}$ and $A_{\rm small}$ are normalization factors for the dust densities, z is the height from the disk mid-plane, h is the gas scale height and $\zeta_{\rm large}$ and $\zeta_{\rm small}$ are the scale heights for large and small grains as fractions of the gas scale height.

The ratio of Planck mean opacities at the dust evaporation temperature and the stellar effective temperature - $\epsilon(z)$, then becomes

$$\epsilon\left(z\right) = \left[\frac{A_{\rm large}K_{\rm P_{large}}(T_{\rm evp}) + A_{\rm small}K_{\rm P_{small}}(T_{\rm evp})\exp\left(\frac{1}{2}\frac{z^2(\zeta^2_{\rm small}-\zeta^2_{\rm large})}{h^2\zeta^2_{\rm large}\zeta^2_{\rm small}}\right)}{A_{\rm large}K_{\rm P_{large}}(T_*) + A_{\rm small}K_{\rm P_{small}}(T_*)\exp\left(\frac{1}{2}\frac{z^2(\zeta^2_{\rm small}-\zeta^2_{\rm large})}{h^2\zeta^2_{\rm large}\zeta^2_{\rm small}}\right)}\right] \tag{A.3}$$

where $K_{\mathrm{P}_{\mathrm{large}}}$ and $K_{\mathrm{P}_{\mathrm{small}}}$ are Planck mean opacities for large and small grains at the specified temperatures, T_{evp} is the dust evaporation temperature and T_* is the stellar effective temperature.

Neglecting local accretion heating, the dust destruction radius R_{evp} (see Isella et al. [2006]; Calvet et al. [1991]) is

$$R_{\mathrm{evp}}\,[\mathrm{AU}] = 0.034\,[\mathrm{AU}] \left(\frac{1500K}{T_{\mathrm{evp}}}\right)^2 \left[\left(\frac{L_*}{L_\odot}\right)\left(B + \frac{1}{\epsilon(z)}\right)\right]^{1/2}, \tag{A.4}$$

L_* is luminosity of the star in solar units. B is a dimensionless diffuse heating term, characterizing the rim optical depth to its own thermal emission.

The gas scale height h at R_{evp} is estimated to be (see eqs. (7) & (8) from Chiang & Goldreich [1997])

$$h\,[AU] = R_{\mathrm{evp}}\,[\mathrm{AU}] \left[\left(\frac{T_{\mathrm{gas}}}{4\times10^7 K}\right)\left(\frac{M_\odot}{M_*}\right)\left(\frac{R_{\mathrm{evp}}}{4.64\times10^{-3}\ \mathrm{AU}}\right)\right]^{1/2} \tag{A.5}$$

where T_{gas} is the temperature of the bulk of the gas (assumed to be isothermal) and M_* is mass of the star in solar masses.

Combining equations (A3), (A4), and (A5), the height of the evaporation front as a function of distance along the disk mid-plane from the star becomes

$$\begin{aligned} z[\mathrm{AU}] = R_{\mathrm{evp}}[\mathrm{AU}] \Bigg[2\zeta_{\mathrm{diff}}^2 \ln\left(\frac{A_{\mathrm{large}}K_{\mathrm{P}_{\mathrm{large}}}(T_*) - Y A_{\mathrm{large}}K_{\mathrm{P}_{\mathrm{large}}}(T_{\mathrm{evp}})}{Y A_{\mathrm{small}}K_{\mathrm{P}_{\mathrm{small}}}(T_{\mathrm{evp}}) - A_{\mathrm{small}}K_{\mathrm{P}_{\mathrm{small}}}(T_*)}\right)\Bigg]^{1/2} \\ \times \left[\left(\frac{T_{\mathrm{gas}}}{4\times10^7 K}\right)\left(\frac{M_\odot}{M_*}\right)\left(\frac{R_{\mathrm{evp}}}{4.64\times10^{-3}\ \mathrm{AU}}\right)\right]^{1/2} \end{aligned} \tag{A.6}$$

where Y and ζ_{diff} are dimensionless terms given by

$$Y = \left(\frac{1.71\times10^{-10}\mathrm{AU}^{-2}K^{-4}R_{evp}^2 T_{\mathrm{evp}}^4}{L_*/L_\odot} - B\right) \tag{A.7}$$

$$\zeta^2_{\text{diff}} = \frac{\zeta^2_{\text{small}}\zeta^2_{\text{large}}}{\zeta^2_{\text{small}} - \zeta^2_{\text{large}}} \tag{A.8}$$

Appendix B

Optical and Near-Infrared Photometry of Young Stellar Objects.

The principal scientific goal of my thesis was to do a detailed case by case modeling of Herbig Ae disks and confront current disk models with interferometry and spectral energy distribution data (SED). Multi-wavelength photometry is required to constrain model parameters. Besides this, due to the limitations of two-telescope long baseline interferometry, broadband SEDs are needed to inform interpretations of the fringe data. It is now well known that that the visible and infrared fluxes from YSOs are time variable (e.g. Carpenter et al. [2002], Fig §B.1) complicating interferometry interpretation. To avoid problems with using decade old photometry from the literature, we obtained new flux measurements nearly coeval with the interferometry data on a number of YSOs.

The high brightness of the targets allowed us to observe a dozen or so objects on clear nights with meter sized telescopes. All the data were observed at the MDM observatory (of which University of Michigan is a partner) with the 1.3m McGraw-Hill and 2.4m Hiltner telescopes.

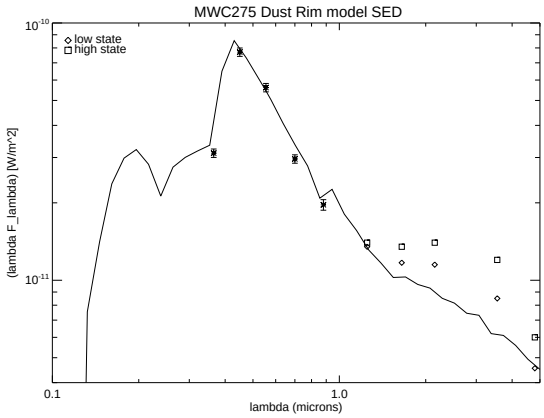

Figure B.1 YSO time variability. The optical and NIR flux for MWC275. The 'stars' are photometry points from MDM. The 'squares' and 'diamonds' are high and low state measurements from Sitko et al. [2008]. The optical light in MWC275 remained unchanged between 1998 and 2006, but the NIR flux rose to maximum in 2002 and then began to fall down.

B.1 Description of Telescopes and Instruments

The MDM observatory is located on the southwest ridge of Kitt Peak, west of Tucson, Arizona. It is owned and operated by the University of Michigan, Dartmouth College, the Ohio State University, Columbia University and Ohio University. The observatory runs two telescopes - McGraw-Hill and Hiltner.

The McGraw Hill telescope was built by Tinsley of California and has an optically worked surface with a 1.27m diameter. The telescope can be used in f/7.6 and f/13.5 Cassegrain configurations. The telescope is on an equatorial mount and can be auto guided in both off-axis and slit plate reflection modes.

The Hiltner telescope was designed by DFM engineering of Colorado and built by L&F industries of California. The telescope has clear aperture of 2.32m and can be used in f/7.5 and f/13.5 Cassegrain configurations. The Hiltner telescope is also an equatorial mount and has instrumentation for off-axis and slit-plate guiding.

The instruments that we used for photometry at the MDM observatory are-

- **8K Imaging Camera:** The 8K Camera was built by Columbia University and operates between 3300Åand 8500Å. The detector plane is a 4×2 mosaic of 2048×4096 CCDs. The field of view is 25 arcmin at the 2.4m and 46 arcmin on the 1.3m telescope. Bessel U, Harris B, Harris V, Harris R, Arizona I, Gunn Z, a broad R and Hα are the currently available filters.
- **Templeton:** Templeton is a 1024×1024 CCD detector for use between 3300Åand 9500Å. The detector gets mounted on the back-end of the Multiple Instrument System (MIS), which comprises of the finder, guider and filter-wheel modules, and spectral calibration and flat field lamps.
- **OSU IR Camera:** The OSU IR Camera (also known as TIFKAM) is an infrared imager and spectrometer that operates in the 1-2.5μm range built by Ohio State University and the MDM consortium. The instrument has a 512×1024 InSb detector array and is equipped with a standard set of JHK filters and moderate resolution grisms.

Details on the telescopes and instruments can be found in - http://www.astro.lsa.umich.edu/obs/mdm/index.html. The photometry filter characteristics are listed in Table B.1.

B.2 Observations

The photometry on various targets were collected in 4 runs (lasting roughly a week each) in November 2004, December 2005, June 2006 and August 2006. Typically, 2.5 nights on each run were good for absolute photometry. The first photometry

Table B.1 Photometry filter properties.

Name	Central Wavelength (μm)	FWHM (μm)
Bessel U	0.364	0.032
Harris B	0.435	0.098
Harris V	0.538	0.098
Harris R	0.630	0.118
Arizona I	0.805	0.150
J	1.25	0.16
H	1.63	0.15
K	2.20	0.19

campaign in November 2004 was conducted on the 1.3m McGraw-Hill telescope. The 8K and TIFKAM were used to collect photometry in the U, B, V, R, I, J, H and K bands. To calibrate the data, the targets were interspersed with observations of Landolt standards (in the optical, Landolt [1983, 1992]) and CTIO standards (for NIR, Elias et al. [1982]) at air masses similar to that of the targets. Most of our targets are bright by astronomical standards and the telescope had to be defocussed to avoid saturation of detector pixels. The typical donut shape for the defocussed stellar images is shown in Fig B.2.

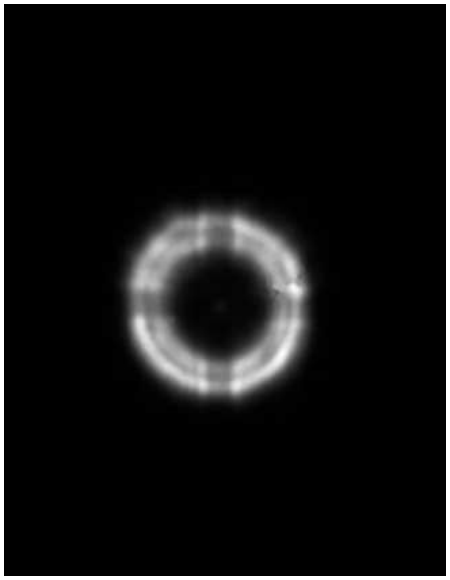

Figure B.2 Defocussed H band image of AB Aur.

Within the CCD/array, each pixel element has different quantum efficiency compared to neighboring pixels. To flatten the detector response, we obtained twilight flats. Zero light exposures (darks) were taken at different exposure times to constrain the dark current and subtract the detector background from the data. Besides this, we also took a number dome-light exposures close to midnight, to verify linearity of the detectors. Fig B.3 shows the H-band counts on an 'average' TIFKAM InSb array element as function of time. The element is linear to better than 3% till 8000 counts, beyond which it begins to go non-linear. We were careful in adjusting the telescope defocus and exposure time to keep the detector counts in the linear regime.

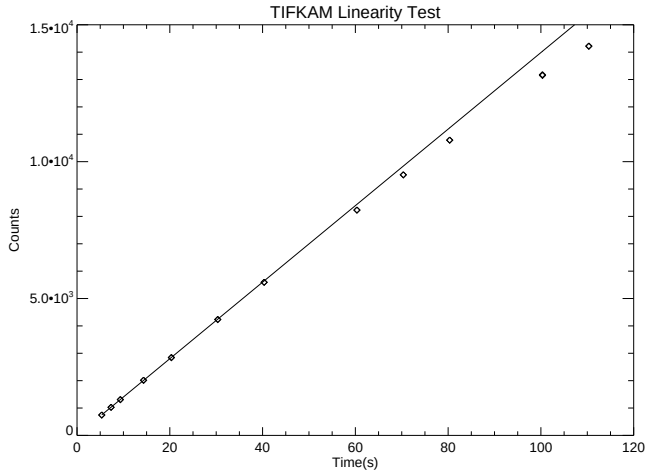

Figure B.3 TIFKAM linearity test. The solid line is a linear fit to the data.

The McGraw-Hill telescope proved to be extremely inefficient for an observing program like ours where the telescope needs to be moved many times between target stars and calibrators. Under such situations the 'pointing' for had to be reset fairly frequently for the telescope. For subsequent observing runs, we switched to the Hiltner 2.4m telescope. The optical data at the 2.4m were taken with the Templeton detector and the infrared observations were done with TIFKAM. Tables B.2 and B.3

present the complete observing logs from the MDM observatory.

B.3 Data Reduction

The following steps constituted the data reduction (these are standard) procedure -

- **Flat Fielding:** The multiple sky flats from each night were combined to produce mean flats in the observation bands. The mean flats were used to produce flat fielded stellar images defines as

$$\text{Image}_{\text{clean}} = \frac{\text{Image}_{\text{raw}} - \text{mean(Dark)}}{\text{mean(Flat)} - \text{mean(Dark)}} \tag{B.1}$$

  where, Image_{raw} is the raw stellar image and Darks are exposures with the camera shutters closed. Flat fielding corrects gradients in pixel gain across the detector. Special care was taken to identify and correct for bad detector pixels during this reduction step.

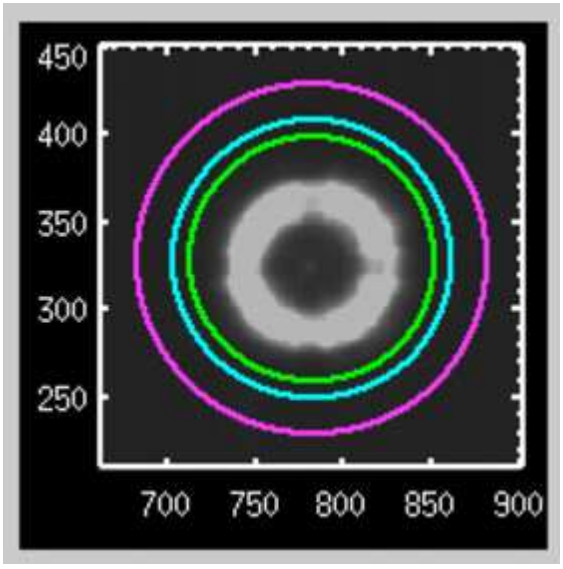

Figure B.4 Aperture photometry on a star.

- **Aperture Photometry:** The counts on the source and calibrator were extracted from the flattened images using ATV - an aperture photometry code (Barth [2001]). Fig B.4 illustrates the photometry technique. The inner-most light-green circle defines the boundary of the star. The counts inside this region are summed to give the total source+background counts. The light-blue and the purple circles define the region from which the sky-background is estimated. The code then subtracts the background from the counts in the inner circle to estimate star counts. Fig B.5 shows a radial slice of the counts in the star from Fig B.4.

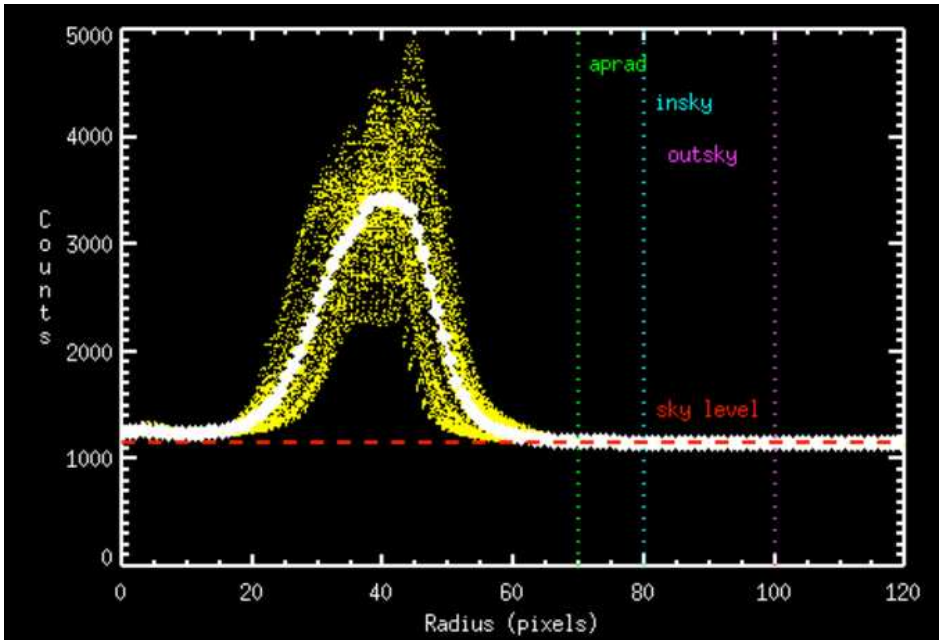

Figure B.5 The radial count profiles on a star. The vertical lines indicate the regions from which ATV estimates the source and background counts.

- **Calibration:** Fig §B.6 shows a V band calibration plot for the night of 12th December, 2005. The X-axis is the Landolt magnitude for the calibrators and the Y-axis is the logarithm of calibrator counts obtained in the previous reduc-

tion step. The solid line is the best linear fit with the following form -

$$\text{magnitude} = -2.5\log(\text{counts}) + \text{C} - (1.086 \times \text{airmass} \times \alpha) \pm \text{error} \qquad \text{(B.2)}$$

The offset C and the airmass correction α are optimized with a χ^2 minimization code. The dispersion from the linear relation is a measure of the robustness of the calibration.

This procedure is carried out in each of the bands to determine the offset and the airmass correction. The best linear-fit formula is then used to convert the source counts into astronomical magnitudes. Tables §B.2 and §B.3 list the calibrated magnitudes and the error estimates for all of out targets.

The chara

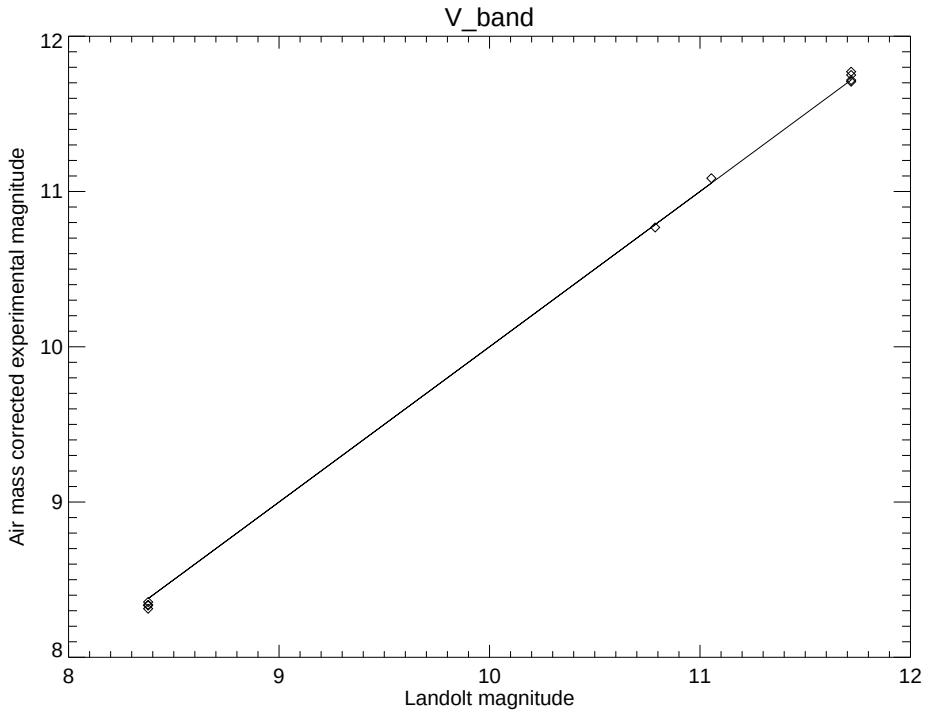

Figure B.6 V band calibration plot. The squares are MDM data points, and the solid line is the calibration fit.

Table B.2: UBVRI Photometry. Majority of the MDM targets are YSOs.

Target	RA (J2000) h m s	Dec ° ′ ″	U mag	B mag	V mag	R mag	I mag	UT Date
HIP2080	00 26 16.5	+ 03 49 33	-	6.72±0.05	6.81±0.04	6.94±0.06	6.93±0.04	08/27/2006
HIP2370	00 30 16.4	− 29 14 38	-	12.65±0.05	12.28±0.04	12.13±0.06	11.75±0.04	”
HIP3013	00 38 20.3	−14 59 54	-	10.67±0.05	10.86±0.04	6.95± 0.06	11.07±0.04	”
BP Tau	04 19 15.8	+ 29 06 27	13.20±0.15	13.36±0.03	12.32±0.04	11.45±0.04	10.60±0.04	11/29/2004
CI Cam	04 19 42.1	+55 59 57	12.13±0.07	12.41±0.06	11.77±0.05	10.79±0.05	9.99±0.04	11/27/2004
			12.32±0.08	12.70±0.04	11.75±0.05	10.64±0.05	9.82±0.09	12/10/2005
			-	12.59±0.05	11.71±0.03	10.72±0.04	9.94±0.05	08/28/2006
DG Tau	04 27 04.7	+26 06 16	13.93±0.04	13.97±0.03	12.79±0.04	11.70±0.04	10.67±0.04	11/29/2004
DI Tau	04 29 42.5	+26 32 49	16.06±0.25	14.45±0.03	12.96±0.04	11.87±0.04	10.70±0.04	”
V830 Tau	04 33 10.0	+24 33 43	14.66±0.15	13.52±0.03	12.21±0.04	11.26±0.04	10.44±0.04	”
LkCa 15	04 39 17.8	+22 21 03	13.98±0.07	13.30±0.03	12.09±0.04	11.26±0.04	10.52±0.04	”
GM Aur	04 55 11.0	+30 21 59	13.90±0.04	13.38±0.03	12.19±0.04	11.34±0.04	10.61±0.04	”
AB Aur	04 55 45.8	+30 33 04	7.18±0.08	7.14 ±0.04	7.01 ± 0.04	6.96 ± 0.05	6.70±0.09	12/10/2005
			-	7.19±0.05	7.05± 0.05	7.01± 0.06	6.80±0.04	08/27/2006
MWC480	04 58 46.3	+29 50 37	-	7.91±0.05	7.68± 0.03	7.62± 0.05	7.45±0.05	08/28/2006

Target	RA (J2000) h m s	Dec ° ′ ″	U	B	V	R	I	UT Date
UX Ori	05 04 30.0	−03 47 14	10.93±0.07	10.70±0.06	10.33±0.05	10.07±0.05	9.75±0.04	11/29/2004
			10.43±0.08	10.22±0.04	9.97± 0.04	9.87± 0.05	9.56±0.09	12/10/2005
RW Aur	05 07 49.5	+30 24 05	10.86±0.04	11.07±0.03	10.32±0.04	9.78± 0.04	9.17±0.04	11/29/2004
GW Ori	05 29 08.4	+11 52 13	11.60±0.04	11.29±0.03	10.16±0.04	9.38± 0.04	8.75±0.04	11/29/2004
MWC 758	05 30 27.5	+25 19 57	8.59±0.07	8.56 ±0.06	8.28± 0.05	8.11± 0.05	7.95±0.04	11/29/2004
			-	8.58 ± 0.05	8.28± 0.03	8.15± 0.04	7.92±0.05	08/28/2006
V380 Ori*	05 36 25.4	−06 42 58	10.29±0.07	10.43±0.06	10.06±0.05	9.67± 0.05	8.99±0.04	11/29/2004
			10.07±0.08	10.15±0.04	9.74± 0.04	9.38 ± 0.05	8.80±0.09	08/27/2008
FU Ori	05 45 22.4	+09 04 12	-	10.80±0.08	9.52± 0.15	8.63± 0.05	8.11±0.15	11/29/2004
			11.57±0.08	10.81±0.04	9.47± 0.04	8.60± 0.05	7.89±0.09	12/10/2005
			-	10.87±0.05	9.65± 0.03	8.87± 0.05	8.13±0.05	08/28/2006
HD 45677	06 28 17.4	−13 03 11	7.03±0.07	7.56±0.06	7.51± 0.05	7.33± 0.05	7.24±0.04	11/27/2004
			6.99±0.08	-	7.52± 0.04	7.35± 0.05	7.06±0.09	12/10/2005
MWC 147	06 33 05.2	+10 19 20	8.45±0.07	8.87±0.06	8.65± 0.05	8.30± 0.05	8.02±0.04	11/27/2004
Z CMa	07 03 43.2	-11 33 06	9.78±0.07	9.86±0.06	9.17± 0.05	8.50± 0.05	7.75±0.04	”
MWC 166	07 04 25.5	-10 27 16	7.08±0.07	7.55±0.06	7.16± 0.05	6.97± 0.05	6.65±0.04	”
HD 58647	07 25 56.1	−14 10 44	6.66±0.07	6.874±0.06	6.73± 0.05	6.76± 0.05	6.67±0.04	”
IRC+10216	09 47 59.4	+13 16 44	-	-	>15.9	15.60±0.10	12.52±0.04	”

Target	RA (J2000) h m s	Dec ° ′ ″	U	B	V	R	I	UT Date
Beta Leo	11 49 03.6	+14 34 19	-	2.36±0.09	2.18±0.08	2.17±0.09	2.22±0.07	06/09/2006
HD141569	15 49 57.8	−03 55 16	-	7.32±0.09	7.16±0.08	7.14 ±0.09	7.15±0.07	”
			-	7.32±0.05	7.14±0.04	7.23± 0.06	7.03±0.04	08/27/2006
HD142666	15 56 40.0	−22 01 40	-	9.70±0.05	9.05±0.04	8.77±0.06	8.32±0.04	08/28/2006
HD143006	15 58 36.9	−22 57 15	-	10.94±0.09	10.12±0.08	9.63±0.09	9.38±0.07	06/09/2006
			-	10.95±0.05	10.14±0.04	9.75 ±0.06	9.22±0.04	08/28/2006
HD144432	16 06 58.0	−27 43 10	-	8.57 ±0.09	8.21 ±0.08	7.98±0.09	7.96±0.07	06/09/2006
			-	8.62 ±0.05	8.20 ±0.03	7.97±0.04	7.83±0.04	08/28/2006
HD150193 (MWC863)	16 40 17.9	−23 53 45	-	9.43 ±0.09	8.87±0.08	8.48±0.09	8.20±0.07	06/09/2006
			-	9.42 ±0.05	8.87±0.04	8.58±0.06	8.04±0.04	08/27/2006
KKOph	17 10 08.0	−27 15 18	-	12.77±0.09	12.11±0.08	11.61±0.09	11.16±0.07	06/09/2006
HD158352	17 28 49.7	+00 19 50	-	5.67 ±0.05	5.38 ±0.04	5.33±0.06	5.18±0.04	08/27/2006
HD158643	17 31 25.0	−23 57 45	-	4.81 ± 0.09	4.78 ±0.08	4.80±0.09	4.73±0.07	06/09/2006
				4.87 ±0.05	4.78 ±0.03	4.81 ±0.04	4.62±0.04	08/28/2006
RSOph	17 50 13.2	−06 42 28	-	12.65±0.08	11.43±0.06	10.21±0.05	9.51±0.07	06/08/2006
MWC275	17 56 21.3	−21 57 22	-	6.98 ±0.08	6.84 ±0.06	6.86 ±0.05	6.71±0.07	”

Target	RA (J2000) h m s	Dec ° ′ ″	U	B	V	R	I	UT Date
			-	7.01 ±0.05	6.86 ±0.04	6.90 ±0.06	6.72±0.04	08/27/2006
HD169412	18 21 33.5	+52 54 08	-	7.89 ±0.09	7.82 ±0.08	7.85±0.09	7.97±0.07	06/09/2006
MWC297	18 27 39.6	−03 49 52	-	14.38±0.09	12.26±0.08	10.29±0.09	9.10±0.07	”
			-	14.27±0.05	12.23±0.04	10.30±0.06	8.92±0.04	08/27/2006
VVSer	18 28 47.9	+00 08 40	-	13.23±0.08	12.22±0.06	11.36±0.05	10.61±0.07	06/08/2006
MWC 300	18 29 25.7	−06 04 37	-	12.87±0.09	11.82±0.08	11.01±0.09	10.56±0.07	06/09/2006
RCra	19 01 53.7	−36 57 08	-	12.17±0.05	11.45±0.03	10.82±0.05	10.15±0.05	08/28/2006
TCra	19 01 58.8	−36 57 50	-	13.67±0.05	12.50±0.03	11.87±0.05	11.23±0.05	”
MWC614	19 11 11.3	+15 47 16	-	7.50 ±0.05	7.37±0.04	7.41±0.06	7.26±0.04	08/27/2006
HIP96720	19 39 41.4	+14 02 53	-	11.06±0.05	10.65±0.03	10.38±0.05	10.06±0.05	08/28/2006
V1295 Aql	20 03 02.5	+05 44 17	-	7.85 ±0.08	7.79±0.06	7.69±0.05	7.59±0.07	06/08/2006
			-	7.93±0.05	7.80±0.04	7.77±0.06	7.58±0.04	08/27/2006
V1685Cyg	20 20 28.2	+41 21 52	-	11.63±0.09	10.79±0.08	10.06±0.09	9.58±0.07	06/09/2006
MWC342	20 23 03.6	+39 29 50	-	11.88±0.09	10.57±0.08	9.44±0.09	8.72±0.07	”
V1057 Cyg	20 58 53.7	+44 15 28	16.00±0.28	14.32±0.06	12.50±0.05	11.18±0.05	9.78±0.04	11/27/2004
MWC361	21 01 36.9	+68 09 48	-	7.75±0.05	7.33±0.03	7.00±0.04	6.62±0.05	08/28/2006
AS 477	21 52 33.9	+47 13 38	10.48±0.07	10.52±0.06	10.07±0.05	9.85±0.05	9.50±0.04	11/27/2004
HIP113937	23 04 23.6	−24 06 56	-	9.12±0.05	9.07±0.04	9.18±0.06	9.08±0.04	08/27/2006

Target	RA (J2000) h m s	Dec ° ′ ″	U	B	V	R	I	UT Date
HIP114547	23 12 09.4	−25 24 14	-	9.51±0.05	9.12 ±0.04	8.98± 0.06	8.67±0.04	”
HIP115858	23 28 25.2	−25 25 14	-	7.09±0.05	6.88 ±0.04	6.92± 0.06	6.72±0.04	”

Table B.3: JHK Photometry. Majority of the MDM targets are YSOs.

Target	RA (J2000) h m s	Dec ° ′ ″	J mag	H mag	K mag	UT Date
V892Tau	04 18 40.6	+28 19 16	8.61±0.05	7.08±0.05	5.86±0.05	12/17/2005
BP Tau	04 19 15.8	+29 06 27	9.10±0.10	8.37±0.10	7.90±0.10	12/01/2004
			9.05±0.05	8.32±0.05	7.85±0.05	12/17/2005
CI Cam	04 19 42.1	+55 59 58	7.20±0.10	5.68±0.10	4.44±0.10	12/01/2004
			7.01±0.05	5.63±0.05	4.35±0.05	12/17/2005
DG Tau	04 27 04.7	+26 06 16	8.92±0.05	7.95±0.05	7.15±0.05	12/17/2005
V830 Tau	04 33 10.0	+24 33 43	9.36±0.05	8.73±0.05	8.52±0.05	12/17/2005
LkCa 15	04 39 17.8	+22 21 04	9.33±0.05	8.72±0.05	8.23±0.05	12/17/2005
GM Aur	04 55 11.0	+30 22 00	9.40±0.05	8.80±0.05	8.52±0.05	12/17/2005
AB Aur	04 55 45.8	+30 33 04	5.99±0.05	5.28±0.05	4.37±0.05	12/17/2005
MWC480	04 58 46.3	+29 50 37.0	6.90±0.05	6.38±0.05	5.57±0.05	12/17/2005
RW Aur	05 07 49.5	+30 24 05	8.22±0.05	7.67±0.05	7.16±0.05	12/01/2004
			8.34±0.10	7.66±0.10	7.18±0.10	12/17/2005
GW Ori	05 29 08.4	+11 52 13	7.42±0.05	6.67±0.05	5.83±0.05	12/17/2005
MWC 758	05 30 27.5	+25 19 57	7.20±0.10	6.55±0.10	5.80±0.10	12/01/2004
			7.26± 0.05	6.70±0.05	5.92±0.05	12/17/2005

Target	RA (J2000) h m s	Dec ° ′ ″	J	H	K	UT Date
MWC120	05 41 02.3	−02 43 00	7.24±0.05	6.66±0.05	5.77±0.05	12/17/2005
FU Ori	05 45 22.4	+09 04 12	6.55±0.05	5.89±0.05	5.32±0.05	12/17/2005
HD 45677	06 28 17.4	−13 03 11	6.85±0.05	6.22±0.05	4.61±0.05	12/17/2005
MWC 147	06 33 05.2	+10 19 20	7.34±0.05	6.70±0.05	5.73±0.05	12/17/2005
Z CMa	07 03 43.2	−11 33 06	6.66±0.05	5.45±0.05	3.94±0.05	12/17/2005
MWC 166	07 04 25.5	−10 27 16	6.32±0.05	6.32±0.05	6.27±0.05	12/17/2005
Beta Leo	11 49 03.6	+14 34 19	1.92±0.08	1.96±0.07	1.90±0.08	06/02/2006
LambdaVir	14 19 06.6	−13 22 16	4.26±0.08	4.25±0.07	4.20±0.08	”
HD141569	15 49 57.8	−03 55 16	6.67±0.08	6.54±0.07	6.48±0.08	06/02/2006
HD143006	15 58 36.9	−22 57 15	8.18±0.08	7.57±0.07	5.94±0.08	06/02/2006
HD144432	16 06 58.0	−27 43 10	7.23±0.08	6.69±0.07	6.14±0.08	06/02/2006
HD150193 (MWC863)	16 40 17.9	−23 53 45	6.84±0.08	6.02±0.07	5.13±0.08	06/02/2006
KKOph	17 10 08.1	−27 15 18	8.46±0.08	7.09±0.07	5.71±0.08	06/02/2006
HD158643	17 31 25.0	−23 57 46	4.76±0.08	4.63±0.07	4.34±0.08	06/02/2006
RSOph	17 50 13.2	−06 42 29	7.94±0.08	7.17±0.07	6.77±0.08	06/04/2006
MWC275	17 56 21.3	−21 57 22	6.20±0.08	5.48±0.07	4.59±0.08	06/02/2006
HD169412	18 21 33.5	+52 54 08	7.77±0.08	7.78±0.07	7.79±0.08	06/02/2006
MWC297	18 27 39.6	−03 49 52	6.06±0.08	4.54±0.07	3.12±0.08	06/04/2006

Target	RA (J2000) h m s	Dec ° ′ ″	J	H	K	UT Date
VVSer	18 28 47.9	+00 08 40	8.60±0.08	7.37±0.07	6.20±0.08	06/02/2006
MWC614	19 11 11.3	+15 47 16	6.91±0.08	6.58± 0.07	5.88±0.08	06/03/2006
V1295Aql	20 03 02.5	+05 44 17	7.15±0.08	6.61±0.07	5.75±0.08	06/02/2006
V1685Cyg	20 20 28.3	+41 21 52	7.97±0.05	7.01±0.05	5.86±0.05	12/17/2005
			7.93±0.10	6.96±0.04	5.81±0.07	06/03/2006
MWC342	20 23 03.6	+39 29 50	7.01±0.05	5.98±0.05	4.78±0.05	12/17/2005
			6.94±0.08	5.92±0.08	4.65±0.08	06/03/2006
MWC361	21 01 36.9	+68 09 48	6.12±0.05	5.58±0.05	4.77±0.05	12/17/2005
MWC1080	23 17 25.6	+60 50 43	7.38±0.05	6.04±0.05	4.68±0.05	12/17/2005

Appendix C

"Effective Baselines" as a tool in characterizing visibility information.

Let $B_{projected}$ be the projected interferometric baseline and let V($B_{projected}$) be the visibility for a circularly symmetric brightness distribution. For a flat disk inclined at angle ϕ and oriented at some PA, we plotted V(B_{eff}) in Fig §3.6. The effective baseline B_{eff} is defined as -

$$B_{eff} = B_{projected}\sqrt{cos^2(\theta) + cos^2(\phi)sin^2(\theta)}$$

where θ is the angle between the uv vector for the observation and the major axis of the inclined disk and ϕ is the inclination of the disk (0^o inclination is face on). Effective baselines account for the decrease in interferometric resolution due to the inclination of the disk in the sky. They capture the geometry of flat disks correctly, but the geometry of finitely thick disks is represented only approximately (optical depth effects and 3-D geometry of thick disks are not taken into account). Here, we argue that effective baselines are good (albeit approximate) tools for capturing details of the MWC275 disk geometry.

In order to determine the inclination angle and sky orientation of the disk, we adopted the following procedure. MC275 visibility values measured with W1W2, S2W2 and E2S2 CHARA-telescope-pairs are close to and just prior to the first mini-

mum in the visibility curve (see Fig 3.6). In this region the visibility-baseline relation for the emission models in Fig 5.42 can be approximated with a linear function. We calculated reduced χ^2 values for the best-fit line to the W1W2, S2W2 and E2S2 visibilities as a function of effective baseline, varying the assumed inclination and position angle of the observed disk. Fig C.1 shows the reduced χ^2 surface for the fits, plotted against the assumed disk-inclination and position angle. To further illustrate the change in quality of fits as inclination and position angles are varied , Fig C.2 shows the linear fits to the visibility vs effective baseline data set.

As seen in Figs C.1 and C.2, the quality of the fits show dramatic improvement at MWC275 disk PA of $136^o \pm 2^o$ and inclination of $48^o \pm 2^o$. These values are very close to a disk PA of $139^o \pm 15^o$ and inclination of 51^{+11}_{-9} degrees determined in Wassell et al. [2006]. The excellent agreement in inclination and PA values for MWC275 from two independent methods strongly supports a disk model for MWC275, validating the use of "effective baselines" to plot MWC275 visibilities.

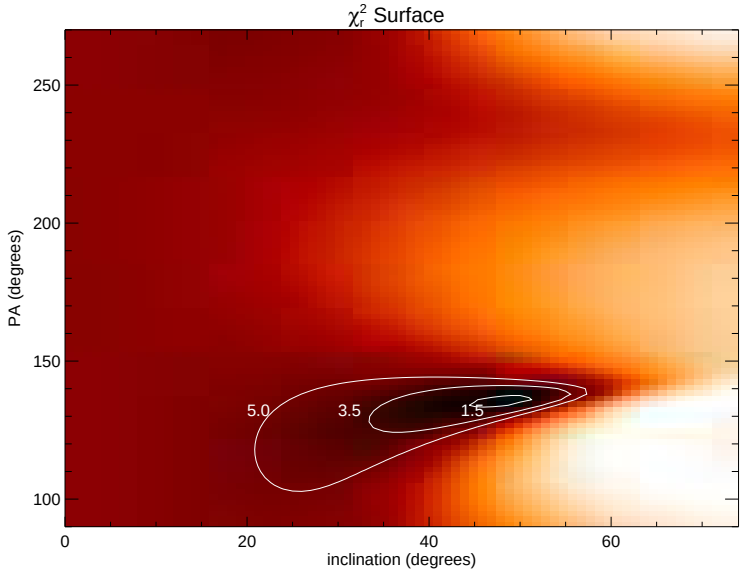

Figure C.1 Reduced χ^2 surface for linear fits to visibilities of MWC275. The visibilities were obtained with the W1W2, S2W2 and E2S2 CHARA-telescope-pairs and fits were made as a function of effective interferometric baseline. The solid curves are reduced χ^2 contours of 5, 3.5 and 1.5 respectively.

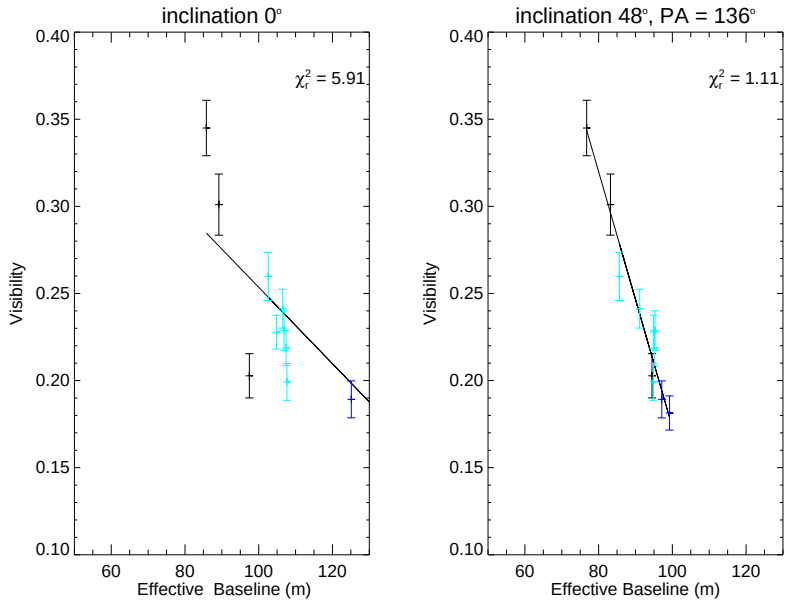

Figure C.2 Linear fits to the observed visibilities vs effective baseline. The data were obtained with the W1W2, S2W2 and E2S2 CHARA-telescope-pairs. The data symbols are explained in Fig. 3.6.

References

Acke, B. & van den Ancker, M. E. 2004a, *A&A*, 426, 151

Acke, B. & van den Ancker, M. E. 2004b, *A&A*, 422, 621

Adams, F. C., Lada & Shu, F. H. 1987, *ApJ*, 312, 788

Akeson, R. L., Ciardi, D. R., van Belle, G. T., Creech-Eakman, M. J. & Lada, E. A. 2000, *ApJ*, 543, 313

Akeson, R. L., Walker, C. H., Wood, K., Eisner, J. A., Scire, E., Penprase, B., Ciardi, D. R., van Belle, G. T., Whitney, B. & Bjorkman, J. E. 2005a, *ApJ*, 622, 440

Akeson, R. L., Boden, A. F., Monnier, J. D., Millan-Gabet, R., Beichman, C., Beletic, J., Calvet, N., Hartmann, L., Hillenbrand, L., Koresko, C., Sargent, A. & Tannirkulam, A. 2005b *ApJ*, 635, 117

Alencar, S. H. P, Basri, G., Hartmann, L. & Calvet, N. 2005, *ApJ*, 440, 595

Andre, P., Ward-Thompson, D. & Barsony, M. 2000, Protostars and Planets IV, 59

Artymowicz, P. & Lubow, S. H. 1994, *ApJ*, 421, 651

Barth, A. J. 2001, ASP Conf. Ser., 238, 385

Berger, D. H., Monnier, J. D., Millan-Gabet, R., ten Brummelaar, T. A., Muirhead, P., Pedretti, E. & Thureau, N. 2006, SPIE, 6268, 62683K

Berger, D. H., Monnier, J. D., Millan-Gabet, R. & 6 coauthors 2008, SPIE, 701319

Bernstein, R., Schectman, S. A., Gunnels, S. M., Mochnacki, S., & Athey, A. E. 2003, SPIE, 4841, 1694B

Blandford, R. D & Payne, D. G. 1982, *MNRAS*, 199, 883

Brittain, S. D., Rettig, T. W., Simon, T. & Kulesa, C. 2005, *ApJ*, 626, 283

Burrows, C. J., Stapelfeldt, K. R., Watson, A. M., Krist, J. E., Ballester, G. E & 12 coauthors , *ApJ*, 473, 437

Buscher, D. F. 1994, in IAU Symposium, Vol. 158, Very High Angular Resolution Imaging, ed. J. G. Robertson & W. J. Tango, 91–+

Calvet, N., Patino, A., Magris, C. G. & D'Alessio, P. 1991, *ApJ*, 380, 617

Calvet, N. & Gullbring, E. 1998, *ApJ*, 509, 802

Calvet, N., D'Alessio, P., Hartmann, L., Wilner, D., Walsh, A., & Sitko, M. 2002, *ApJ*, 568, 1008

Carpenter, J. M., Hillenbrand, L. A., Skrutskie, M. F. & Meyer, M. R. 2002, *ApJ*, 124, 1001

Carr, J. S., Tokunaga, A. T. & Najita, J. 2004, *ApJ*, 603, 213

Chiang, E., I. & Goldreich, P. 1997, *ApJ*, 490, 368

Chiang, E. I., Joung, M. K., Creech-Eakman, M. J., Qi, C., Kessler, J. E., Blake, G. A. & van Dishoeck, E. F. 2001, *ApJ*, 547, 1077

Corder, S., Eisner, J. & Sargent, A. 2005, *ApJ*, 622, L133

D'Alessio, P., Calvet, N. & Hartmann, L. 2001, *ApJ*, 553, 321

D'Alessio, P., Calvet, N., Hartmann, L., Franco-Hernandez, R. & Servin, H. 2006, *ApJ*, 638, 314

Dominik, C., Dullemond, C. P., Waters, L. B. F. M. & Walch, S. 2003, *A&A*, 398, 607

Dubrulle, B., Morfill, G., & Sterzik, M. 1995, *Icarus*, 114, 237

Dullemond, C. P., Dominik, C. & Natta, A. 2001, *ApJ*, 560, 957

Dullemond, C. P. & Natta, A. 2003, *A&A*, 408, 161

Dullemond, C. P., van den Ancker, M. E, Acke, B. & van Boekel, R. 2003b, *ApJ*, 594, L47

Dullemond, C. P. & Dominik, C. 2004, *A&A*, 421, 1075

Eisner, J. A., Lane, B. F., Akeson, R. L., Hillenbrand, L. A. & Sargent, A. I. 2003, *ApJ*, 588, 360

Eisner, J. A., Lane, B. F., Hillenbrand, L. A., Akeson, R. L. & Sargent, A. I. 2004, *ApJ*, 613, 1049

Eisner, J. A., Chiang, E. I., Lane, B. F. & Akeson, R. L. 2007, *ApJ*, 657, 347

Eisner, J. A. 2007, *Nature*, 447, 562

Elias, J. H., Frogel, J. A., Matthews, K. & Neugebauer, G. 1982, *A&A*, 87, 1029

Espaillat, C., et al. 2007, *ApJ*, 670, L135

Ferguson, J. W., Alexander, D. R., Allard, F., Barman, T., Bodnarik, J. G., Hauschildt, P. H., Heffener-Wong, A. & Tamanai, A. 2005, *ApJ*, 623, 585

Fromang, S. & Papaloizou, J. 2006, *A&A*, 452, 751

Fukagawa, M., Hayashi, M., Tamura, M., Itoh, Y., Hayashi, S. S., Oasa, Y. & 17 co-authors 2004, *ApJ*, 605, L53

Furlan, E. "Properties and evolution of circumstellar disks and envelopes around young, low-mass stars in the Taurus star-forming region", 2006, Ph.D. dissertation, A&I database, Publication No. AAT 3205198

Gail H. P. 2004, *A&A*, 413, 571

Garcia Lopez, R., Natta, A., Testi, L. & Habart, E. 2006, *A&A*, 459, 847

Gibb, E. L., Van Brunt, K. A., Brittain, S. D. & Rettig, T. W. 2007, *ApJ*, 660, 1572

Grady, C. A., Woodgate, B., Bruhweiler, F. C., Boggess, A., Plait, P., Lindler, D. J., Clampin, M. & Kalas, P. 1999, *ApJ*, 523, L151

Grady, C. A., Devine, D., Woodgate, B., Kimble, R., Bruhweiler, F. C., Boggess, A., Linsky, J. L , Plait, P., Clampin, M. & Kalas, P. 2000, *ApJ*, 544, 895

Haas, M., Leinert, C., & Richichi, A. 1997, *A&A*, 326, 1076

Hanner, M. 1988, Grain optical properties, Technical report

Herbst, W. & Shevchenko, V. S. 1999, *AJ*, 118, 1043

Harries, T. J. 2000, *MNRAS*, 315, 722

Harries, T. J., Monnier, J. D., Symington, N. H. & Kurosawa, R. 2004, *MNRAS*, 350, 565

Hartmann, L., Kenyon, S. J. & Calvet, N. 1993, *ApJ*, 407, 219

Hartmann, L., Hewett, R. & Calvet, N. 1994, *ApJ*, 426, 669

Herbig, G. H., 1960, ApJS , 4, 337

Hernández, J., Calvet, N., Briceño, C., Hartmann, L., & Berlind, P. 2004, *AJ*, 127, 1682

Hillenbrand, L. A., Strom, S. E., Vrba, F. J. & Keene, J. 1992, *ApJ*, 397, 613

Isella, A. & Natta, A. 2005, *A&A*, 438, 899

Isella, A., Testi, L. & Natta, A. 2006, *A&A*, 451, 951

Isella, A., Natta, A. & Testi, L. 2007, *A&A*, 469, 213

Jones, B. & Puetter, R. C. 1993, SPIE, 1946, 610

Johansen, A.& Klahr, H. 2005, *ApJ*, 634, 1353

Kamp, I. & Dullemond, C. P. 2004, *ApJ*, 615, 991

Kataza, H. & Maihara, T. 1991, *A&A*, 248, L1

Kenyon, S. & Hartmann, L. 1987, *ApJ*, 323, 714

Kenyon, S. J., Dobrzycka, D., & Hartmann, L. 1994, *AJ*, 108, 1872

Kenyon, S. J. & Hartmann, L. 1995, *ApJS*, 101, 117

Kraus, A., Hoffmann, K. H., Benisty, M., Berger, J. P. & 13 co-authors 2008b, *A&A*, in press

Kraus, A., Preibisch, T. & Ohnaka, K. 2008a, *ApJ*, 676, 490

Krist, J. E., Ardila, D. R., Golimowski, D. A., Clampin, M., Ford, H. C & 36 coauthors , *ApJ*, 129, 1008

Kurosawa, R., Harries, T. J., Bate, M. R. & Symington, N. H. 2004, *MNRAS*, 351, 1134

Kurosawa, R., Harries, T. J. & Symington, N. H. 2006, *MNRAS*, 370, 580

Kurosawa, R., Romanova, M. M. & Harries, T. J. 2008, *MNRAS*, 385, 1931

Kurucz, R. L. 1970, SAO Special Report 308 (Cambridge: SAO)

Lada, C. J., 1987, IAU Symp ,115, 1

Landolt, A. U. 1983, *ApJ*, 88, 439

Landolt, A. U. 1992,*A&A*, 104, 340

Lamers, H. J. G. L. M. & Waters, L. B. F. M. 1984, *A&A*, 136, 37

Lawson, P. R., et al. 2004, Proceedings of SPIE, Vol. 5491. p.886

Lawson, P. R., et al. 2006, Proceedings of SPIE, Vol. 6268, pp. 62681U

Leinert, C., Haas, M., Ábrahám, P., & Richichi, A. 2001, *A&A*, 375, 927

Leinert, Ch., van Boekel, R., Waters, L. B. F. M., Chesneau, O.,Malbet, F. & Kohler, R. 2004, *A&A*, 423, 537

Lissauer, J. J & Stevenson, D. J. 2007, Protostars and Planets V, 591

Lin, D. N. C., Bodenheimer, P. & Richardson, D. C. 1996, Nature, 380, 606

Lin, S., Ohashi, N., Lim, J., Ho, P., Fukagawa, M. & Tamura ,M. 2006, *ApJ*, 645, 1297

Liu, W. M., et al. 2005, *ApJ*, 618, L133

Liu, W. M., Hinz, P. M., Meyer, M. R., Mamajek, E. E., Hoffmann, W. F., Brusa, G., Miller, D.& Kenworthy, M. A. 2007, *ApJ*, 658, 1164

Lucy, L. B. 1999, *A&A*, 344, 282

Mannings, V. & Sargent, A. I. 1997 *ApJ*, 490, 792

Mariñas, N., Telesco, C. M., Fisher, R. S., Packham, C.& Radomski, J. T. 2006, 653, 1353.

Matthews, K., Ghez, A. M., Weinberger, A. J., & Neugebauer, G. 1996, *PASP*, 108, 615

McCarthy, D. W. & Low, F. J. 1975 *ApJ*, 202, 37

Meeus2001, G., Waters, L. B. F. M., Bouwman, J., van den Ancker, M. E., Waelkens, C. & Malfait, K. 2001, *A&A*, 365, 476

Merand, A., Borde, P. & Coude Du Foresto, V. 2004, *A&A*, 433, 1155

Michelson, A. A. & Pease, F. G. 1921, *ApJ*, 53, 249

Millan-Gabet, R., Schloerb, F. P., Traub, W. A., Malbet, F., Berger, J. P. & Breg-

man, J. D. 1999, *ApJ*, 513, L131

Millan-Gabet, R., Schloerb, F. P. & Traub, W. A. 2001, *ApJ*, 546, 358

Millan-Gabet, R., Monnier, J. D. & Berger, J. P., Traub, W. A. & 12 coauthors 2006, *ApJ*, 645, L77

Millan-Gabet, R., Malbet, F., Akeson, R., Leinert, C., Monnier, J. D. & Waters, R. 2007, Protostars and Planets V, 539

Miroshnichenko, A., Ivezic, Z. & Elitzur, E. 1997, *ApJ*, 475, 41

Monnier, J. D., Principles of LongBaseline Stellar Interferometry, Course notes from the 1999 Michelson Summer School, Edited by P. R. Lawson (JPL Publication) 2000, 9, 203

Monnier, J. D. & Millan-Gabet, R. 2002, *ApJ*, 579, 694

Monnier, J. D., Tuthill, P. G., Ireland, M. J., Cohen, R. & Tannirkulam, A. 2004, AAS 205, 36, 1367

Monnier, J. D., Millan-Gabet, R., Billmeier, R., Akeson, R. L., Wallace, D., Berger, J. P., Calvet, N., D'Alessio, P., Danchi, W. C., Hartmann, L. & 24 coauthors, 2005, *ApJ*, 624, 832

Monnier, J. D., Berger, J. P., Millan-Gabet, R., Traub, W. A., Schloerb, F. P., Pedretti, E., Benisty, M., Carleton, N. P., Haguenauer, P., Kern, P., Labeye, P., Lacasse, M. G., Malbet, F., Perraut, K., Pearlman, M. & Zhao, M. 2006, *ApJ*, 647, 444

Monnier, J. D., Zhao, M., Pedretti, E., Thureau, N., Ireland, M., Muirhead, P., Berger, J. P., Millan-Gabet, R., Van Belle, G., ten Brummelaar, T., McAlister, H., Ridgway, S., Turner, N., Sturmann, L., Sturmann, J. & Berger, D. 2007, *Science*, 317, 342

Monnier, J. D., Tannirkulam, A., Tuthill, P. G., Ireland, M., Cohen, R., Danchi, W. C. & Baron, F. 2008, *ApJ*, 681, L97

Monnier, J. D. et al. 2008, in preparation.

Mottram, J. C., Vink, J. S., Oudmaijer, R. D. & Patel, M. 2007, *MNRAS*, 377, 1363

Muzerolle, J., Calvet, N. & Hartmann, L. 1998, *ApJ*, 492, 743

Muzerolle, J., Calvet, N. & Hartmann, L. 2001, *ApJ*, 550, 944

Muzerolle, J., D'Alessio, P., Calvet, N., & Hartmann, L. 2004, *ApJ*, 617, 406

Nagasawa, M., Thommes, E. W., Kenyon, S. J., Bromley, B. C. & Lin, D. N. C. 2007, Protostars and Planets V, 639

Najita, J., Carr, J. & mathieu, R. D. 2003, *ApJ*, 589, 931

Najita, J., Carr, J., Glassgold, A. E. & Valenti, J. A. 2007, Protostars and Planets V, 507

Natta, A., Prusti, T., Neri, R., Wooden, D., Grinin, V. P. & Mannings, V. 2001, *A&A*, 371, 186

Natta, A., Testi, L., Neri, R., Sheperd, D. S. Wilner, D. J. 2004, *A&A*, 416, 179

Oppenheimer, B. R., Brenner, D., Hinkley, S., Zimmerman, N., Sivaramakrishnan, A. & 7 coauthors 2008, *ApJ*, 680

Ossenkopf, V., Henning, Th., Mathis, J. S. 1992, *A&A*, 261, 567

Pascucci, I., Wolf, S., Steinacker, J., Dullemond, C. P., Henning, Th., Niccolini, G., Woitke, P. & Lopez, B., *A&A*, 2004, 417, 793.

Pinte, C., Menard, F., Berger, J. P., Benisty, M. & Malbet, F. 2008 *A&A*, in press

Pollack, J. B., Hollenbach, D., Beckwith, S., Simonelli, P. D., Roush, T. & Fong, W. 1994, *ApJ*, 421, 615

Pollack, J. B., Hubickyj, O., Bodenheimer, P., Lissauer, J. J., Podolak, M. & Greenzweig, Y. 1996, Icarus, 124, 1, 62

Pontoppidan, K. M., Dullemond, C. P., Blake, G. A., Adwin Boogert, A. C., van Dishoeck, E. F., Evans, N. J., Kessler-Silacci, J. & Lahuis, F. 2007, *ApJ*, 656, 980.

Rettig, T., Brittain, S., Simon, T., Gibb, E., Balsara, D. S., Tilley, D. A. & Kulesa, C. 2006, *ApJ*, 646, 342

Robitaille, T. P., et al. 2006, *ApJS*, 167, 256

Romanova, M. M., Kulkarni, A. K. & Lovelace, R. V. E. 2008, *ApJ*, 673, L171

Semenov, D., Pavlyuchenkov, Ya., Schreyer, K., Henning, Th., Dullemond, C. & Bacmann, A. 2005, *ApJ*, 621, 853

Shakura, N. I. & Sunyaev, R. A. 1973, *A&A*, 24, 337

Strom, K. M. & Strom, S. E. 1994, *ApJ*, 424, 237

Shu, F. H., Adams, F. C. & Lizano, S. 1987, Annual Review of Astronomy and Astrophysics, 25, 23

Sitko, S. L., Carpenter, W. J., Kimes, R. L., Wilde, J. L., & 11 coauthors, J. P. 2008, *ApJ*, 678, 1070

Smith, K. W., et al. 2005, *A&A*, 431, 307

Tanaka, H., Himeno Y., & Ida, S. 2005, *ApJ*, 625, 414

Tannirkulam, A., Harries, T. J., & Monnier, J. D. 2007, *ApJ*, 661, 374

Tannirkulam, A., Monnier, J. D., Millan-Gabet, R., Harries, T. J., Pedretti, E. & 4 coauthors 2008, *ApJ*, 677, L51

Tannirkulam, A., Monnier, J. D., Harries, T. J.,Millan-Gabet, R., Zhao, Z., Pedretti, E. & 6 coauthors 2008, *ApJ*, accepted

Tatulli, E., Isella, A., Testi, L., Marconi, A. & 94 coauthors 2007, *A&A*, 464, 29

ten Brummelaar, T. A., McAlister, H. A., Ridgway, Bagnuolo, W. G. Jr., Turner, N. H. & 8 coauthors 2005, *ApJ*, 628, 453

Turner, N. J, Willacy, K., Bryden, G. & Yorke. H. W. 2006, *ApJ*, 639, 1218

Tuthill, P. G., et al. 2000, *PASP*, 112, 555

Tuthill, P. G., Monnier, J. D. & Danchi, W. C. 2001, *Nature*, 409, 1012

van Boekel, R., Min, M., Leinert, Ch., Waters, L. B. F. M., Richichi, A., Chesneau, O., Dominik, C., Jaffe, W., Dutrey, A., Graser, U., Henning, Th., de Jong, J., Köhler, R., de Koter, A., Lopez, B., Malbet, F., Morel, S., Paresce, F., Perrin, G., Preibisch, Th., Pryzgodda, F., Schöller, M. & Wittkowski, M. 2004, *Nature*, 432, 479

van Boekel, R., Min, M., Waters, L. B. F. M., de Koter, A., Dominik, C., van den Ancker, M. E. & Bouwman, J. 2005, *A&A*, 437, 189

van Boekel, R., Dullemond, C. P. & Dominik, C. 2005, *A&A*, 441, 563

Vinkovic, D., Ivezic, Z., Jurkic, T. & Elitzur, M. 2006, *ApJ*, 636, 348

Vinkovic, D. 2006b, *ApJ*, 651, 906

Wassell, E. J., Grady, C. A., Woodgate, B., Kimble, R. A. & Bruhweiler, F. C. 2006, *ApJ*, 650, 985

Walker, C., Wood, K., Lada, C. J., Robitaille, T., Bjorkman, J. E. & Whitney, B. 2004, *MNRAS*, 351, 607

Waters, L. B. F. M, & Waelkens, C. 1998, Annual Review of Astronomy and Astrophysics, 36, 233

Weidenschilling, S. J. & Cuzzi, J. N. 1993, Protostars and Planets III, 1031

Weiner, J., Tatebe, K.,Hale, D. D. S., Townes, C. H., Monnier, J. D., Ireland, M., Tuthill, P. G., Cohen, R., Barry, R. K., Rajagopal, J. & Danchi, W. C. 2006 *ApJ*, 636, 1067

Weingartner, J. C. & Draine, B. T. 2001, *ApJ*, 548, 296

Wetherill, G. W. 1990, Icarus, 88, 336

Wilking, B. A., 1989, PASP ,101, 229

Wood, K., Mathis, J., S. & Ercolano, B. 2004, *MNRAS*, 348, 1337

Zhu, Z., Hartmann, L., Calvet, N., Hernandez, J., Muzerolle, J., & Tannirkulam, A. 2007, *ApJ*, 669, 483